On-Line Monitoring and Diagnostics of the Integrity of Nuclear Plant Steam Generators and Heat Exchangers

Final Report

Report No. DE-FG07-01ID14114/UTNE-07
NEER Grant Number: DE-FG07-01ID14114

Volume 1

Experimental and Hybrid Modeling Approach for Monitoring Heat Exchanger System Performance

Belle R. Upadhyaya
J. Wesley Hines
(Principal Investigators)

Baofu Lu
Xuedong Huang
Rosani L. Penha
Sergio R. Perillo
Ke Zhao

The University of Tennessee
Nuclear Engineering Department
209 Pasqua Engineering Building
Knoxville, TN 37996-2300
E-mail: bupadhya@utk.edu

DOE Program Manager for NEER
Idaho Operations Office
Nancy A. Elizondo

September 2004

EXECUTIVE SUMMARY

The overall purpose of this Nuclear Engineering Education Research (NEER) project was to integrate new, innovative, and existing technologies to develop a fault diagnostics and characterization system for nuclear plant steam generators (SG) and heat exchangers (HX). Issues related to system level degradation of SG and HX tubing, including tube fouling, performance under reduced heat transfer area, and the damage caused by stress corrosion cracking, are the important factors that influence overall plant operation, maintenance, and economic viability of nuclear power systems. The research at The University of Tennessee focused on the development of techniques for monitoring process and structural integrity of steam generators and heat exchangers.

The objectives of the project were accomplished by the completion of the following tasks. All the objectives were accomplished during the project period. This report summarizes the research and development activities, results, and accomplishments during June 2001 – September 2004.

- Development and testing of a high-fidelity nodal model of a U-tube steam generator (UTSG) to simulate the effects of fouling and to generate a database representing normal and degraded process conditions. Application of the group method of data handling (GMDH) method for process variable prediction.
- Development of a laboratory test module to simulate particulate fouling of HX tubes and its effect on overall thermal resistance. Application of the GMDH technique to predict HX fluid temperatures, and to compare with the calculated thermal resistance.
- Development of a hybrid modeling technique for process diagnosis and its evaluation using laboratory heat exchanger test data.
- Development and testing of a sensor suite using piezo-electric devices for monitoring structural integrity of both flat plates (beams) and tubing. Experiments were performed in air, and in water with and without bubbly flow.

- Development of advanced signal processing methods using wavelet transforms and image processing techniques for isolating flaw types.
- Development and implementation of a new nonlinear and non-stationary signal processing method, called the Hilbert-Huang transform (HHT), for flaw detection and location. This is a more robust and adaptive approach compared to the wavelet transform.
- Implementation of a moving-window technique in the time domain for detecting and quantifying flaw types in tubular structures. A window zooming technique was also developed for flaw location in tubes.
- Theoretical study of elastic wave propagation (longitudinal and shear waves) in metallic flat plates and tubing with and without flaws.
- Simulation of the Lamb wave propagation using the finite-element code ABAQUS. This enabled the verification of the experimental results.

The research tasks included both analytical research and experimental studies. The experimental results helped to enhance the robustness of fault monitoring methods and to provide a systematic verification of the analytical results. The results of this research were disseminated in scientific meetings. A journal manuscript was submitted for publication. The new findings of this research have potential applications in aerospace and civil structures. The report contains a complete bibliography that was developed during the course of the project.

ACKNOWLEDGMENTS

The research was supported by a U.S. Department of Energy Nuclear Engineering Education Research (NEER) grant with the University of Tennessee, Knoxville (grant number DE-FG07-01ID14114). We want to acknowledge the assistance provided by the NEER grant office, DOE Idaho Operations. The authors wish to thank Professor Emeritus Rafael Perez, University of Tennessee, for the discussion of Hilbert-Huang transformation and its implementation. The authors greatly appreciate the assistance provided by Richard Bailey and Gary Graves of the Nuclear Engineering Department in developing the experimental facilities for this project.

DISCLAIMER

Any opinions, findings, and conclusions or recommendations expressed in this report are those of the authors and do not necessarily reflect the views of the Department of Energy.

CONTENTS

1. INTRODUCTION, BACKGROUND, AND OBJECTIVES

1.1. Background and Objectives

The objective of the research project at The University of Tennessee was to develop a system for *On-line Monitoring and Diagnostics of Integrity of Nuclear Plant Steam Generators and Heat Exchangers.* Both structural and process integrity of these components were considered. Steam generators (SG) and heat exchangers (HX) constitute a significant part of power generation systems, and their reliability and availability influence plant operation, maintenance, and cost control issues. Such issues are especially important for the next generation reactors, which require remote monitoring for both system integrity and for increasing the maintenance interval necessitated by increased fuel cycle lengths. Furthermore, the incorporation of an on-line monitoring system must be considered during the design phase, thus increasing its effectiveness and avoiding unnecessary retrofitting. The three-year project achieved the integration of new, innovative, and existing technologies to develop an automated structural fault diagnostics and characterization system for nuclear plant heat exchangers and steam generators.

A nuclear plant steam generator is one of the critical components of a nuclear power plant. There are thousands of tubes in a steam generator. The U-tube steam generator (UTSG) in a typical four-loop, 1,300 MWe pressurized water reactor (PWR), consists of about 3,600 tubes. Tube degradation can occur due to thermal and mechanical stresses, fouling and deposits, fatigue and creep, wear and fretting, and stress corrosion cracking and intergranular attack. Depending on the nature of plant operating conditions, one or more of the above causes may result in tube damage. The degradation of tubes in a steam generator is the primary cause of its reduced performance and of its structural failure. A remedy often used by the industry is to plug damaged and leaking tubes. This, in turn, results in decreased operational efficiency with time. The cost of replacement of a large UTSG in a 1,300 MWe four-loop PWR is about $150 million. Several operating PWR units in the U.S. have either replaced steam generators or are seriously considering this upgrading. These provide a strong argument for the development of continuous on-line monitoring of their structural integrity and incipient fault detection and isolation.

The use of a distributed and embedded sensor suite and extracting information from sensor arrays would result in a *smart structure* with self-inspection capability. Since the project emphasized he application of this technology to next generation reactors, the creation of hybrid database for use in predictive models, was given high priority. Figure 1.1 is a schematic of the integration of plant monitoring, diagnosis, and prognosis modules. It is anticipated that this system will provide timely decision-making information about the status of plant devices and components to operational personnel.

The capability and experience of The University of Tennessee in system monitoring and diagnosis and new methods being developed under this project are being directed towards implementation in the next generation nuclear power plants. Features such as the use of this technology in plant design-phase, wireless communication, Internet-based e-maintenance, and other remote technologies must also being considered in technology implementation.

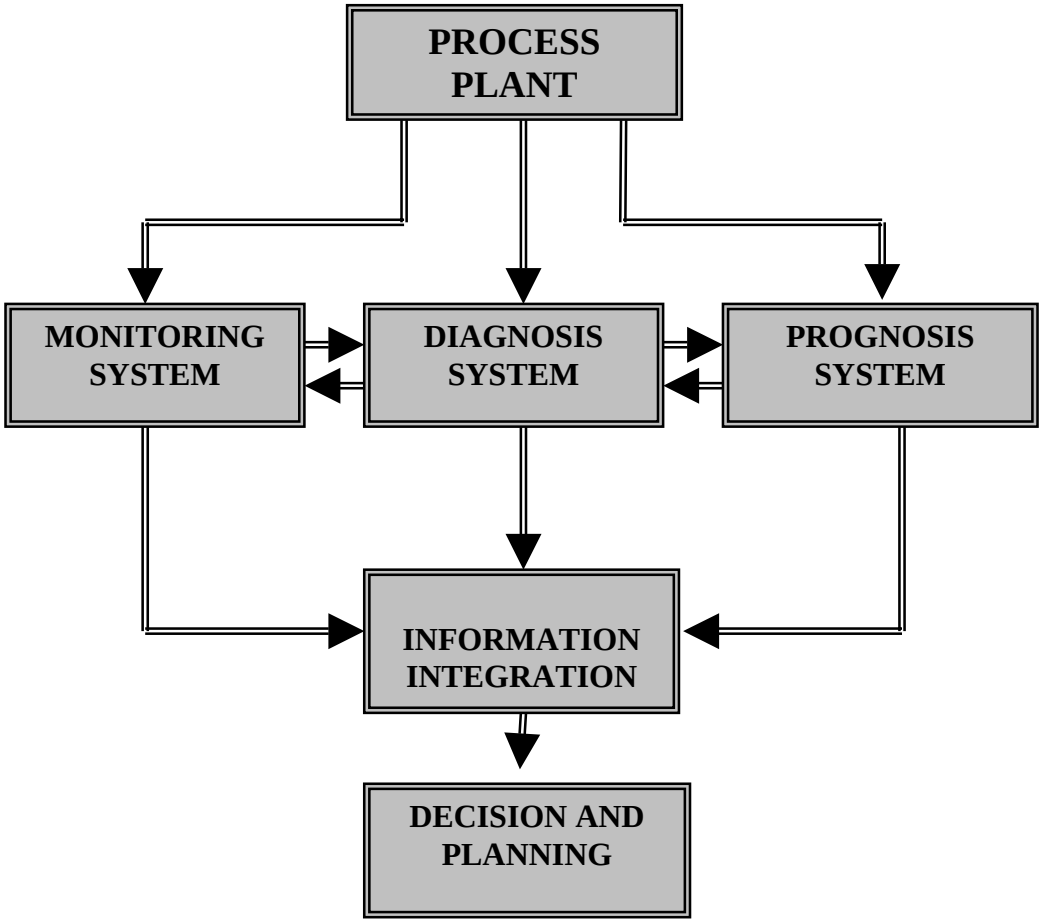

Figure 1.1. Schematic of a plant monitoring, diagnosis, and prognosis system.

1.2. Summary of Research Tasks and Significant Results

The following major tasks were completed during the project. All the originally stated milestones were accomplished during the project period.

1. Review of literature on the various tasks considered for research in this project. A complete Bibliography is given at the end of the report.

2. Development of a MATLAB-Simulink™ code to simulate the dynamic performance of a U-tube steam generator (UTSG) in a typical 1,140 MWe PWR. This multi-nodal model was used to simulate the effects of tube fouling, tube plugging, leakage and other process-related phenomenon. The UTSG model is coupled to the whole plant system in

order to provide realistic simulation results. The nodal structure was expanded to account for spatial variations in the physical parameters. For example, the effect of fouling in the sub-cooled region has a higher influence on the steam pressure compared to a similar effect in the boiling region.

3. The high-fidelity nodal model of the UTSG was used to simulate the effects of fouling. Application of the group method of data handling (GMDH) method for process variable prediction. The model was used to generate a database representing normal and degraded process conditions.
4. Development of a laboratory heat exchanger system that was used to generate normal operation data and data under faulty device operation. This portable test rig was equipped with flow and pressure transmitters, flow meters, and thermocouples to measure fluid temperatures.
5. Development of a laboratory test module to simulate particulate fouling of HX tubes and its effect on overall thermal resistance. Application of the GMDH technique to predict HX fluid temperatures, and to compare with the calculated thermal resistance.
6. Development of a hybrid first principle and data-based model that was used to update and fine-tune the model using process data. Predictive artificial neural network and nonlinear data-driven models were used for process monitoring and diagnosis. The hybrid models were classified into serial hybrid and parallel hybrid models. The serial modeling exhibited a better performance in predicting process variables compared to the parallel modeling. A simple heat exchanger model was used for this study.
7. Development of a laboratory piezo-device sensor suite for structural monitoring and a data acquisition system for measuring both input excitation signal and the response signal. This uses metal flat plates and tubing specimen. The comparison of the input excitation signal (transmitted signal) and the signal received at another location in the plate show excellent frequency response characteristics. The frequency characteristics changed when there was a flaw in the plate (or tubing) such as a crack, inclusion, deposit, etc. This task included the review of elastic wave propagation in plates under normal and fault conditions. Experiments were performed in air, and in water with and without bubbly flow. A review of wireless and Internet signal transmission was also performed as part of this experiment.

8. Development of advanced signal processing and defect classification algorithms. The transient data were analyzed using time-frequency techniques such as the wavelet transforms and the Hilbert-Huang transform (HHT). The HHT was found to be highly effective in processing non-stationary and nonlinear signals from the piezo-transducers.
9. Development of a moving-window technique in the time domain for detecting and quantifying flaw types in tubular structures. A window zooming technique was also developed for flaw location in tubes.
10. Theoretical study of elastic wave propagation (longitudinal and shear waves) in metallic flat plates and tubing with and without flaws.
11. Simulation of Lamb wave propagation using the finite-element code ABAQUS. This enables the verification of the experimental results.
12. The following is a list of publications under this project. These were used for information dissemination.

12.1. B. Lu, B.R. Upadhyaya, and J.W. Hines, "Application of Hilbert-Huang Transform for Acoustic Signal Analysis for Steam generator Structural Integrity Diagnosis," Transactions of the American Nuclear Society, Vol. 91, November 2004.

12.2. B. Lu, B.R. Upadhyaya, and J.W. Hines, "Feature Extraction from Lamb Wave Signals for Structural Flaw Classification," Transactions of the American Nuclear Society, Vol. 90, pp. 64-65, June 2004.

12.3. B.R. Upadhyaya, J.W. Hines, B. Lu, and X. Huang, "Structural Integrity Monitoring of Nuclear Plant Steam Generators," Transactions of the American Nuclear Society, Vol. 89, pp. 481-482, November 2003.

12.4. B.R. Upadhyaya, B. Lu, J.W. Hines, and S.R.P. Perillo, "Defect Monitoring in Steam Generator Structures Using Piezoelectric Transducers and Time-Frequency Analysis," Transactions of the American Nuclear Society, Vol. 88, pp. 504-505, June 2003.

12.5. B. Lu, B.R. Upadhyaya, J.W. Hines, and S.R.P. Perillo, "Time-Frequency Analysis of Acoustic Signals for Flaw Monitoring in Steam Generator Structures, Proceedings of MARCON 2003, Knoxville, TN, May 2003.

12.6. X. Huang, B.R. Upadhyaya, and J.W. Hines, "Particulate Fouling and its Effects on U-Tube Steam Generator Thermal Performance," Proceedings of MARCON 2003, Knoxville, TN, May 2003.

12.7. B.R. Upadhyaya, J.W. Hines, X. Huang, N.A. Johansen, A.V. Gribok, and S.R.P. Perillo, “Automated Monitoring and Diagnostics of the Integrity of Nuclear Plant Steam Generators,” Transactions of the American Nuclear Society, Vol. 86, p. 188, 2002.

12.8. R.L. Penha, J.W. Hines, and B.R. Upadhyaya, "Application of Hybrid Modeling for Monitoring Heat Exchangers," Proceedings of ANES 2002, Miami, October 2002.

12.9. S.R.P. Perillo, B.R. Upadhyaya, and J.W. Hines, "Structural Monitoring of Steam Generators and Heat Exchangers Using Piezoelectric Devices," Proceedings of ANES 2002, Miami, October 2002.

12.10. S.R.P. Perillo and B.R. Upadhyaya, "Applications of Piezoelectric Devices in Engineering Systems," Proceedings of MARCON 2002, Knoxville, TN, May 2002.

12.11. R.L. Penha and J.W. Hines, “Hybrid System Modeling for Process Diagnostics,” Proceedings of MARCON 2002, Knoxville, TN, May 2002.

12.12. B. Lu, B.R. Upadhyaya, and R.B. Perez, “Structural Integrity Monitoring of Steam Generator Tubing Using Transient Acoustical Signal Analysis,” submitted for publication in IEEE Transactions on Nuclear Science, 2004.

1.3. Project Personnel

Principal Investigator:	B.R. Upadhyaya
Co-Principal Investigator:	J.W. Hines
Graduate Research Assistant:	B. Lu
	X. Huang
	K. Zhao
Visiting Scholars:	S.R. Perillo
	R.L. Penha

1.4. Outline of the Report - Volume 1

The review of steam generator degradation mechanisms and the current status of in-service inspection are presented in Section 2. The development of a simulation model of the UTSG and the results of simulating both normal and degraded operation are described in Section 3. Experimental studies on tube fouling are presented in Section 4. Section 5 presents the technique and the results of monitoring tube fouling using the GMDH approach. Section 6 presents the details of the hybrid modeling approach and the results of application

to a tubular heat exchanger. The development of data driven models from operational data and applications to a helical coil steam generator are described in Section 7. Concluding remarks on the tasks and results presented in Volume 1 of the report are summarized in Section 8. The report contains an extensive bibliography of literature review.

2. REVIEW OF DEGRADATION MECHANISMS IN NUCLEAR PLANT STEAM GENERATORS AND HEAT EXCHANGERS

2.1. Introduction

Pressurized water reactors (PWRs) use steam generators (SGs) to convert water into steam in the secondary side from heat produced in the reactor core (primary side). Figure 2.1 shows a simplified schematic of a recirculating-type nuclear steam generator [58]. The steam generators are large components, that measure up to 70 feet in height and weigh as much as 800 tons. Inside the steam generators, hot radioactive water is pumped through thousands of feet of tubing -- each steam generator can contain anywhere from 3,000 to 10,000 tubes, each about 0.75-inch diameter (the number of tubes depends on the type of SG, U-tube or once-through type) -- under high pressure. The water flowing through the inside of the tubes heats non-radioactive water on the outside of the tubes and converts the secondary water into steam. The steam (saturated or superheated) flows into several stages of a turbine that is coupled to electrical generators. The steam from the last stage of the turbine is condensed into water and is pumped back to the steam generator.

The steam generator tubes have an important safety role because they constitute one of the primary barriers between the radioactive and non-radioactive sides of the plant. For this reason, the integrity of the tubing is essential in minimizing the leakage of water between the two *sides* of the plant. There is the potential that if a tube ruptures during plant operation, radioactivity from the primary loop could escape directly to the atmosphere along with the steam.

Operating results show that about one-half of the PWR nuclear power plants in the world were plugging or sleeving steam generator tubes in any given year of the first half of 1990s. The total number of steam generator tubes plugged per year has ranged from about 10,000 to 12,000 tubes. Moreover, more than 48,000 steam generator tubes were sleeved as of December 1994. This indicates that it is of great significance to maintain the structural integrity of SGs for efficient electricity production and safe operation of nuclear power units. To achieve this goal, it is necessary to get a good understanding of steam generator flaws and degradation mechanisms.

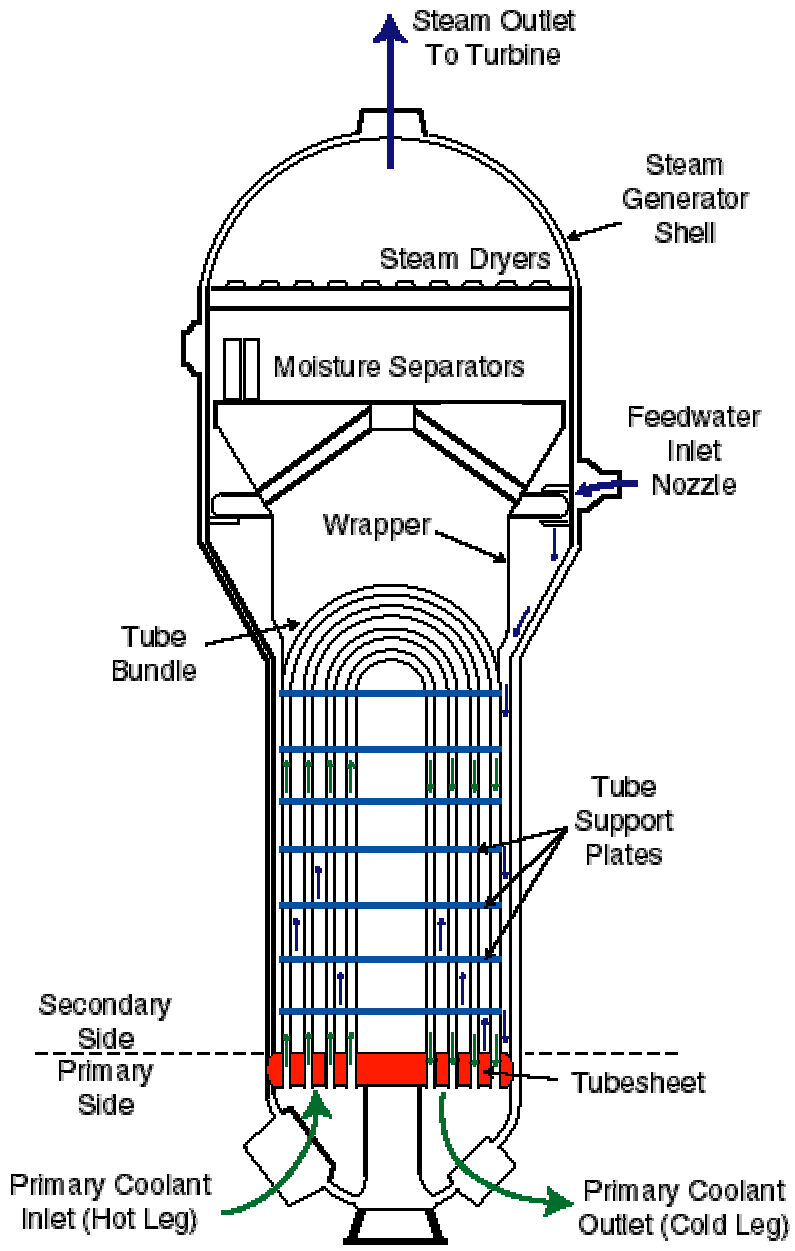

Figure 2.1. Simplified schematic of a recirculating type nuclear steam generator [Ref. 58].

2.2. Review of SG Defects and Degradation Mechanisms

An extensive literature review on SG defects and degradation mechanisms has been made [57-60]. The discussion in this section is taken from Ref. [58]. Generally, there exist various degradation modes for SG (mainly for the tubing). The degradation modes are somewhat different for UTSG and OTSG systems. However, the following modes are

generally true: (a) Stress Corrosion Cracking, (b) Intergranular attack (IGA), (c) Denting, (d) Pitting, (e) Fretting, Wear, and Thinning, (f) High-cycle Fatigue and Wastage. Fouling is often not regarded as a degradation mode of tubing. It may be regarded of as a degradation cause, which is influenced by other sources (water chemistry, impurities, etc). Fouling will be further discussed in the following section. From the point of view of SG integrity and heat transfer, fouling mainly results in SG degradation by changing the heat transfer. Almost all other degradation mechanisms lead to loss of structural integrity of the SG and also the degradation in the SG thermal performance. If they are severe enough they may initiate an accident, such as steam generator tube rupture (SGTR). Hence it is of great importance to monitor both the structural and process the integrity of steam generators.

Steam generator (SG) defects mainly include SG materials discontinuity, or loss of SG structural integrity and capability of normal heat transfer and steam generation. Dominant forms of SG degradation forms have changed over time. From the early time to mid-1970s, thinning of steam generator tube walls due to the chemistry of water flowing around them was the dominant cause of tube degradation. However, all plants have changed their water chemistry control programs since then, almost completely eliminating the problem with tube thinning.

After tube thinning, tube denting became a primary concern. Denting results from the corrosion of the carbon steel support plates and the buildup of corrosion product in the crevices between tubes and tube support plates. Measures have been taken to control denting, including changes in the chemistry of the secondary side, the non-radioactive side of the plant. But other phenomena continue to cause tube cracking.

Some of the newer steam generators have features that make the tubes less susceptible to corrosion-related damage. These include using stainless-steel tube support plates to minimize the likelihood of denting; new fabrication techniques to minimize mechanical stress on tubes; and the use of more corrosion-resistant tube materials, such as thermally treated Alloy 600 and Alloy 690. Though for different types of SGs, there exist some differences and characteristics in their degradation mechanisms, the following general categories of SG degradation mechanisms have been identified.

2.2.1. Stress Corrosion Cracking (SCC)

Stress corrosion cracking occurs under the combined action of corrosion and stress, either applied or residual. Depending on the metal and corrosive medium, the cracking may be either intergranular or transgranular. SCC can occur on both the primary (inside) and secondary (outside) sides of SG tubes, which are named respectively as PWSCC (Primary Water Stress Corrosion Cracking) and ODSCC (Outer Diameter Stress Corrosion Cracking). SCC increases in severity (frequency of occurrence and speed of crack growth) as stresses increase, as the environment becomes more severe (higher temperature, more aggressive chemical environment, etc.), and as the material susceptibility increases. Typical locations for SCC are at dents (see Figure 2.2), in the roll expansion regions at the tube sheet (see Figure 2.3), and in areas with concentrated impurities [58].

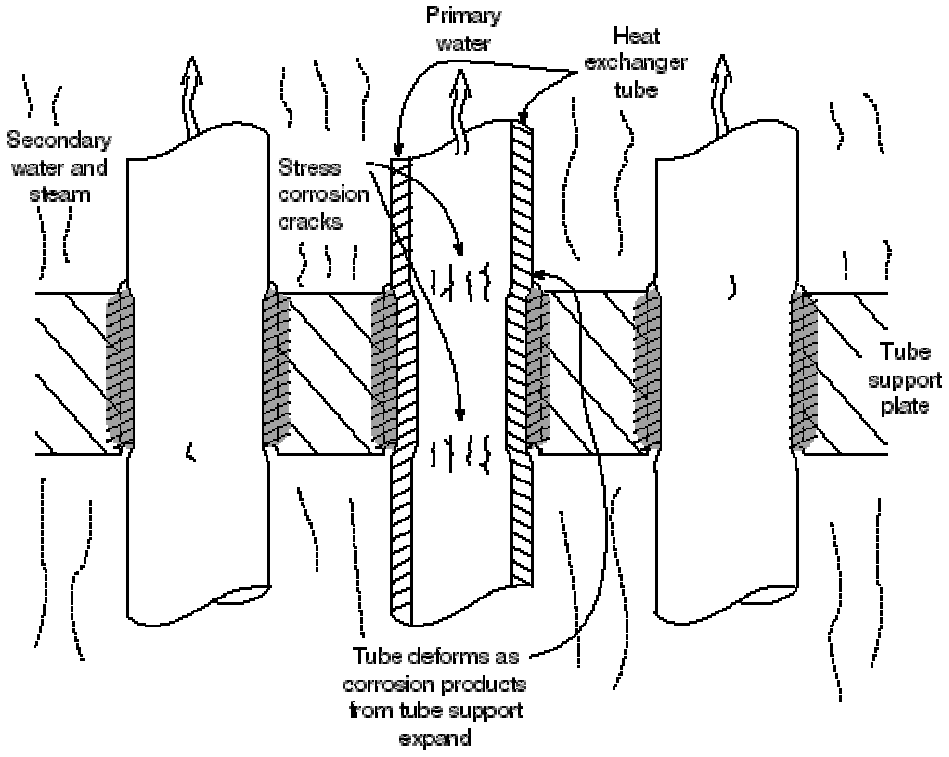

Figure 2.2. Illustration showing the typical locations for SCC occurring at dents [Ref. 58].

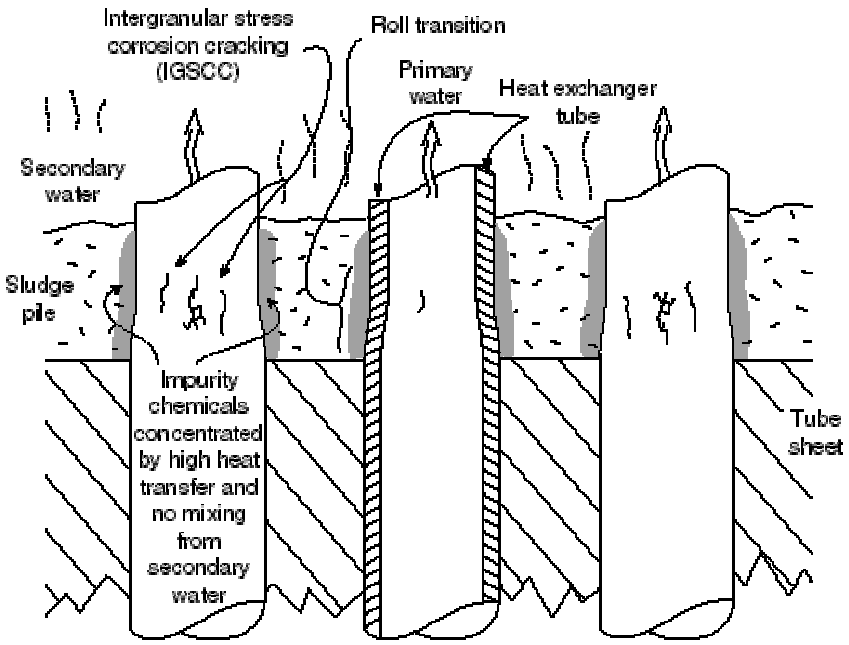

Figure 2.3. Illustration showing the typical locations for SCC occurring in the roll expansion regions at the tube sheet [Ref. 58].

2.2.2. Intergranular Attack (IGA)

Intergranular attack of SG tubes proceeds along the grain boundaries of the metal, starting at the surface on the secondary side (see Figure 2.4). It also occurs to a smaller extent on the primary side. This form of corrosion proceeds in the absence of stress, but may be accelerated by stress. IGA can occur both in sludge piles (see Figure 2.5) and in tube support regions, and it may be a precursor to subsequent intergranular stress corrosion cracking (IGSCC) [58].

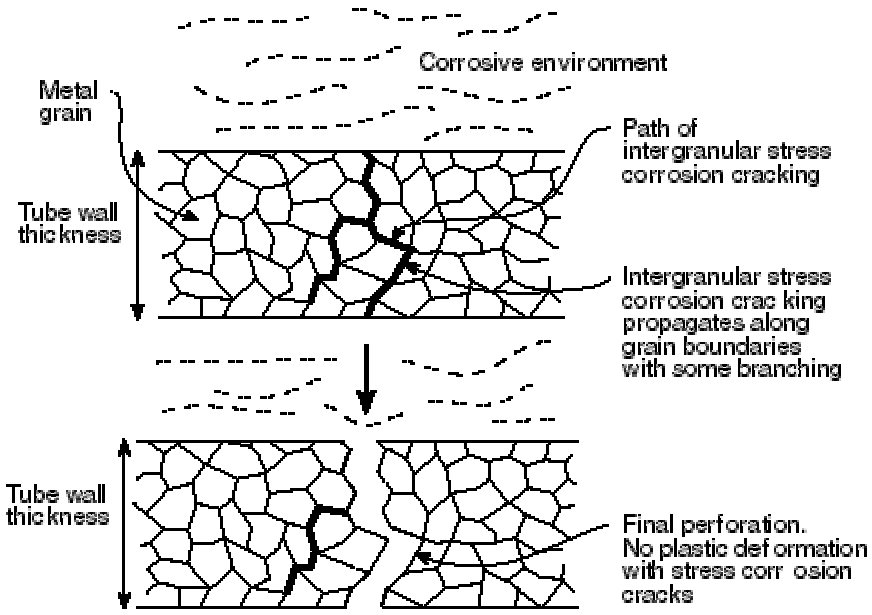

Figure 2.4. Illustration showing the intergranular attack of SG tubes starting at the surface on the secondary side [Ref. 58].

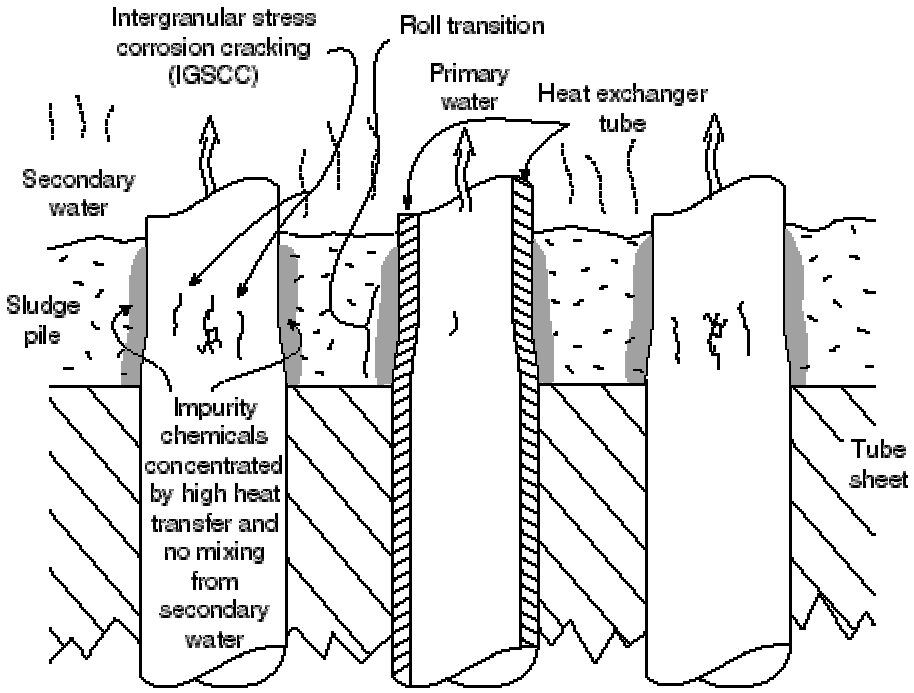

Figure 2.5. Illustration showing the intergranular attack of SG tubes near sludge piles [Ref. 58].

2.2.3. Denting

Denting is a process in which the SG tubes are squeezed inward and deformed at a carbon steel tube support plate intersection or within the tube sheet as a result of the corrosion of carbon steel supports, which produces a buildup of corrosion products between the tube support structure and the outer surface of the tube. Stresses are introduced and can lead to stress corrosion cracking and other types of tube failures (see Figure 2.6) [58].

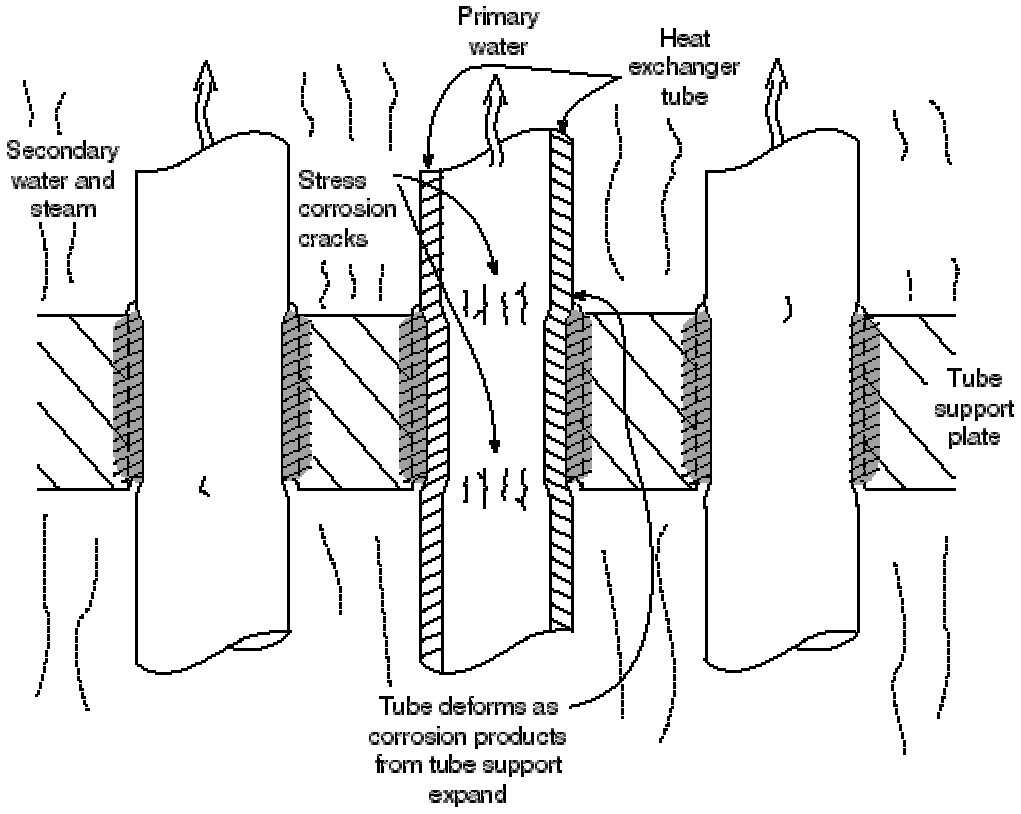

Figure 2.6. Illustration showing denting and other types of tube failures [Ref. 58].

2.2.4. Pitting

Pitting corrosion essentially acts like a chemical drill and is not focused on structural features such as grain boundaries (see Figure 2.7) [58]. This degradation has been observed on the secondary side of SG tubes in both the hot and cold legs, primarily on tube surfaces in the sludge piles in the cold leg. Pitting occurs because of the presence of oxidizing impurities (oxygen and copper) and acidic forming impurities (chloride and sulfate). Any

barriers to diffusion such as sludge accumulation on tube wall will accelerate the pitting process by enhancing the chemical concentrations.

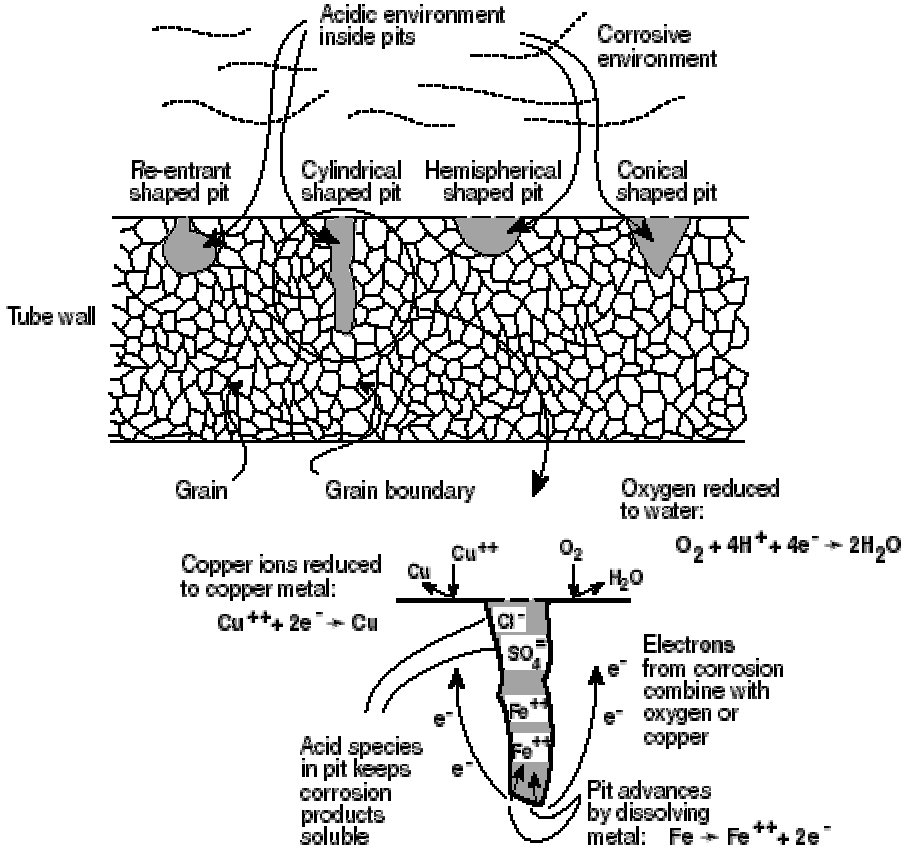

Figure 2.7. Illustration showing pitting degradation [Ref. 58].

2.2.5. Fretting, Wear, and Thinning

These steam generator degradation types are also broad characterized as mechanically-induced or *aided degradation mechanisms*. Degradation from small amplitude, oscillatory motion, between continuously rubbing surfaces, is generally termed fretting. Tube vibration of relatively large amplitude, resulting in intermittent sliding contact between tube and support, is termed sliding wear, or wear. Concurrent effects of vibration and corrosion generally cause thinning. However, thinning occurs at some locations where flow-induced vibrations are not expected, so it is not certain that tube motion is required for this mechanism; in some cases it may simply be the result of corrosion wastage.

The major stressor in fretting and wear is the flow-induced vibration. When anti-vibration bars (AVBs) are used in the U-bend regions of tube bundles of recirculating steam generators to stiffen the tubes and limit vibration amplitudes, the anti-vibration bar fretting/wear can occur.

2.2.6. High-Cycle Fatigue

The combination of high vibration amplitude and low strength may lead to catastrophic fatigue failures. Vibration occurs in steam generators with high recirculation flow factors (causing flow-induced vibrations in the U-bend region) and improper AVB support. A high mean stress (e.g. residual stress) or a tube defect (fretting mark or crack) significantly reduces the fatigue strength. Therefore, tubes with dents, fret marks, or cracks at the top tube support plate in U-bend region of the recirculating SGs are susceptible to high-cycle fatigue failure.

Wastage of the peripheral tubes near the lower support plates on the cold leg sides of the recirculating SGs in a few plants might also have been caused by acidic sulfates. Resin leakage from the condensate polisher beds could have produced the acidic sulfate environment. The phosphate corrosion or wastage is transgranular and may lead to significant thinning and, ultimately, to local ductile rupture and leakage. Phosphate wastage was the major cause of tube failures in PWR SGs until around 1976. However, it is no longer an active degradation mechanism in most of the PWR plants since phosphate water chemistry is no longer used in most plants.

2.2.7. Wastage

Wastage is the relatively uniform corrosion and thinning of a SG tube on its outside surface (secondary-side of the SG). This degradation tends to occur in relatively stagnant regions in recirculating SGs with secondary-side phosphate water chemistry. These regions include the tube-to-tube sheet crevices, the tube-to-tube support plate annuli, and the sludge pile on the tube sheet, or the short radius U-bends in the vicinity of AVBs.

Table 1 gives a summary of PWR recirculating steam generator tube degradation mechanisms [59].

2.3. Review of Fouling in Heat Exchangers and Steam Generators

There is an extensive amount of literatures on fouling [62-73]. Over the past several years, an increasing number of pressurized water reactor (PWR) plants have begun to experience degradation in steam generator thermal performance, which is often manifested as a decrease in SG steam pressure during operation. Such degradation can result in costly reductions in the electrical generating capacity of the plant. Even a 1% decrease in electrical generation approximately corresponds to $2 million in lost revenues per year for a typical PWR. Numerous causes of SG thermal performance degradation have been identified, including primary and secondary tube fouling, dryer clogging, flow resistance due to scaling, and tube plugging and sleeving. Hence, fouling-related degradation is one of the major problems in steam generators as well as in heat exchangers. Therefore in this research, we focused part of our effort for the study of fouling, including a literature review, modeling, experimental study, and monitoring and diagnosis of fouling using the GMDH method.

Table 1. Summary of PWR recirculating steam generator tube degradation processes

Rank[a]	Degradation Mechanism	Stressor	Degradation Sites	Potential Failure Mode	ISI Method
1	ODSCC	Tensile stresses, impurity concentrations, sensitive materials	• Tube-to-tubesheet crevices • Sludge Pile • Tube support plate • Free span	Axial or circumferential crack Circumferential crack Axial crack Axial crack	MRPC MRPC/Cecco 5 Bobbin coil/ Cecco 5 Bobbin coil (in absolute mode)
2	PWSCC	Temperature, residual tensile stresses, sensitive materials (low mill anneal temperature)	• Inside surface of U-bend • Roll transition w/o kiss rolling • Roll transition with kiss rolling • Dented tube regions	Mixed Crack Mixed Crack Axial Crack Circumferential crack	MRPC[b] MRPC MRPC Bobbin coil or MRPC
3	Fretting, Wear	Flow induced vibration, aggressive chemicals	• Contact points between tubes and the AVBs, or tubes and the preheater baffles • Contact Between tubes and loose parts • Tube-to-tube contact	Local wear Depends on loose part geometry Axial Wear	Bobbin coil Bobbin coil Bobbin coil
4	High-cycle fatigue	High mean stress level and flow induced vibration, initiating defect (crack, dent, pit, etc.)	At the upper support plate if the tube is clamped	Transgranular circumferential cracking	Leak detection or by detection of precursor
5	Denting	Oxygen, copper oxide, chlorides, temperature, PH, crevice condition, deposits	At the tube support plates, in the sludge pile, in the tubesheet crevices	Flow blockage in tube, may lead to circumferential cracking (see PWSCC), decreases in fatigue resistance	Profilometry, Bobbin coil
6	Pitting	Brackish water, chlorides, sulfates, oxygen, copper oxides	Cold leg in sludge pile or where scale containing copper deposits is found, under deposit pitting in hot leg	Local attack and tube thinning, may lead to a hole	Bobbin coil, ultrasonics
7	Wastage	Phosphate chemistry, chloride concentration, resin leakage	Tubesheet crevices, sludge pile, tube support plates, AVBs	General thinning	Bobbin coil

[a] Based on operating experience and number of defects (as of 1993).
[b] Multi-frequency rotating pancake coil probe.

2.3.1. Definition of Fouling

Fouling is generally defined as the accumulation of unwanted materials on the surfaces of processing equipment. It has been recognized as a nearly universal problem in design and operation and affects the operation of equipment in two ways:

- *The fouling layer has a low thermal conductivity. This increases the resistance to heat transfer and reduces the effectiveness of heat exchangers and steam generators.*
- *As deposition occurs, the cross-sectional area is reduced, which causes an increase in pressure drop across the apparatus.*

Heat exchangers and SGs are designed for counteracting the effect of fouling by providing excess heat transfer capacity in order to offset the losses in efficiency caused by fouling. That is, the thermal resistance due to fouling, R_f, is included in the equation for the overall heat transfer coefficient as follows:

$$\frac{1}{U_o A_o} = \frac{1}{\alpha_o A_o} + \frac{R_{f-i}}{A_i} + \frac{R_w}{A_w} + \frac{R_{f-o}}{A_o} + \frac{1}{\alpha_i A_i} \qquad (2.1)$$

U_o= overall heat transfer coefficient based on outside area of tube wall
A = tube wall area
A_w = mean wall area
R_f = thermal resistance due to fouling
R_w = thermal resistance of wall
α = convective heat transfer coefficient.

As deposit thickness or R_f increases with time, U_o decreases. The thermal fouling resistance, R_f, is defined as:

$$R_f = \frac{1}{U_o(t=t)} - \frac{1}{U_o(t=0)} \qquad (2.2)$$

The overall heat transfer coefficient determines how much heat can be transferred between the hot and the cold fluid in a given heat exchanger. When it falls below a tolerable value, the heat exchanger will have to be serviced.

2.3.2. Fouling Mechanism

According to the mechanism responsible for deposit generation, fouling has been classified into crystallization fouling, particulate fouling, chemical reaction fouling, corrosion fouling, and biological fouling (bio-fouling).

- ***Crystallization fouling*** *is the deposition of a solid layer on a heat transfer surface, mainly resulting from the presence of dissolved inorganic salts in the flowing solution which become supersaturated under process conditions. Typical scaling problems are calcium carbonate, calcium sulphate, and silica deposits.*
- ***Particulate fouling*** *is the accumulation of solid particles suspended in a fluid onto a heat transfer surface. Suspended particles can be ambient pollutants (sand, silt, clay), upstream corrosion products, or products of chemical reactions occurring within the fluid.*
- ***Chemical reaction fouling*** *involves deposits that are formed as the results of chemical reactions at the heat transfer surface. The heat exchanger surface material does not react itself, although it may act as a catalyst. This kind of fouling is a common problem in chemical process industries, oil refineries, and dairy plants.*
- ***Corrosion fouling*** *occurs when the heat exchanger material reacts with the fluid to form corrosion products on the heat transfer surface.*
- ***Biological fouling*** *is the development and deposition of organic films consisting of micro-organisms and their products (microbial fouling) and the attachment and growth of macro-organisms, such as barnacles or mussels (macrobial fouling).*

Generally, several fouling mechanisms occur at the same time, nearly always being mutually reinforcing. The above fouling mechanisms generally occur in five consecutive steps:

1. *Initiation or delay period: When a new or cleaned heat exchanger is put into operation, the initially high heat transfer coefficients may remain unchanged for some time. This delay period can vary from a few seconds to several days. According to research results of Müller-Steinhagen and co-workers, no delay period occurs for particulate fouling.*
2. *Mass transport: To form a deposit at the heat transfer surface, at least one key component has to be transported to it from the bulk fluid. In most cases, this occurs by diffusion.*
3. *Formation of the deposit: After the foulant has been transported to the heat transfer surface, it must stick to the surface or react to give the deposit forming substance.*
4. *Removal or auto-retardation: Depending on the strength of the deposit, erosion occurs immediately after the first deposit has been laid down. Furthermore, several mechanisms exist which cause auto-retardation of the deposition process.*
5. *Aging: Every deposit is subjected to this stage. This can increase the deposit strength by, for example, polymerization, recrystallization, or dehydration. Biological deposits weaken with time due to contamination of organisms.*

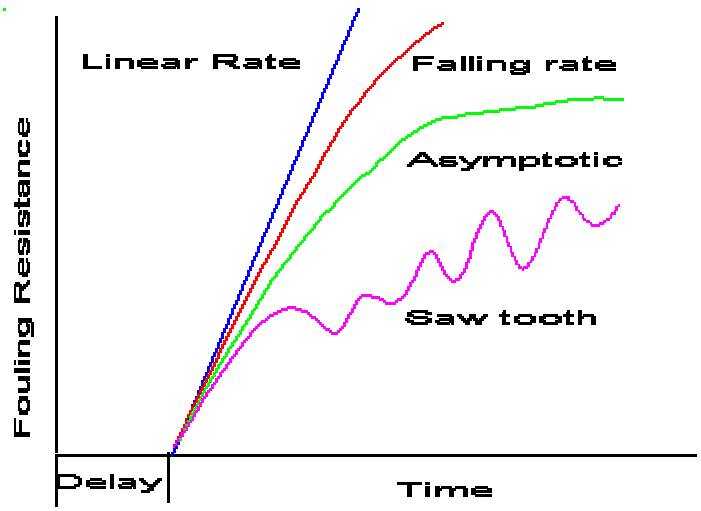

Figure 2.8. Different cases of fouling rate.

Depending on the process parameters and the dominant fouling mechanism, the fouling rate will either be constant or decrease with time.

- *Linear rate: R_f increases with time or the growth rate of deposit is constant. This is the result of hard and adherent deposit where removal and aging can be ignored.*
- *Falling rate: R_f increases with time, but with a progressively falling rate or the removal rate increases with time.*
- *Asymptotic rate: After a period of time, R_f reaches a constant value or the growth rate of deposit approaches zero.*
- *Saw-tooth fouling: Part of the deposit is detached after a critical residence time or once a critical deposit thickness has been reached. The fouling layer then builds up and breaks off again.*

2.3.3. Mitigation or Control of Fouling

Owing to the enormous costs associated with fouling, a considerable number of fouling mitigation strategies have been developed. Fouling is a function of many variables. For example, fouling in crude oil exchangers is affected by the following variables: crude oil composition, inorganic contaminants, process conditions (temperature, pressure, flow rate), exchanger and piping configuration, and surface temperature. Therefore effective control of the variables in certain conditions may minimize fouling. Generally, effective fouling control methods should involve:

- *Preventing foulant formation*
- *Preventing foulant from adhering to themselves and to heat transfer surfaces*
- *Removal of deposits from the surfaces.*

Experiences have shown that steps can be taken to prevent or mitigate the impact of fouling problems during the following phases: plant design, plant construction, plant operation, and plant maintenance.

The following techniques are implemented to mitigate or control fouling: reduction of foulant concentration, use of chemical additives, mechanical on-line mitigation strategies, high flow rate and low surface temperature, chemical or mechanical cleaning

of fouled process equipment, surface coatings and treatments, ultraviolet, acoustic, magnetic, electric and radiation treatment, etc.

2.3.4. Heat Exchanger or SG Degradation Models

The degradation models are those that define the relationships between the characterization variable (for example, steam pressure change, tube wear rate, etc.) and the contributors or stressors (thermal fouling resistance, contact forces, contact time, coefficient of friction, etc) of the defects. These models can be used to predict the reliability or residual lifetime of tubing in heat exchangers and SGs.

Even though there are various degradation models for SG residual lifetime prediction, which could be used by the nuclear industry, the Nuclear Regulatory Commission (NRC) has not yet approved any one of these as the standard method. This may be due to the fact that the SG degradations are so complex that up to now no single model can characterize all the degradation mechanisms very well.

Based on parametric study of the UTSG thermal-hydraulic model, Naghedolfeizi and Upadhyaya [5] determined that a quadratic function provides the best statistical fit to the trends of steam pressure variation as a function of the overall heat transfer coefficient.

$$\Delta P = a_0 + b_0 U_n + c_0 U_n^2 \qquad (2.3)$$

ΔP is the SG steam pressure deviation from the set point and U_n is the reduction in the heat transfer coefficient. By combining the above equation with the fouling model (for example an exponential function), the following model [12] may be obtained and applied to predict tube residual life.

$$\Delta P = \alpha_0 + \alpha_1 t + \alpha_2 t^2, \text{ where t is time.} \qquad (2.4)$$

One of the statistical techniques used by some engineers is the Weibull probability distribution, which has been successfully used to describe the statistics of material failure caused by fatigue and stress corrosion cracking [59]. Reference [58] emphasized the Weibull distribution with two-parameter distribution given by

$$F(t) = 1 - \exp[-(t/t_\tau)^b] \qquad (2.5)$$

F(t) is the cumulative fraction of tubes "failed" by a given degradation mechanism, t is the time of operation, t_τ is the characteristic time of the Weibull probability distribution, and b is the slope of the distribution when plotted on a Weibull probability graph.

Kern and Seaton [63] were among the first researchers to conduct a systematic investigation of particulate fouling. They reviewed many experimental particulate fouling data from recovery heat exchangers and noticed that they all repeat the same type of asymptotic deposition trend. After Kern and Seaton, many investigators tried to develop a general model for particulate deposition on heat exchanger tubing surfaces, but there was little general agreement on predicting particulate fouling [64].

The reason why there has not been a general predictive model for particulate deposition until recently is that the interaction between particulates and fluid flow is very complex, especially in the turbulent flow field. In the heat exchanger industry, the fact that there is a temperature gradient between the flow field and the heat exchanger surface makes the problem of predicting a theoretical model for particulate deposition very complex.

In a more recent experimental investigation on particulate fouling in heat exchangers, a generalized model has been developed. The effect of operational variables such as flow, velocity, surface temperature, and fluid bulk temperature on particle deposition has been measured. Details of the models are as follows.

Kern and Seaton's model, which was based on the deposit removal rate concept, did not include the thermal or particle size effects.

$$R_f(t) = \frac{K_1 UC}{K_2 \lambda_d \tau_W}(1 - e^{-K_2 \tau_W t}) = R_f * (1 - e^{-bt}) \tag{2.6}$$

Watkinson and Epstein introduced a sticking probability to the particles and redefined the Kern-Seaton model and came up with the following model [64].

$$R_f(t) = \frac{K_3 C \beta e^{-E/RT_S}}{K_4 \lambda_d {\tau_W}^2}(1 - e^{-K_4 \tau_W t}) \tag{2.7}$$

$$\beta = \frac{U(f/8)^{1/2}}{11.8 {S_C}^{2/3}} \tag{2.8}$$

Muller-Steinhagen [64] included the influence of wall temperature and the fouling behavior of their equation is given as

$$R_f(t) = \frac{K_5 C \beta e^{-E/RT_S}}{K_6 \lambda_d \tau_W} \tag{2.9}$$

For adhesion controlled particles on heat transfer surface the fouling resistance given by [64]

$$R_f(t) = \frac{K_7 fCe^{-E/RT_S}}{K_8 \lambda_d \tau_W}(1 - e^{-K_8 \tau_W t}) \tag{2.10}$$

The thermophoretic effect is the effect of surface temperature on the deposition of submicron particles which acts in the direction of the temperature gradients. Thus a high

surface temperature will repel particles while a cold surface will attract them. The effect of surface temperature is more pronounced for gas particle systems than for liquids.

Muller-Steinhagen [64] reported the following model for particle deposition rate:

$$m_d = (\beta - V_t / 2)C - (\beta + V_t / 2)C_W \quad (2.11)$$

V_t is the thermophoretic velocity and is defined as

$$V_t = \frac{0.26}{2\lambda_l + \lambda_p} * \frac{\nu_l q}{T} \quad (2.12)$$

Within the limited range of experimental data the general agreement between the data and the predicted model is fairly satisfactory. The nomenclatures are as follows [14]:

C = Bulk particle concentration kg/kg
C_W = Particle concentration near the solid-liquid interface kg/kg
E = Activation Energy, J/mol
f = Moody friction factor
m_d = Deposition flux, kg/m^2.S
q = Heat Flux, W/m^2
R_f = Fouling resistance, m^2.k/W
R_f* = Asymptotic fouling resistance m^2.K/W
R = Universal gas constant
Sc = Schmidt number = V^1/D
t = time, sec
T_s = Temperature at liquid-solid interface ˚C
U = Flow velocity, m/s
V_t = Thermophoretic velocity, m/s
ß = Mass transfer coefficient, m/s
λ_d = Thermal conductivity of deposit
λ_l = Thermal conductivity of liquid W/m.K
λ_p = Thermal conductivity of particles W/m.K
ν_l = Kinematic viscosity of liquid, m^2/s
τ_W = Wall shear stress, N/m^2
K1,...,K8 = Constants.

In the simulation of fouling in this study, we use the fouling factor to take into account the fouling effect. Generally the fouling factor must be obtained experimentally by determining the values of U for both clean and dirty conditions in the heat exchanger. The fouling factor is thus defined as:

$$R_f = 1/U_{dirty} - 1/U_{clean} \tag{2.13}$$

According to the "Standard of Tubular Exchanger Manufacturers Association," 4th ed., 1959, for treated boiler feed water above 125°F, the fouling factor is 0.001 $h \cdot ft^2 \cdot °F/Btu$ or 0.0002 $m^2 \cdot °C/W$.

3. DEVELOPMENT OF A MULTI-NODAL DYNAMIC MODEL OF A U-TUBE STEAM GENERATOR (UTSG)

3.1. Assumptions in the Development of a Steam Generator (SG) Model

A multi-nodal simulation model was developed for a typical recirculating type U-tube steam generator (UTSG). The general arrangement of a UTSG is shown in Figure 3.1. The primary coolant enters the steam generator through an inlet nozzle at the bottom of the inlet plenum. The coolant flows inside the U-tube, first upward and then downward, and thus transfers heat to the secondary fluid in the shell side of the SG. The primary fluid leaves the outlet plenum through an outlet nozzle connected to the cold leg piping. In the SG shown in Figure 3.1, the feedwater enters the downcomer shell at a level just above the U-tube region. It flows down through an annulus inside the shell and mixes with water coming from the drum section. The water enters the tube bundle region where heat is transferred to the fluid. As it flows over the outside of the U-tubes, a mixture of steam and water is formed. The mixer enters the riser region where the nozzle effect increases the natural driving force. As the flow passes through the separator region, water is removed from the steam and is returned to the drum section. The steam leaving the separator passes through steam dryers and exits the steam generator with a quality of almost 100%.

A typical 1,300 MWe four-loop Westinghouse nuclear plant has about 3,400 U-tubes per SG. The Inconel stainless steel tubing has an outer diameter of 0.875 inch with a tube metal thickness of 0.05 inch. The height of U-tubes is ≈ 36 feet. The nominal steam pressure is 850 psia with a saturation temperature of 522 °F. The feed water has an inlet temperature of 434 °F and a flow rate of ≈ 3.73×10^6 *lbm/hr*.

The objective is to divide the tube length into a number of axial nodes so as to simulate tube fouling at different axial locations. The simulation may be made by varying heat transfer areas, flow rates, and heat transfer coefficients. The latter include film heat transfer coefficient of primary water in tubes, film heat transfer coefficient of secondary sub-cooled water, film heat transfer coefficient of secondary boiling water, and metal tube conductivity.

The model may be used to simulate dynamic behavior of thermal and hydraulic processes in a UTSG system. The simulation model has been developed based on the conservation equations (mass, energy, and momentum) and constitutive relationships. The following assumptions are made in model development.

- Both water and steam are considered to be saturated.
- Density and specific heat capacity of the feed water, sub-cooled region, and the primary side are assumed to be constant.
- Heat transfer coefficients are constant.
- Steam leaving the steam generator is 100% saturated.
- Heat transfer between the downcomer and the tube bundle regions is negligible.

The thermodynamic properties of the saturated water and steam are assumed to be linear functions of the steam pressure for a range of ± 100 *psi* from the normal operating point. The steam flow leaving the UTSG is considered to be a critical flow. The flow is defined in terms of steam pressure and steam valve coefficient as

$$W_s = C_l P \tag{3.1}$$

W_s = steam flow rate, C_l = steam valve coefficient, P = steam pressure.

Figure 3.1 shows the schematic of the nodal model representation. The steam generator water level is controlled by a three-element controller that uses the measurements of the SG water level, steam flow rate, and feed water flow rate. The forcing functions of the

isolated UTSG model are: primary inlet temperature, steam valve coefficient, feed water temperature, and SG level set point. The equations describing the nonlinear model of the UTSG are presented in Section 3.2.

3.2. Describing Equations for the Multi-Nodal Simulation Model

1. Primary Side

1.1 Inlet Plenum: (Nodes 1 and 2)

$$\frac{dT_{pi}}{dt} = \frac{W_{pi}}{M_{pi}}(\theta_i - T_{pi})$$

where $L_{s2}=(L-L_{s1})/3$.

$$\frac{dT_{p2}}{dt} = \frac{W_{pi}}{\rho_{pi}A_pL_{s2}}(T_{p1}-T_{p2}) + \frac{U_{pm2}S_{pm2}}{M_{p2}C_{p2}}(T_{m2}-T_{p2}) + \frac{T_{p2}-T_{p1}}{L_{s2}}\frac{dL_{s1}}{dt}$$

1.2 U-tube Primary Lump Equations: (Nodes 3 and 4)

$$\frac{dT_{p3}}{dt} = \frac{W_{pi}}{\rho_{pi}A_pL_{s2}}(T_{p2}-T_{p3}) + \frac{U_{pm3}S_{pm3}}{M_{p3}C_{p3}}(T_{m3}-T_{p3}) + \frac{2(T_{p3}-T_{p2})}{3L_{s2}}\frac{dL_{s1}}{dt}$$

$$\frac{dT_{p4}}{dt} = \frac{W_{pi}}{\rho_{pi}A_pL_{s2}}(T_{p3}-T_{p4}) + \frac{U_{pm4}S_{pm4}}{M_{p4}C_{p4}}(T_{m4}-T_{p4}) + \frac{T_{p4}-T_{p3}}{3L_{s2}}\frac{dL_{s1}}{dt}$$

Nodes 5 and 6:

$$\frac{dT_{p5}}{dt} = \frac{W_{pi}}{\rho_{pi} A_p L_{s2}} (T_{p4} - T_{p5}) + \frac{U_{pm5} S_{pm5}}{M_{p5} C_{p5}} (T_{m5} - T_{p5})$$

$$\frac{dT_{p6}}{dt} = \frac{W_{pi}}{\rho_{pi} A_p L_{s2}} (T_{p5} - T_{p6}) + \frac{U_{pm6} S_{pm6}}{M_{p6} C_{p6}} (T_{m6} - T_{p6}) + \frac{T_{p5} - T_{p6}}{3L_{s2}} \frac{dL_{s1}}{dt}$$

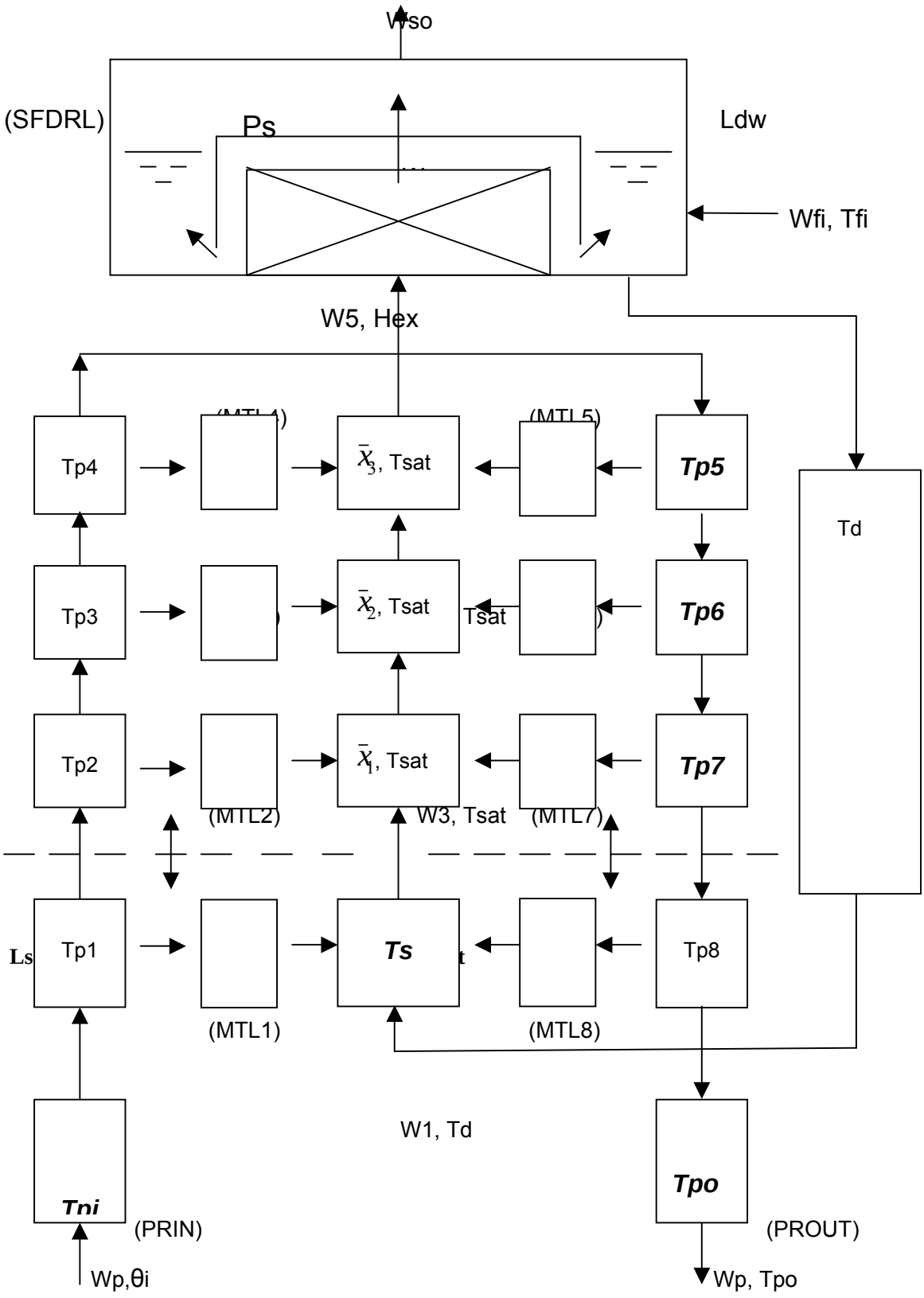
Wso
(SFDRL)
Ps
Ldw
Wfi, Tfi
W5, Hex
Tp4
Tp3
Tp2
Tp1
Tpi
(PRIN)
Wp,θi
(MTL1)
(MTL2)
(MTL5)
(MTL7)
(MTL8)
$\bar{X}_3$, Tsat
$\bar{X}_2$, Tsat
$\bar{X}_1$, Tsat
W3, Tsat
Tsat
Tp5
Tp6
Tp7
Tp8
Ts
Td
W1, Td
Tpo
(PROUT)
Wp, Tpo
Ls

Figure 3.1. Schematic of the U-Tube Steam Generator model with four axial tube nodes.

Node 7:

$$\frac{dT_{p7}}{dt}=\frac{W_{pi}}{\rho_{pi}A_pL_{s2}}(T_{p6}-T_{p7})+\frac{U_{pm7}S_{pm7}}{M_{p7}C_{p7}}(T_{m7}-T_{p7})+\frac{2(T_{p6}-T_{p7})}{3L_{s2}}\frac{dL_{s1}}{dt}$$

Node 8:

$$\frac{dT_{p8}}{dt}=\frac{W_{pi}}{\rho_{pi}A_pL_{s1}}(T_{p7}-T_{p8})+\frac{U_{pm8}S_{pm8}}{M_{p8}C_{p8}}(T_{m8}-T_{p8})+\frac{T_{p7}-T_{p8}}{L_{s1}}\frac{dL_{s1}}{dt}$$

1.3 Outlet Plenum:

$$\frac{dT_{po}}{dt}=\frac{W_{pi}}{M_{po}}(T_{p8}-T_{po})$$

2. Tube-wall Equations

$$\frac{dT_{m1}}{dt}=\frac{U_{pm1}S_{pm1}}{M_{m1}C_m}T_{p1}-\frac{U_{pm1}S_{pm1}+U_{ms1}S_{ms1}}{M_{m1}C_m}T_{m1}+\frac{U_{ms1}S_{ms1}}{M_{m1}C_m}\cdot\frac{T_d+T_{sat}}{2}+\frac{T_{m2}-T_{m1}}{2L_{s1}}\cdot\frac{dL_{s1}}{dt}$$

Node 1:

Node 2:

$$\frac{dT_{m2}}{dt}=\frac{U_{pm2}S_{pm2}}{M_{m2}C_m}(T_{p2}-T_{m2})-\frac{U_{ms2}S_{ms2}}{M_{m2}C_m}(T_{m2}-T_{sat})+\frac{T_{m2}+2T_{m3}-3T_{m1}}{2(L_0-L_{s1})}\cdot\frac{dL_{s1}}{dt}$$

Node 3:

$$\frac{dT_{m3}}{dt}=\frac{U_{pm3}S_{pm3}}{M_{m3}C_m}(T_{p3}-T_{m3})-\frac{U_{ms3}S_{ms3}}{M_{m3}C_m}(T_{m3}-T_{sat})+\frac{T_{m3}+T_{m4}-2T_{m2}}{2(L_0-L_{s1})}\cdot\frac{dL_{s1}}{dt}$$

Node 4:

$$\frac{dT_{m4}}{dt}=\frac{U_{pm4}S_{pm4}}{M_{m4}C_m}(T_{p4}-T_{m4})-\frac{U_{ms4}S_{ms4}}{M_{m4}C_m}(T_{m4}-T_{sat})+\frac{T_{m4}-T_{m3}}{2(L_0-L_{s1})}\cdot\frac{dL_{s1}}{dt}$$

Node 5:

$$\frac{dT_{m5}}{dt}=\frac{U_{pm5}S_{pm5}}{M_{m5}C_m}(T_{p5}-T_{m5})-\frac{U_{ms5}S_{ms5}}{M_{m5}C_m}(T_{m5}-T_{sat})+\frac{T_{m5}-T_{m6}}{2(L_0-L_{s1})}\cdot\frac{dL_{s1}}{dt}$$

Node 6:

$$\frac{dT_{m6}}{dt}=\frac{U_{pm6}S_{pm6}}{M_{m6}C_m}(T_{p6}-T_{m6})-\frac{U_{ms6}S_{ms6}}{M_{m6}C_m}(T_{m6}-T_{sat})+\frac{T_{m5}+T_{m6}-2T_{m7}}{2(L_0-L_{s1})}\cdot\frac{dL_{s1}}{dt}$$

Node 7:

$$\frac{dT_{m8}}{dt}=\frac{U_{pm8}S_{pm8}}{M_{m8}C_m}(T_{p8}-T_{m8})-\frac{U_{ms8}S_{ms8}}{M_{m8}C_m}(T_{m8}-\frac{T_d+T_{sat}}{2})+\frac{T_{m7}-T_{m8}}{2L_{s1}}\cdot\frac{dL_{s1}}{dt}$$

Node 8:

$$\frac{dT_{m7}}{dt}=\frac{U_{pm7}S_{pm7}}{M_{m7}C_m}(T_{p7}-T_{m7})-\frac{U_{ms7}S_{ms7}}{M_{m7}C_m}(T_{m7}-T_{sat})+\frac{2T_{m6}+T_{m7}-3T_{m8}}{2(L_0-L_{s1})}\cdot\frac{dL_{s1}}{dt}$$

3. Secondary Side Equations

3.1 Sub-cooled region equations

Mass Balance:

$$\frac{dL_{s1}}{dt}=\frac{W_1-W_2}{\rho_{s1}A_{fs}}$$

Energy Balance:

$$\frac{d}{dt}(\rho_{s1}A_{fs}L_{s1}C_{psub}\frac{T_d+T_{sat}}{2})=P_{r2}L_{s1}[U_{ms1}(T_{m1}-\frac{T_d+T_{sat}}{2})+U_{ms8}(T_{m8}-\frac{T_d+T_{sat}}{2})]+W_1C_{psub}T_d-W_2C_{psub}T_{sat}$$

3.2 Boiling region equations

Node 1:

Mass Balance:

$$\frac{d}{dt}(\rho_{b1}A_{fs}L_{s2})=W_2-W_3$$

$$\frac{d}{dt}\rho_{b1}=-\frac{K_1+K_2\frac{X_{e1}}{2}}{(V_f+\frac{X_{e1}}{2}V_{fg})^2}\frac{dP}{dt}-\frac{V_{fg}}{2(V_f+\frac{X_{e1}}{2}V_{fg})^2}\frac{dX_{e1}}{dt}$$

Energy Balance:

$$\frac{d}{dt}(\rho_{b1}A_{fs}L_{s2}h_{b1})=P_{r2}L_{s2}[U_{ms2}(T_{m2}-T_{sat})+U_{ms7}(T_{m7}-T_{sat})]+W_2h_f-W_3h_{ex1}$$

Node 2:

$$\frac{d}{dt}(\rho_{b2} A_{fs} L_{s2}) = W_3 - W_4$$

$$\frac{d}{dt}\rho_{b2} = -\frac{K_1 + K_2 \dfrac{X_{e1} + X_{e2}}{2}}{(V_f + \dfrac{X_{e1} + X_{e2}}{2} V_{fg})^2} \frac{dP}{dt} - \frac{V_{fg}}{2(V_f + \dfrac{X_{e1} + X_{e2}}{2} V_{fg})^2} (\frac{dX_{e1}}{dt} + \frac{dX_{e2}}{dt})$$

Mass Balance:

Energy Balance:

$$\frac{d}{dt}(\rho_{b2} A_{fs} L_{s2} h_{b2}) = P_{r2} L_{s2} [U_{ms3}(T_{m3} - T_{sat}) + U_{ms6}(T_{m6} - T_{sat})] + W_3 h_{ex1} - W_4 h_{ex2}$$

Node 3:

Mass Balance:

$$\frac{d}{dt}(\rho_{b3} A_{fs} L_{s2}) = W_4 - W_5$$

$$\frac{d}{dt}\rho_{b3} = -\frac{K_1 + K_2 \dfrac{X_{e2} + X_{e3}}{2}}{(V_f + \dfrac{X_{e2} + X_{e3}}{2} V_{fg})^2} \frac{dP}{dt} - \frac{V_{fg}}{2(V_f + \dfrac{X_{e2} + X_{e3}}{2} V_{fg})^2} (\frac{dX_{e2}}{dt} + \frac{dX_{e3}}{dt})$$

Energy Balance:

$$\frac{d}{dt}(\rho_{b3} A_{fs} L_{s2} h_{b3}) = P_{r2} L_{s2} [U_{ms4}(T_{m4} - T_{sat}) + U_{ms5}(T_{m5} - T_{sat})] + W_4 h_{ex2} - W_5 h_{ex3}$$

4. Drum Region Equations

4.1 Riser/Separator Volume

$$\frac{d}{dt}(V_r \rho_r) = W_5 - W_6$$

$$\frac{d}{dt}\rho_r = -\frac{K_1 + K_2 X_{e3}}{(V_f + X_{e3} V_{fg})^2} \frac{dP}{dt} - \frac{V_{fg}}{(V_f + X_{e3} V_{fg})^2} \frac{dX_{e3}}{dt}$$

4.2 Drum Water Volume

$$\frac{d}{dt}(\rho_{dw}A_{dw}L_{dw}) = W_{fi} + (1 - X_{e3})W_6 - W_1$$

Mass Balance:

Energy Balance:

$$\frac{d}{dt}(\rho_{dw}A_{dw}L_{dw}T_{dw}) = W_{fi}T_{fi} + (1 - X_{e3})W_6T_{sat} - W_1T_{dw}$$

4.3 Drum Steam Volume

$$(V_{dr} - A_{dw}L_{dw})\frac{d\rho_g}{dt} - \rho_g A_{dw}\frac{dL_{dw}}{dt} = X_{e3}W_6 - C_lP$$

5. Downcomer Region Equations

$$\frac{dT_d}{dt} = \frac{W_1}{M_d}(T_{dw} - T_d)$$

6. Constitutive Relations

$h_{bi}=h_f+0.5(Xe_{i-1}+Xe_i)h_{fg}$ (i= 1,2,3; $Xe_0=0$)

$h_{exi}=h_f+Xe_ih_{fg}$ (i= 1,2,3)

$h_f=X_4+K_3P$

$h_{fg}=X_5+K_4P$

$L_{s2}=(L_0-L_{s1})/3$

$T_{sat}=X_1+K_5P$

$V_f = X_2 + K_1 P$

$V_{fg} = X_3 + K_2 P$

$$\rho_b = \frac{1}{V_f + \frac{X_e}{2} V_{fg}}$$

$$\rho_r = \frac{1}{V_f + X_e V_{fg}}$$

$$\rho_g = X_6 + K_6 P$$

$$W_1 = \frac{C_1}{12}[\rho_d (L_{dw} + L_d - L_{s1}) - L_{s2}(\rho_{b1} + \rho_{b2} + \rho_{b3}) - L_r \rho_r]^{0.5}$$

The definitions of the parameters and variables are given below:

A_{fs} = Secondary flow area in the U-tube region

A_{dw} = Effective area of the drum water section

C_l = Effective pressure drop coefficient in the recirculating loop

C_l =Steam valve coefficient

C_m = Specific heat capacity of the metal tubes

$C_{p1\text{-}8}$ = Specific heat capacity of the primary fluid

C_{psub} = Specific heat capacity of the secondary-side water in the sub-cooled region

$h_{b1\text{-}3}$ = Average enthalpy of the nodes in boiling region

h_f, h_{fg} = Saturated and latent enthalpies of water

$h_{ex1\text{-}3}$ = Exit enthalpy of the nodes in boiling region

$K_{1\text{-}6}$ = constants

L = Effective height of U-tubes

L_d = Downcomer length

L_{dw} = Steam generator water level (drum section)

$L_{s1,2}$ = Subcooled and boiling nodal length

$M_{m1\text{-}8}$ = Metal mass in metal nodes

$M_{p1\text{-}8}$ = Water mass in primary nodes

M_{pi} = Water mass in the inlet plenum

P = Steam generator pressure

$P_{r1,2}$ = Inside and outside perimeters of the U-tubes

$S_{ms1\text{-}8}$ = Heat transfer areas from the U-tubes to the secondary side in each node

$S_{pm1\text{-}8}$ = Heat transfer areas from the primary side to the U-tubes in each node

T_d = Downcomer temperature

T_{dw} = Drum water temperature

$T_{m1\text{-}8}$ = Metal tube temperature in each node

$T_{p1\text{-}8}$ = Primary water temperature in each node

T_p = Water temperature in the inlet plenum

T_{po} = Water temperature in the outlet plenum

T_{sat} = Saturated temperature of the water and steam in the UTSG

$U_{pm1\text{-}8}$ = Heat transfer coefficient from the primary side to metal side in each node

$U_{ms1\text{-}8}$ = Heat transfer coefficient from the metal side to secondary side in each node

V_{dr} = Volume of the drum section

V_f, V_g = Specific volume of the saturated water and steam

$V_{fg} = V_g - V_f$

V_r = Volume of the riser region

X_{1-6} = Constants

Xe_{1-3} = Exit quality of the steam leaving the nodes in boiling region

ρ_b = Average density of the water in boiling region

ρ_g = Density of the saturated steam

ρ_r = Density of the water in riser region.

3.3. Results of Simulation for Different Cases of Tube Degradation

Some preliminary results of the simulation of the UTSG model response for the following tube degradation mechanisms are presented:

- Tube plugging by changing the heat transfer area.
- Tube fouling on the primary side (inner tube) by introducing an additional heat transfer resistance at different axial locations.
- Tube fouling on the secondary side (outer tube) by introducing an additional heat transfer resistance at different axial locations.
- Tube metal heat conductivity.

Figures 3.2 through 3.11 show the results of simulation for normal condition and for the cases of tube degradation. The latter include decreased heat transfer area (tube plugging), decreased heat transfer coefficients (fouling) and decreased tube metal conductivity (material property). In all these cases the steam pressure decreased from its nominal value. Figures 3.12 – 3.15 show the process dynamics during normal transients. The

results are indicative of the high fidelity of the model. The simulation results also show that the new model can simulate the fouling problem at different axial locations.

The following observations are made from Figures 3.4 - 3.11:

(1) When we introduce an additional heat transfer resistance so as to decrease by 50% the overall heat transfer coefficient in the metal-to-secondary side sub-cooled heat transfer nodes (MTL1 and MTL8) or the primary-to-metal side sub-cooled heat transfer nodes (PRL1 and PRL8), the steam pressure decreases from 874.91 psia to 868 psia and 868.6 psia respectively.
(2) When we introduce an additional heat transfer resistance so as to decrease by 50% the overall heat transfer coefficient in the metal-to-secondary side boiling heat transfer nodes or the primary-to-metal side boiling heat transfer nodes, the steam pressure decrease from 874.91 psia to about 863.8 psia and 860.1 psia respectively, and there is not much difference in the pressure difference caused by fouling at different axial locations within the boiling region.

These results show that we can differentiate and thus diagnose the fouling in sub-cooled region and the boiling region. However, it seems difficult to diagnose the fouling at different axial locations within a specific heat transfer region.

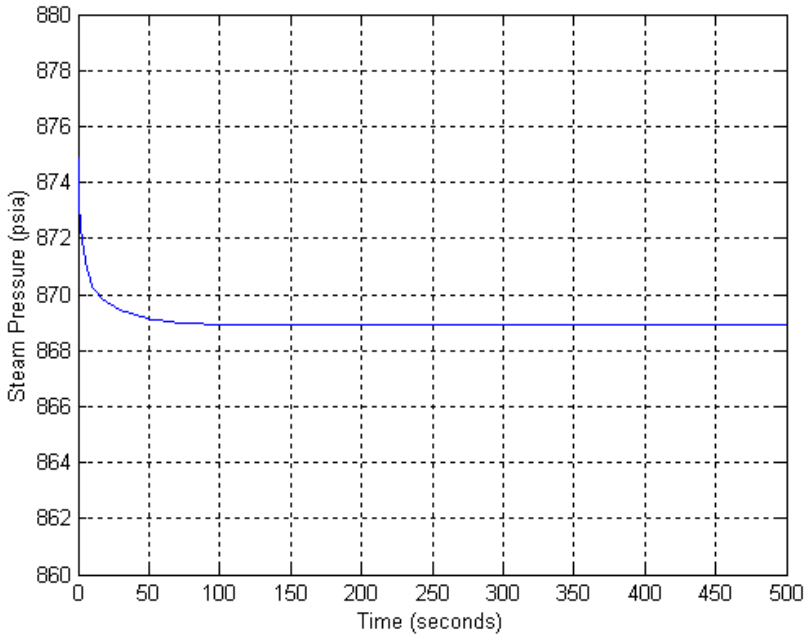

Figure 3.2. Steam pressure change for the case of 5% decrease in the number of tubes.

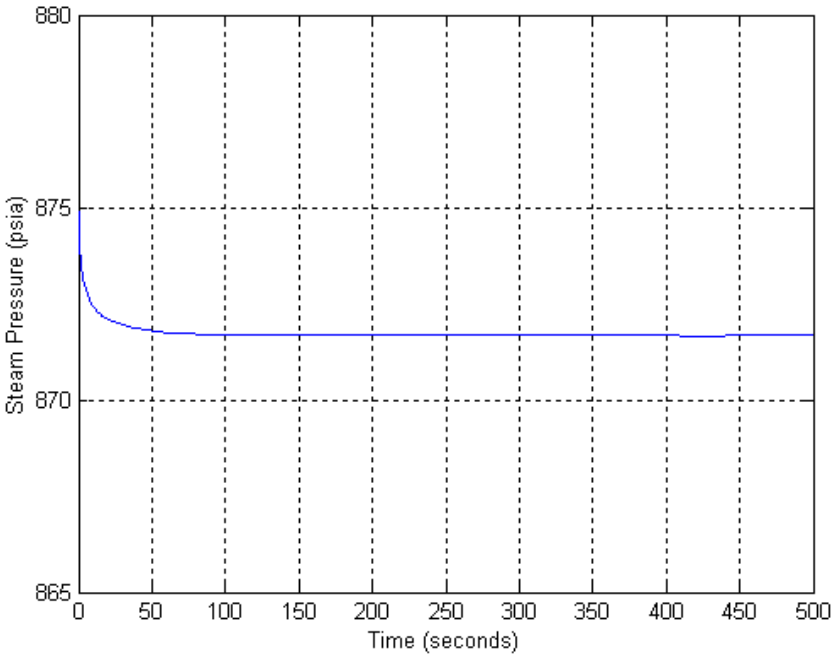

Figure 3.3. Steam pressure change for the case of 10% decrease in the tube metal conductivity.

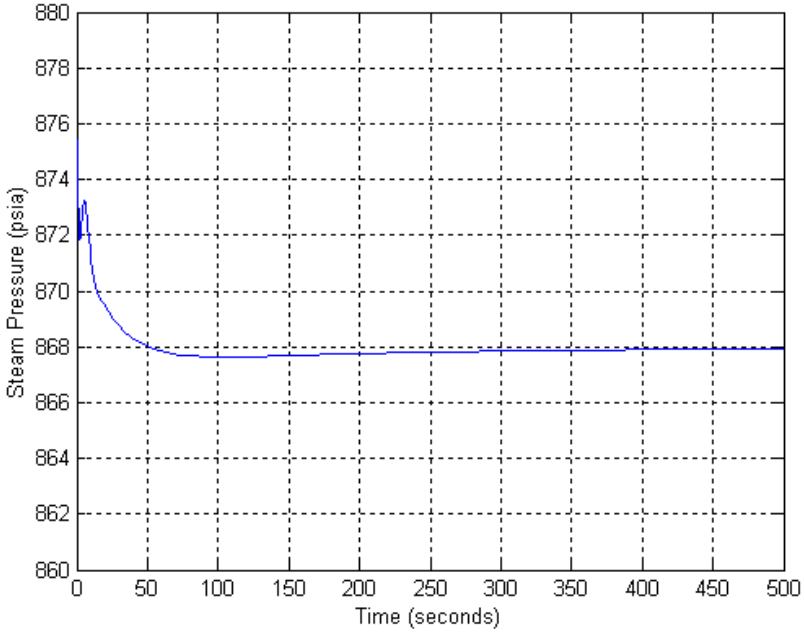

Figure 3.4. Steam pressure change when decreasing by 50% the overall heat transfer coefficient in the metal-to-secondary side sub-cooled heat transfer nodes (MTL1 and MTL8).

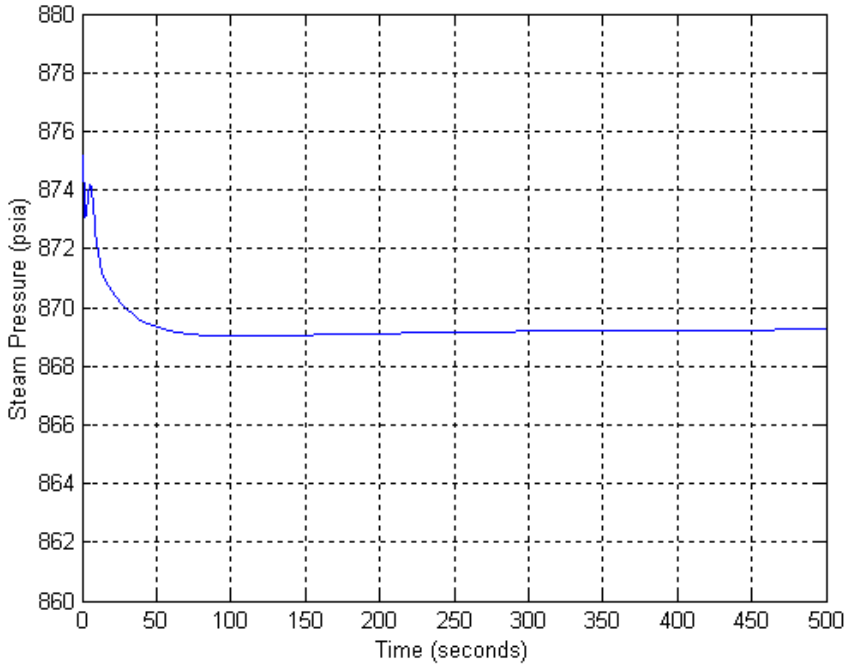

Figure 3.5. Steam pressure change when decreasing by 50% the overall heat transfer coefficient in the primary-to-metal side sub-cooled heat transfer nodes (PRL1 and PRL8).

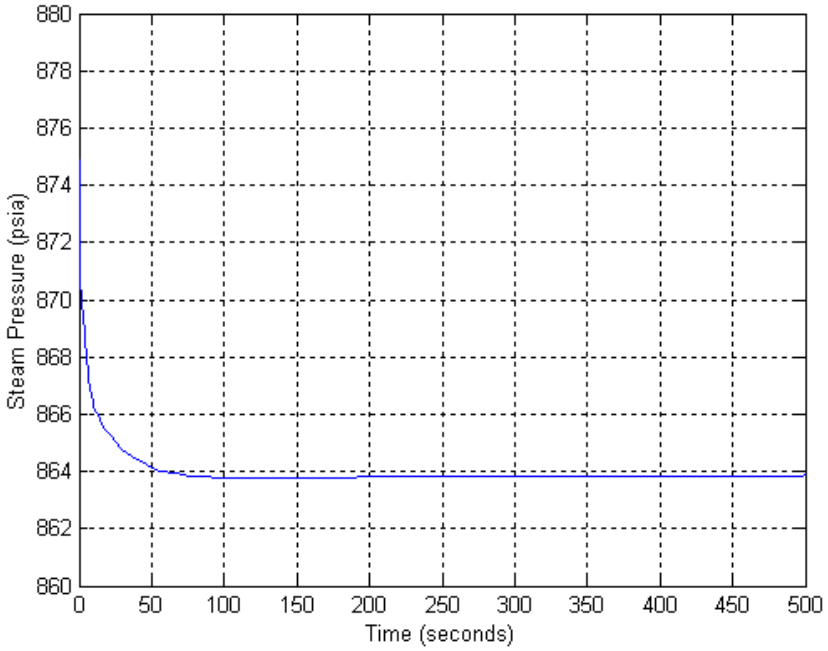

Figure 3.6. Steam pressure change when decreasing by 50% the overall heat transfer coefficient in the metal-to-secondary side boiling heat transfer nodes (MTL2 and MTL7).

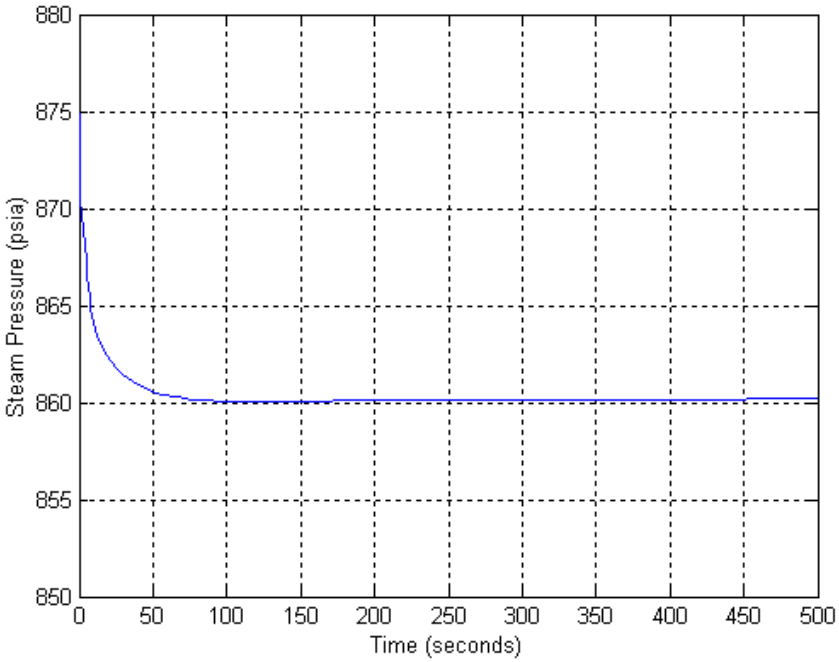

Figure 3.7. Steam pressure change when decreasing by 50% the overall heat transfer coefficient in the primary-to-metal side boiling heat transfer nodes (PRL2 and PRL7).

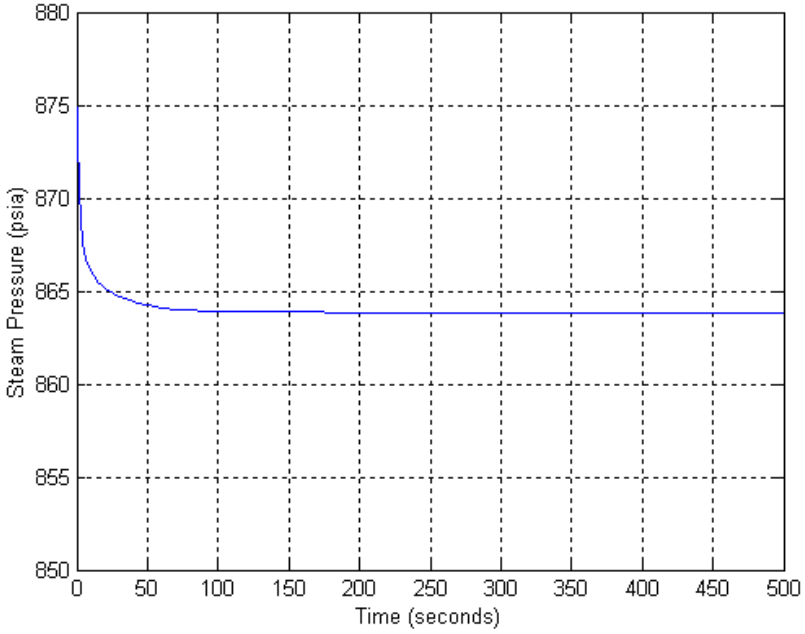

Figure 3.8. Steam pressure change when decreasing by 50% the overall heat transfer coefficient in the metal-to-secondary side boiling heat transfer nodes (MTL3 and MTL6).

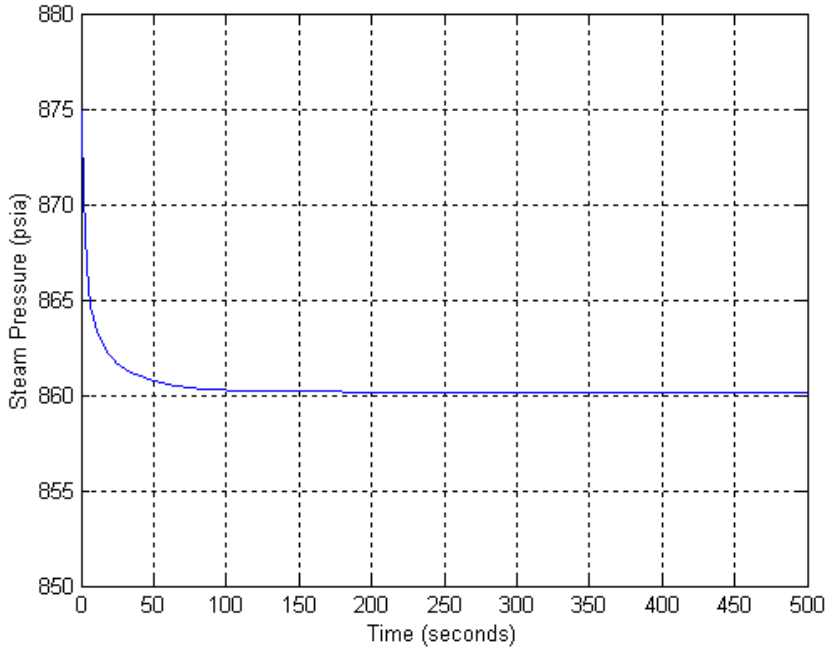

Figure 3.9. Steam pressure change when decreasing by 50% the overall heat transfer coefficient in the primary-to-metal side boiling heat transfer nodes (PRL3 and PRL6).

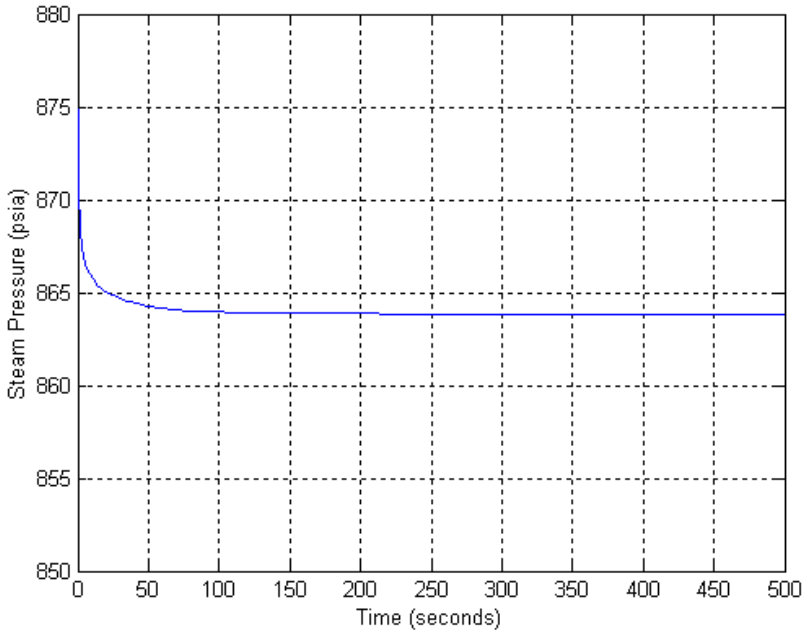

Figure 3.10. Steam pressure change when decreasing by 50% the overall heat transfer coefficient in the metal-to-secondary side boiling heat transfer nodes (MTL4 and MTL5).

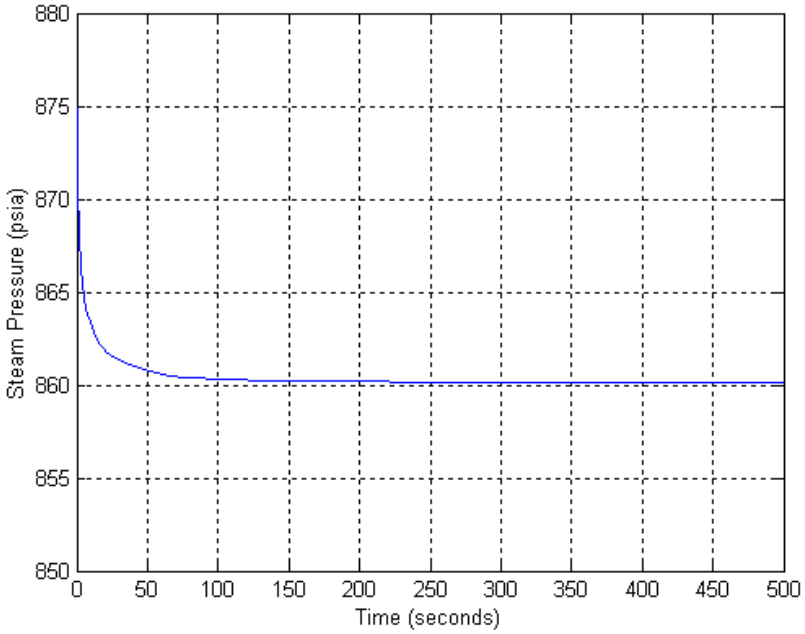

Figure 3.11. Steam pressure change when decreasing by 50% the overall heat transfer coefficient in the primary-to-metal side boiling heat transfer nodes (PRL4 and PRL5).

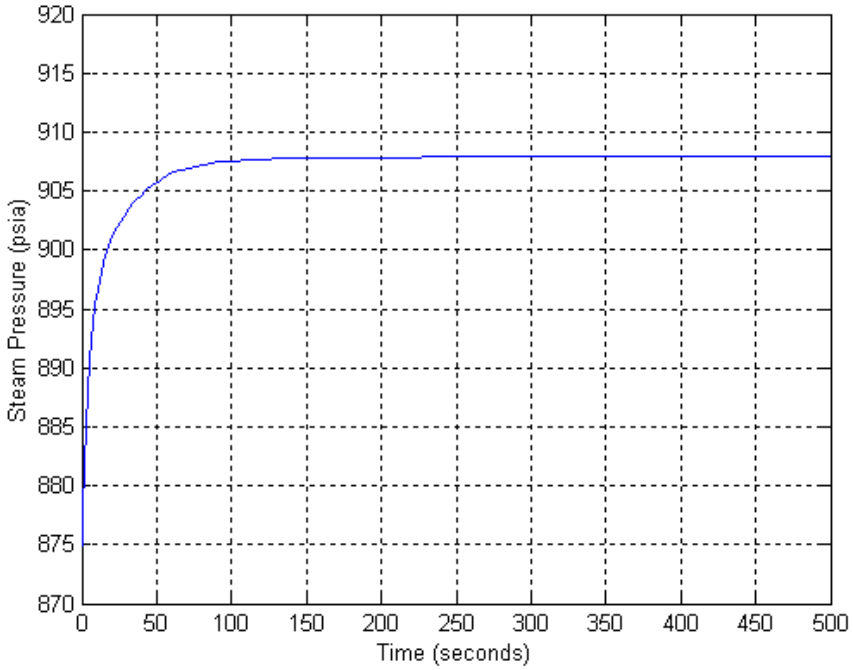

Figure 3.12. Steam pressure variation for a 10% decrease in the steam valve coefficient (decreased steam flow rate).

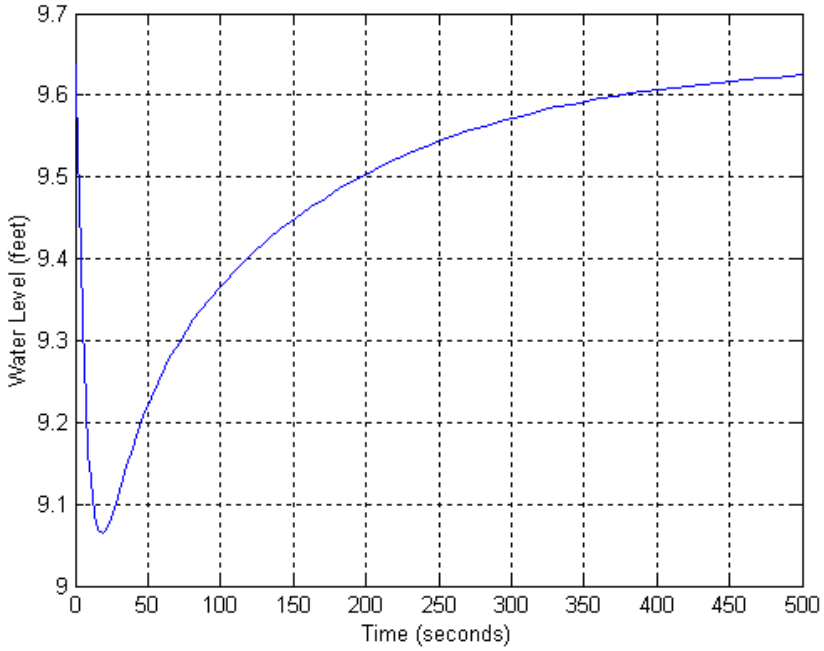

Figure 3.13. SG water level variation for a 10% decrease in the steam valve coefficient.

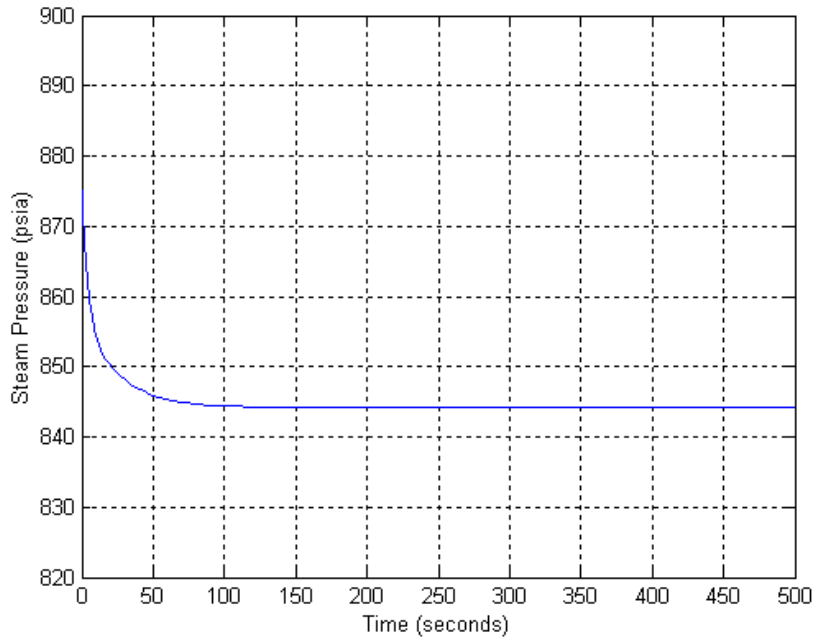

Figure 3.14. Steam pressure variation for a 10% increase in the steam valve coefficient.

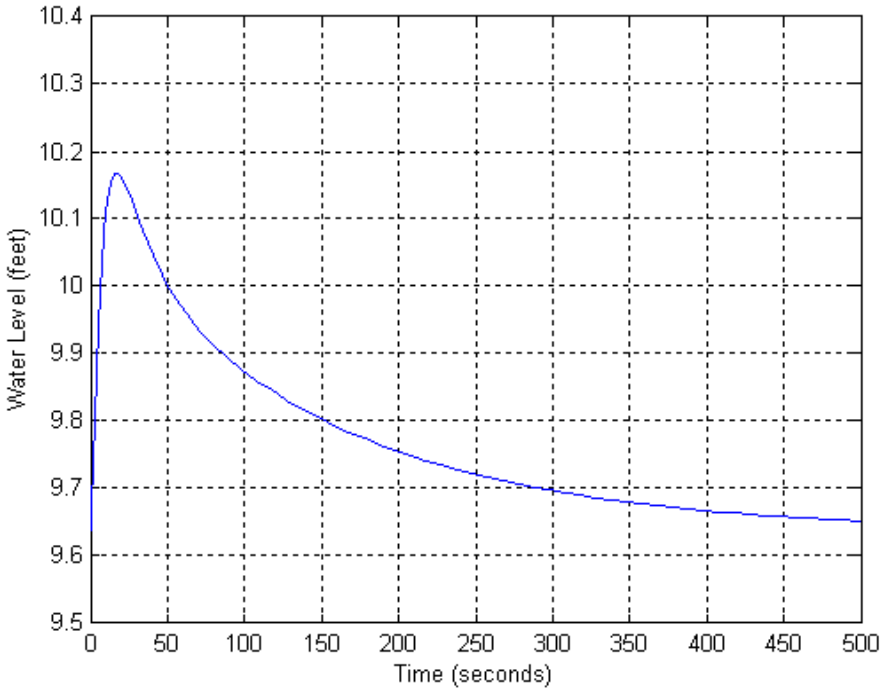

Figure 3.15. Steam generator water level variation for a 10% increase in the steam valve coefficient.

4. EXPERIMENTAL STUDY OF PARTICULATE FOULING IN HEAT EXCHANGERS

4.1. Introduction

In this section, we first present a review of experimental study of particulate fouling by earlier investigators. Our goal of this research on fouling is to study the fouling behavior, verify the particulate fouling model through a laboratory experiment and collect the experimental fouling data for monitoring and diagnosis of fouling. In order to accomplish this task, we adapted a previously developed laboratory setup to perform experimental studies of particulate fouling in a small-scale heat exchanger. In this chapter, we present a literature review of experimental studies of particulate fouling, description of the experimental setup, and the experimental results.

4.2. Review of Experimental Study of Particulate Fouling in Heat Exchangers

Over the years, several researchers performed experiments to study the particulate fouling in heat exchangers. Some representative work from the literature is reviewed.

Melo et al. (1988) studied particle transport in fouling on copper tubes. They used the material KAOLIN to simulate suspended particles in water. Their fouling tests were performed in an annular heat exchanger consisting of a 2-meter long external Perspex tube and a removable inner copper tube, which was electrically heated. Water-KAOLIN suspensions were circulated through the annular section at different Reynolds numbers. KAOLIN particles were studied with a laser flow granulometer and a scanning electron microscope (SEM) and the fouling layer was roughly characterized as a thin disc with 16 μm (mean diameter) by 1 μm (mean thickness). SEM visualization of the deposits formed on the copper tube surfaces showed that the particles adhere by their larger faces

(the bases of the disc). The thermal conductivity, density, final thickness, mass, and thermal resistance were measured or estimated. The experimental results show that the fouling data fit well into the asymptotical behavior and mass transfer controls the deposition rate when Re < 3900, and the adhesion dominates the process at higher Re values.

Middis et al. (1990) performed experimental study on particulate fouling in heat exchangers with enhanced surfaces. In their study, KAOLIN particles in X-2 were chosen as the fouling suspension. They studied the particulate fouling in a plate heat exchanger and a double pipe heat exchanger over a wide range of flow conditions. The fouling experimental results again show that the fouling progression follows a characteristic asymptotic behavior. They also studied the effect of Reynolds number and other factors on fouling behavior, and the conclusions are similar to those reached by Melo et al.

Charmra et al. (1993) made a study on the effect of particle size and size distribution on particulate fouling in tubes. In their study, the Wieland NW, Wolverine Korodense, and a plain tube were chosen for testing. Two types of foulants, clay and silt, were used in the tests. The fouling tests were conducted for different concentrations, flow rate, foulant type, and particle diameter. Their experimental results show that the enhanced tubes exhibit higher fouling resistance than the plain tubes; the enhanced and the plain tubes exhibit the same fouling behavior, and the fouling resistance decreases as the concentration decreases for all particle sizes. This is because the deposition rate decreases as the concentration decreases since the deposition rate is proportional to fouling concentration. In addition, as the particle size (diameter) increases, the asymptotic fouling resistance decreases. This is because the particle deposition rate is proportional to $Sc^{-0.57}$, where the Schmidt number Sc is defined as the ratio of the

kinematic viscosity over the Brownian diffusivity. Hence smaller particles will have smaller Schmidt numbers and should undergo higher deposition rates (fouling resistances) than larger particles. The experiments also show that the asymptotic fouling resistance, R_f^*, as a function of Reynolds number for the Korodense tube, decreases as the Reynolds number increases. This is because the removal rate is directly proportional to the wall shear stress. Therefore, as the Reynolds number increases, the wall shear stress increases, which in turn increases the removal rate, and as a result the fouling resistance decreases. Again, the results also show that the fouling resistance decreases as the particle diameter increases. It is also shown that the fouling resistance increases as the particle size decreases. For example in their results, the asymptotic fouling resistance for the 16 μm particles is significantly smaller than that for the 4 μm particles except for the plain tube. This is due to the transition from the diffusion dominant regime to the inertia dominant regime. It is also found that the enhanced tubes (NW and Korodense tubes) have higher asymptotic fouling resistances than the plain tube.

Other researchers who used other types of material to simulate the fouling particles. Among them, Muller-Steinhagen et al. (1988) used Al_2O_3 particles to study particulate fouling in heat exchangers. Basset et al (2000) used the sol-gel method, proposed by Sugimoto et al. (1980), to synthesize the simulated magnetite particles to study the fouling of Alloy-800 heat exchanger surfaces by magnetite particles, etc. Turakhia et al. (1984) studied measurement and diagnosis of the fouling of heat exchanger surface using the pressure drop method and the overall heat transfer resistance method.

It should be noted that most of the above researchers only used a single tube or even a tube section in their experimental study. Hence it is necessary to use a real heat exchanger to study the particulate fouling behavior.

4.3. Research Experimental Setup for Particulate Fouling Tests

As mentioned above, we wanted to use a real heat exchanger and perform experiments to study the particulate fouling behavior. For this purpose we designed and adapted an experimental setup. Figure 4.1 shows the schematic of this setup, and Figure 4.2 shows a photograph. In our experiment, we used KAOLIN clay suspended in water and a small-scale tube-and-shell heat exchanger. The particulate material is the RC-90 KAOLIN from Thiele KAOLIN Company. The particle size is $< 2\ \mu m$ with a percentage of 98.0% and a pH (dry clay tested at 20% solids) of 6.8. The heat exchanger, HT-1-A-CI-2-24, was procured from Mahan's Thermal Products, Inc. It has 31 copper tubes, with shell diameter $2\frac{1}{8}$ inch, tube length 24 inch, and tube outer diameter $1/4$ inch.

As seen in Figures 4.1 and 4.2, the experimental setup consists of a stainless steel water tank, a 2 KW electrical heater, a stainless steel centrifugal pump, a shell-and-tube heat exchanger, two flow-meters measuring the tube-side and shell-side flow rates, four thermocouples measuring the inlet and outlet temperatures of the tube-side and shell-side coolant, and a data acquisition system. The data acquisition system includes two conditioning modules, a connection box, a data acquisition board, and a personal computer. A LabVIEW data acquisition software is used to collect, display, and store

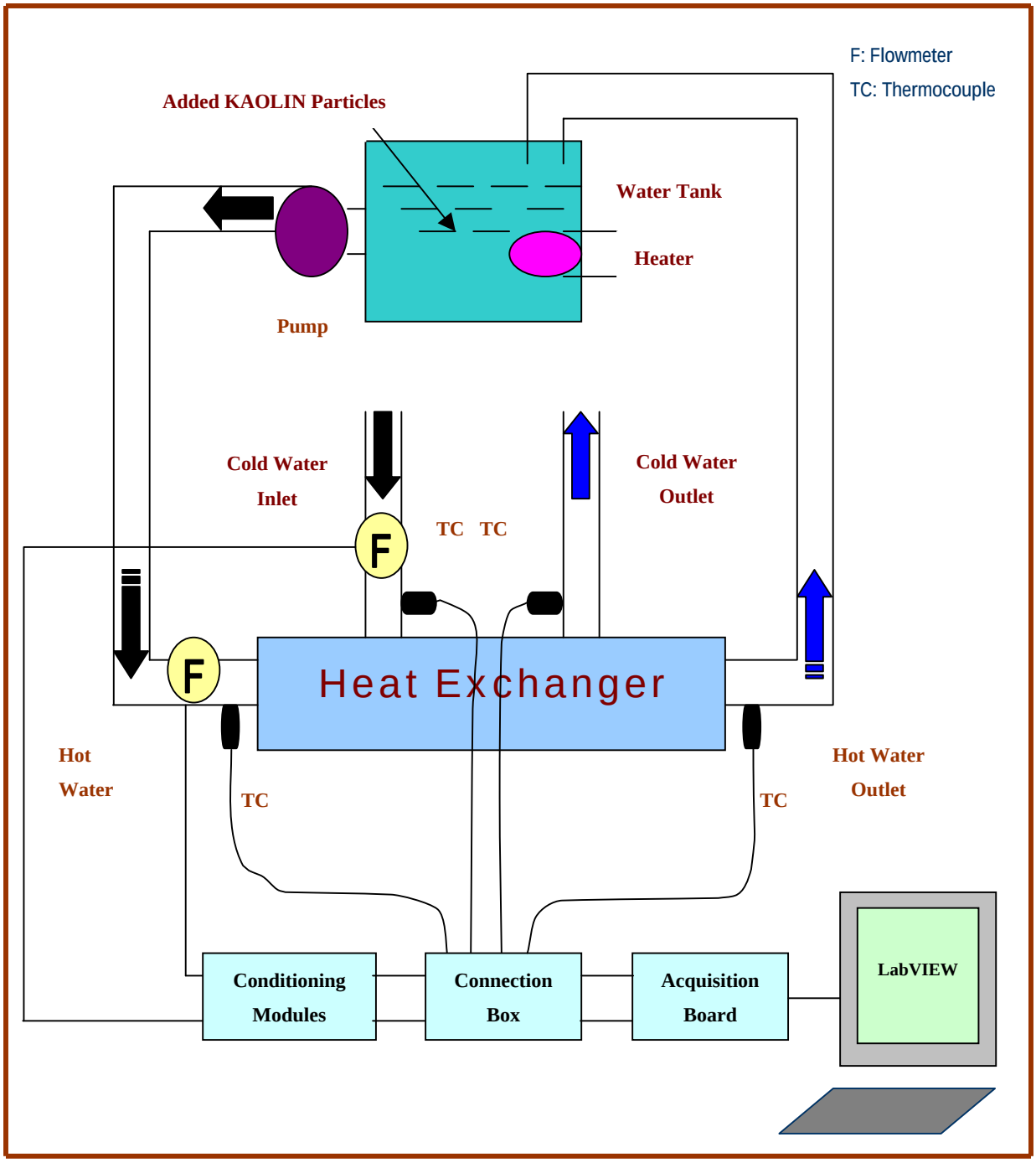

Figure 4.1. Configuration of the heat exchanger experimental set-up for particulate fouling tests.

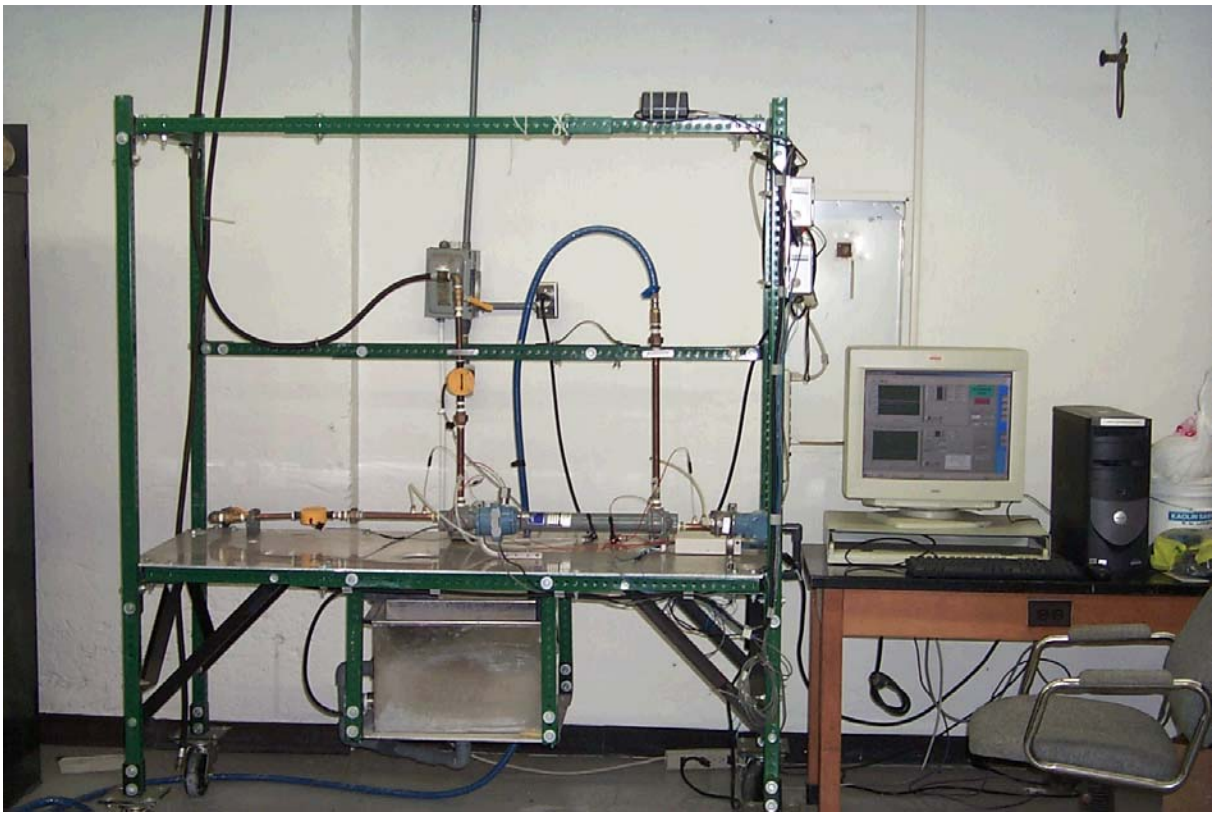

Figure 4.2. An Overview of the Experimental Setup

the experimental data. Water, mixed with KAOLIN particles, is designed to flow through the tube side of the heat exchanger so that it is convenient to remove or wash off the fouling layer after the experiment is completed. Figure 5.2 shows the heat exchanger on the mobile table, water tank (underneath the table), connections to hot and cold water lines, and the data acquisition computer system.

4.4. Calculation of Overall Thermal Resistance and Experimental Results

The effect of the fouling progression can be monitored by continuously evaluating the overall heat transfer thermal resistance (1/UA). From energy balance, we have

$$\dot{Q} = UA\Delta T_{LMTD} = \dot{m}_h C_h \Delta T_h = \dot{m}_c C_c \Delta T_c \tag{4.1}$$

Where, $\dot{Q}$ is the heat transfer rate;

A is the surface area on which the overall heat transfer coefficient U is based;

ΔT_{LMTD} is the logarithmic mean temperature difference for the heat exchanger and is defined as:

$$\Delta T_{LMTD} = \frac{\Delta t_1 - \Delta t_2}{\ln(\Delta t_1 / \Delta t_2)} \tag{4.2}$$

For parallel or concurrent flow heat exchangers:

$$\Delta t_1 = t_{h,in} - t_{c,in}\ ;\ \Delta t_2 = t_{h,out} - t_{c,out}\ . \tag{4.3}$$

For counter flow heat exchangers:

$$\Delta t_1 = t_{h,in} - t_{c,out}\ ;\ \Delta t_2 = t_{h,out} - t_{c,in}\ . \tag{4.4}$$

As stated above, U is the overall heat transfer coefficient, and A is the heat transfer area, which may slightly change with fouling progress. However, the product UA can be calculated and be thought of as inseparable in terms of the effect of fouling on heat transfer. The inverse of UA is the overall thermal resistance, which increases as the fouling deposition increases.

From Equation (4.1), we can derive the following formula for calculating the overall thermal resistance:

$$\frac{1}{UA} = \frac{\Delta T_{LMTD}}{\dot{m}_h C_h \Delta T_h} = \frac{\Delta T_{LMTD}}{\dot{m}_c C_c \Delta T_c} \tag{4.5}$$

This overall thermal resistance, *1/(UA),* is continuously computed so as to monitor the particulate fouling behavior in the heat exchanger. To determine the overall

thermal resistance, we measure the mass flow rate of the cold side or/and the hot side, inlet and outlet temperatures of both the cold side and the hot side, as shown in Figures 4.1 and 4.2. In our calculation of overall thermal resistance, we used the cold-side flow rate and the inlet and outlet temperatures. It should also be noted that in our experimental design, we have used the parallel flow pattern in the heat exchanger.

In our experiment, initially 70gm KAOLIN particles were added to the water tank then at about 50 hours after the start of the experiment, another 50 gm were added to the tank, which has a dimension of 18" × 12" × 12". This resulted in a fairly high concentration of about 2823 ppm.

The experiment was run for about 170 hours. A MATLAB code was used to process the experimental data and to calculate the overall thermal resistance. The code is given in the Appendix. Figure 4.3 shows the raw signals that were measured and collected during the experiment. Figure 4.4 presents the experimental results of the changes in the overall thermal resistance with time. During the entire experiment, the coolant flows of both the tube-side and the shell-side were basically kept constant.

It should also be noted that since there was background noise present in the measurements, we used a MATLAB function to filter the computed overall fouling resistance. Thus, it looks "smoother" as shown in Figure 4.4. From Figure 4.4, we see that the overall fouling resistance first increases with time, then at after about 120 hours of running it tends to attain a steady state value. This proves that the overall thermal resistance exhibits an asymptotic behavior even in a real small-scale heat exchanger.

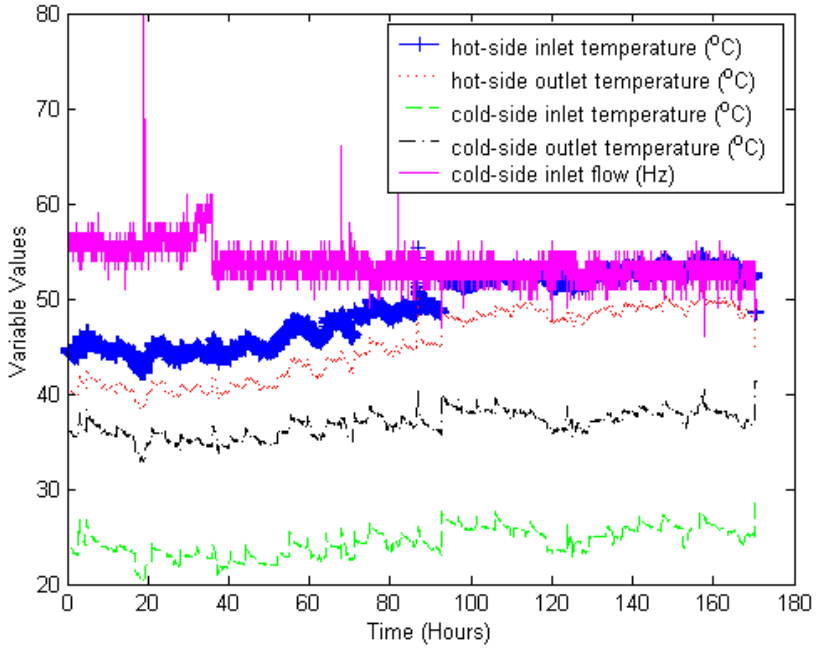

Figure 4.3. Experimental results - measured raw signals from the experiment.

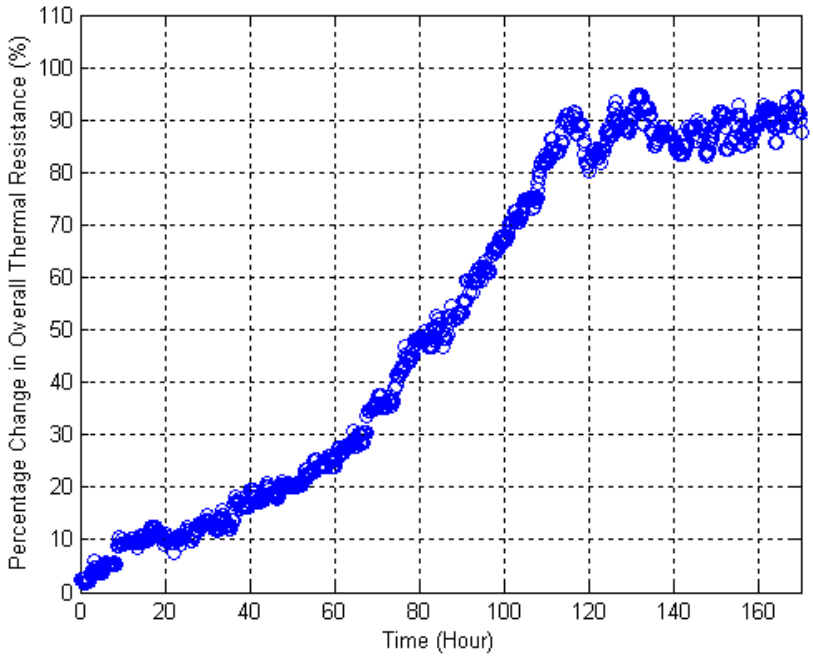

Figure 4.4. Experimental results - overall thermal resistance variation vs. experimental running time.

4.5. Overall Thermal Resistance after Removal of the Fouling Deposition Layer

After the experiment was completed, we opened the heat exchanger and used brushes to remove and wash off the fouling layers that attached to the inner surfaces of all the 31 heat exchanger tubes. Then we ran the experiment again for a while and used the same method as above to monitor or track the change in overall thermal resistance of the heat exchanger. The results are shown in Figures 4.5 and 4.6. It should be noted that Figure 4.6 is just a local zoom of Figure 4.5. The objective is to show more clearly the change in the overall thermal resistance of the heat exchanger. From these two figures, we can clearly see that the overall thermal resistance of the heat exchanger after cleaning restores to the overall thermal resistance value of the previous clean state. This confirms that the change in overall thermal resistance of the heat exchanger that we observed during the experiment was really due to the fouling progression. This also indicates that we can successfully monitor the fouling progression in a heat exchanger by tracking the changes in the overall thermal resistance.

4.6. Remarks

From the above experimental study on particulate fouling and its time progression in a small-scale heat exchanger, we make the following observations.

- The particulate fouling in a small-scale heat exchanger still exhibits an asymptotic behavior. This agrees with the conclusion from theoretical studies. It should be noted that in Figure 5.3, the overall thermal resistance does not seem to follow a strict exponential trend. This is most likely due to our change (increase) in the fouling particle concentration at about 50 hours after the start of the experiment.

- All the above results show that the experimental methodology and design of the setup for particulate fouling study are correct and successful. It has been demonstrated that the particulate fouling in a heat exchanger can be monitored and diagnosed by tracking the change in the overall thermal resistance.

- The acquired experimental data are useful and can be used for the monitoring and diagnosis of fouling in the heat exchanger using the GMDH modeling technique. This is discussed in detail in Section 5.

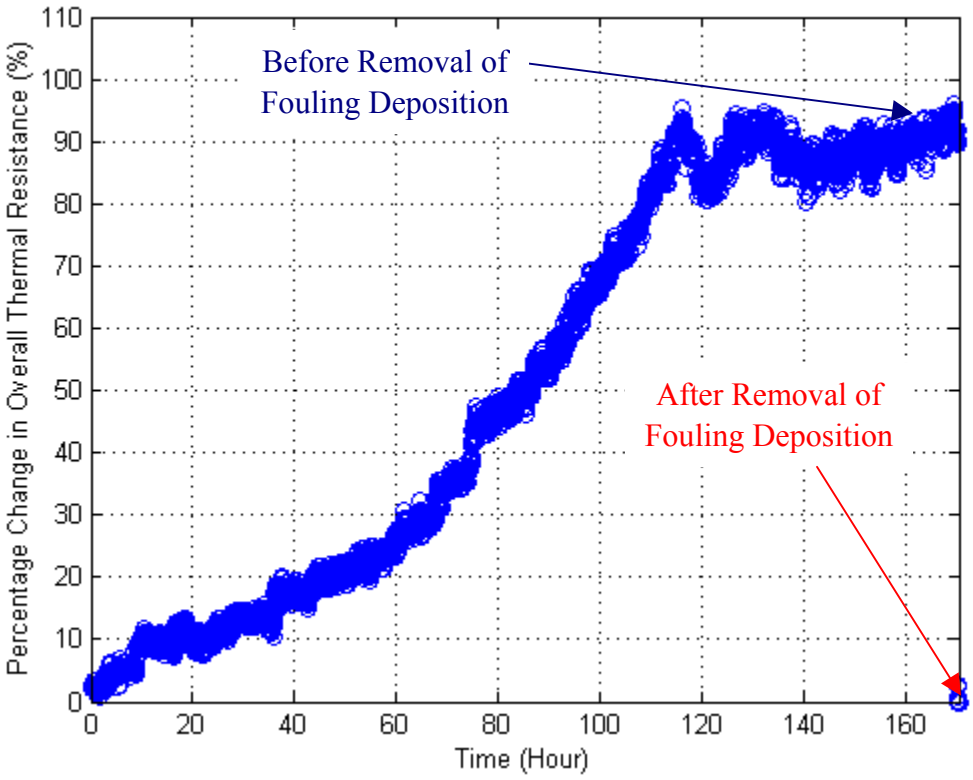

Figure 4.5. Change in the overall thermal resistance of the heat exchanger before and after removal of the fouling deposition layers.

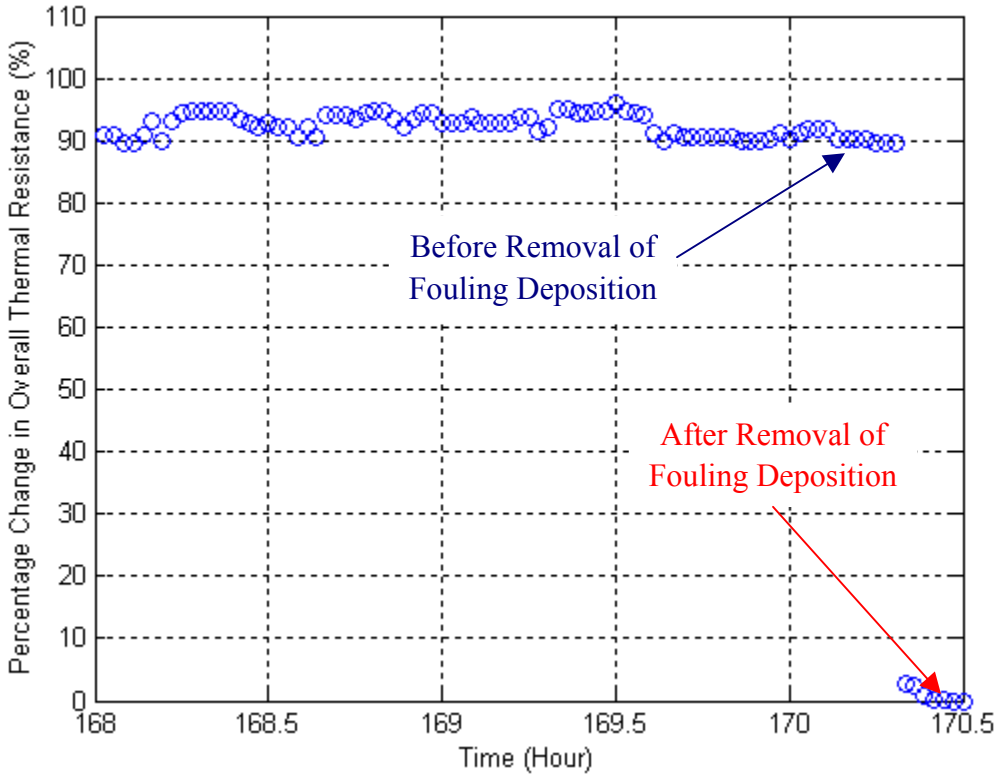

Figure 4.6. Change in overall thermal resistance of the heat exchanger before and after removal of the fouling deposition layers. This is a local zoom of Figure 4.5.

5. MONITORING AND DIAGNOSIS OF FOULING USING THE EMPIRICAL DATA-BASED MODELING APPROACH

5.1. Introduction

The Group Method of Data Handling (GMDH) approach has found wide applications in various areas, such as data mining, forecasting, prediction and system modeling, pattern recognition, and fault detection and isolation (FDI). GMDH is an inductive self-organizing algebraic model since we do not need to know the exact physical model in advance. Instead, GMDH automatically learns the relations that dominate the system variables during the training process. Therefore a good GMDH model can be used to avoid the need for the development of a first-principle model, especially when this model is costly or even impossible to develop for a very complex system. After a reliable GMDH model is developed, it can be then used for FDI or many other purposes as mentioned above.

In later sections of this chapter, we first present a brief introduction to the GMDH approach, then we use the GMDH method and the MATLAB functions previously developed by Ferreira and Upadhyaya (1998) to monitor and diagnose the fouling problems occurring in both a heat exchanger and a steam generator.

5.2. The GMDH Method

GMDH is a data-driven modeling technique, which uses mathematical functions to characterize the complex nonlinear relationships that are inherent among the given input-output mapping. It uses the following so-called Kolmogorov-Gabor polynomial form to approximate the input-output mapping:

$$y = a_0 + \sum_{i=1}^{n} a_i x_i + \sum_{i=1}^{n}\sum_{j=1}^{n} a_{ij} x_i x_j + \sum_{i=1}^{n}\sum_{j=1}^{n}\sum_{k=1}^{n} a_{ijk} x_i x_j x_k + \ldots \qquad (5.1)$$

Where, $\{x_1, x_2, \ldots, x_n\}$ is the input variable vector,

y is the output variable,

$\{a_0, a_i, a_{ij}, ...\}$ is the vector of coefficients or weights.

Additional input variables may also be formed from the basic measurements, and may include nonlinear and rational functions of these measurements.

A polynomial network of GMDH structure with m inputs and k layers is shown in Figure 5.1. The main procedure for GMDH algorithm implementation used for a given set of n observations of m independent variables is described as follows:

Step 1:

Subdivide the data into training data set and testing data set and preprocess the data sets by normalizing them.

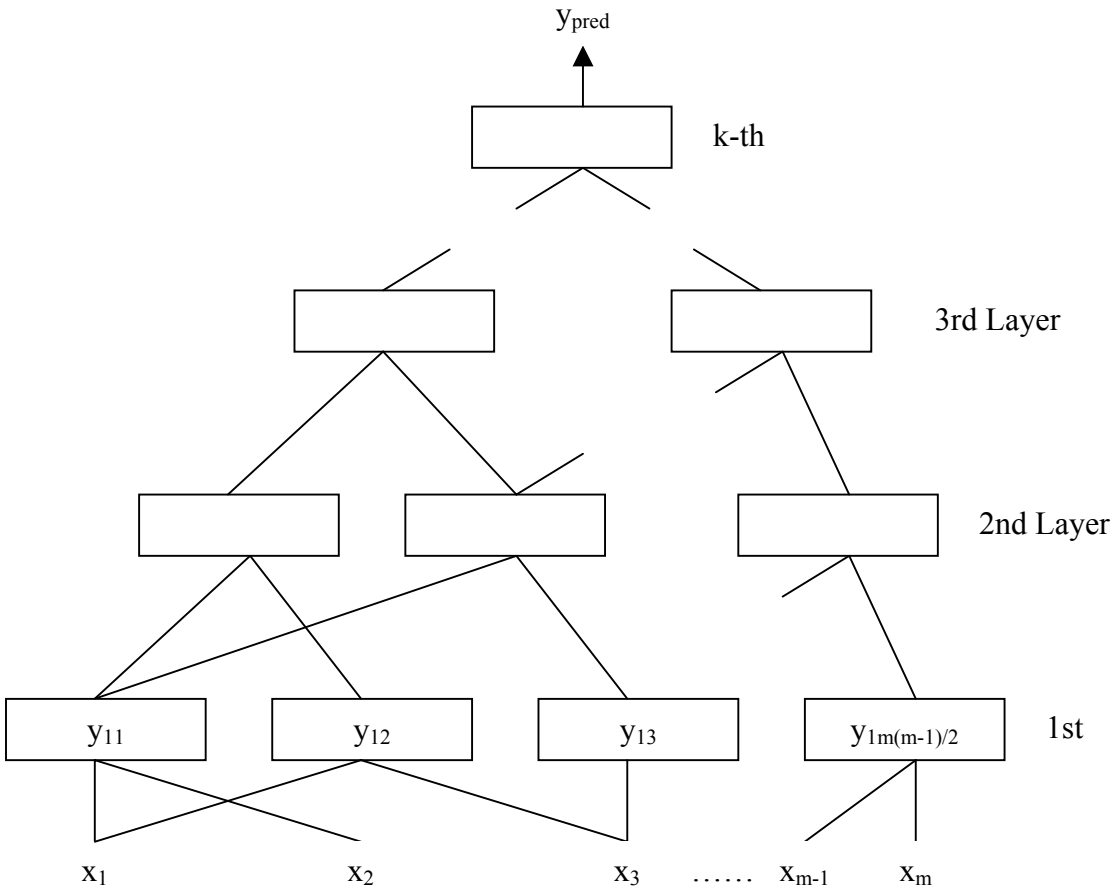

Figure 5.1. The GMDH network structure.

Step 2:

For each pair of input variables x_i and x_j and associated output y of the training data set, calculate the regression polynomial

$$y = A + Bx_i + Cx_j + Dx_i^2 + Ex_j^2 + Fx_i x_j \qquad (5.2)$$

that best fits the dependent observations y_i in the training set. A total number of $m(m+1)/2$ regression polynomials will be computed from the observations.

Step 3:

For each regression, evaluate the polynomial for all n observations and store these n new observations in a new matrix Z. That is, recalculate current layer's output using all data sets with the parameters generated in step 2, and store these outputs in a new matrix Z as the new input terms for the next layer of the GMDH architecture.

Step 4:

Screening out the least effective variables: First, for each column of the matrix Z, the root mean square error is computed and is given by:

$$r_j^2 = \frac{\sum_{i=1}^{n} \left(y_i - z_{ij}\right)^2}{\sum_{i-1}^{n} y_i^2} \qquad (5.3)$$

Then order the columns of Z according to increasing r_j, and pick those columns of Z that satisfy $r_j < R$ to replace the original columns of X. Here, a cut-off value 'R' needs to be chosen by the user. This means that all the columns of Z satisfying $r_j < R$ are picked to replace the input terms in the previous layer, while all the variables with $r_j > R$ are screened out and are not passed to the next generation of the algorithm.

Step 5:

Testing for optimality: The above procedure is repeated until over-fitting starts to occur, which can be checked by cross validation, that is, by plotting the smallest of the r_j's calculated in

each generation and comparing it with the smallest r_j's of the previous generation. The process should be stopped when the r_j's begin to increase.

At the completion of GMDH algorithm, all quadratic regression polynomials are stored, and the estimated coefficients for high order polynomial are determined through back tracing the GMDH architecture until the original variables (x_1, x_2, …, x_n) is reached. Then we can use this GMDH model to make new predictions of y. Further details of the GMDH algorithm and its implementation are given by Ferreira and Upadhyaya (1998), Lu (2001), Ivakhnenko (1995), and Kondo (2003). In the following sub-sections, we use the MATLAB functions GMDH_PBK, ANNt_PBK, etc., developed by Ferreira and Upadhyaya (1998), to monitor fouling degradation in both HX and UTSG systems.

5.3. Data Generation

In order to monitor and diagnose degradations including fouling in a heat exchanger or UTSG, it is first necessary to generate data for the development of good data-driven models. In order to generate data, an appropriately developed first-principle model is essential.

In our study, for the heat exchanger, we use the energy (heat) balance equations, as defined by Equations (5.1) - (5.3) for the case of parallel flow, to generate the normal data. The MATLAB code is given in Appendix E. The experimental data, characterizing the progress of fouling in a heat exchanger, were collected from the experimental setup and is used for monitoring and diagnosis of fouling in the heat exchanger using GMDH method. When generating normal data for HX, the coolant flow on both the tube-side and the shell-side were kept constant as was the case during the experiment, and only the inlet temperatures of both sides were chosen as the forcing (input) variables.

For the UTSG, a good physics model was developed in Phase II [200]. We used this SIMULINK model to generate both normal data and the data with the presence of fouling, which is assumed to progress with time as given in Figures 4.1 and 4.2. These data were used for monitoring and diagnosis of fouling in a steam generator using the GMDH method. When generating the normal data, both the tube-side inlet temperature and the number of heat transfer

tubes were chosen as forcing variables; and an additional fouling thermal resistance was added when generating data for fouling.

It should be noted that when generating the data, all the input forcing variables should cover the entire desired space. Otherwise, a good data-driven model cannot be properly developed.

5.4. Monitoring and Diagnosis of Fouling in the Heat Exchanger

Now that both the normal data and data with fouling are available, we first use the GMDH method to develop a data-driven model and then use the model to monitor and diagnose the fouling progress. The MATLAB code for monitoring and diagnosis of fouling in the heat exchanger is given in the Appendix.

The procedure is first to establish a data-driven model using the normal data, then use this model and the faulty data, i.e. the experimental data characterizing the fouling progress, to make predictions and estimate residual of the outlet temperatures of both the tube-side and the shell-side. Figure 5.2 gives the hot-side or the tube-side outlet temperature data used for training and the GMDH predicted values; Figure 5.3 presents the hot-side or the tube-side outlet temperature data used for testing and the GMDH predicted values. We see from these two figures that they both agree with each other very well.

After development of the GMDH model, we use the experimental data and the model to make new predictions. Figure 5.4 gives the GMDH predictions of the hot-side outlet temperature of the heat exchanger versus the real experimental data of the same variable. Figure 5.5 presents the estimate residual. From Figures 5.4 and 5.5, we can see that at the initial stage of the experiment, the predicted value and the measurements are almost equal to each other because there is little fouling at the early stage. Then as the fouling progress and gradually increases, the residual also increases. Finally, when the fouling reaches the asymptotical value and keeps basically constant, the residual also follows the same trend, coming to a steady-state value. Comparing Figure 5.5 with Figure 4.9, it is interesting to note that the GMDH estimation of residuals follow the same behavior as the overall thermal resistance as a function of experimental running time.

Figure 5.6 gives the cold-side or the shell-side outlet temperature used for training and the GMDH predicted values; Figure 5.7 presents the cold-side outlet temperature used for testing and the GMDH predicted values. Also we can see from these two figures that they both agree with each other very well.

Then we use the experimental data and the developed GMDH model to make new predictions. Figure 5.8 gives the GMDH predictions of the cold-side outlet temperature of the heat exchanger versus the real experimental data of the same variable. Figure 5.9 shows the residuals. Again from Figures 5.8 and 5.9, we can see that at the initial stages of the experiment, the predicted values and the measurements agree very well with each other because there is very little fouling at the early stage. Then as the fouling progresses and gradually increases, the residual also increases. Finally the fouling reaches an asymptotical value and keeps almost constant, the residual also follows the same tendency and finally attains a steady state.

Comparing Figure 5.5 with Figure 5.9, again we find that the GMDH estimation residual follows the same behavior as the overall thermal resistance as a function of experimental running time. These results suggest that we can easily use the residual trending given in Figures 5.4-5.5 and Figures 5.8-5.9 to monitor and diagnose the fouling problem that is occurring in a heat exchanger.

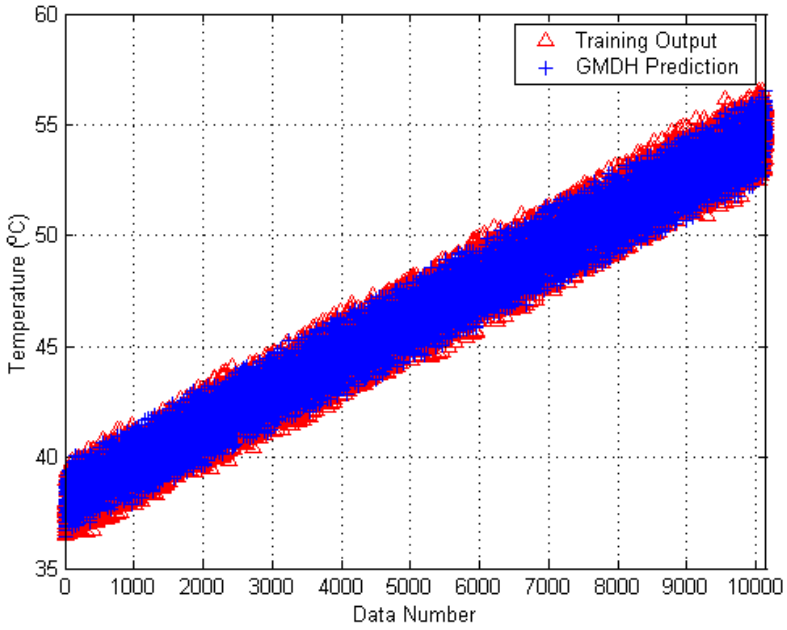

Figure 5.2. Training output and the GMDH predicted values of the tube-side/hot-side outlet temperature.

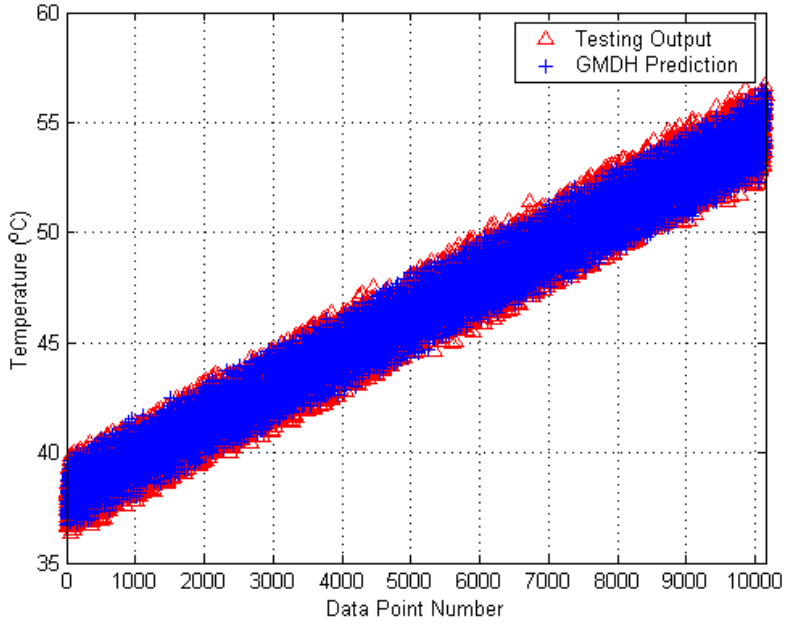

Figure 5.3. Testing output and the GMDH predicted values of the tube-side/hot-side outlet temperature.

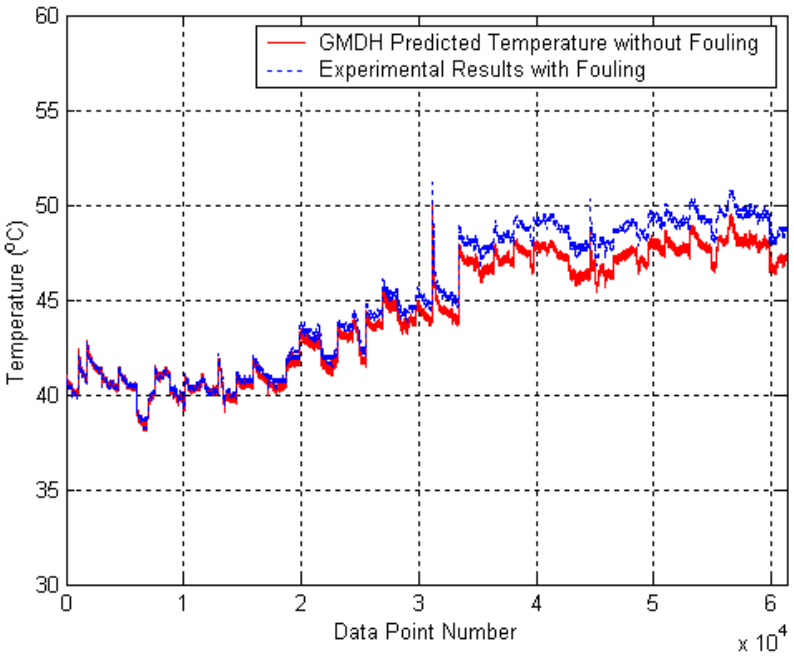

Figure 5.4. GMDH predictions of the hot-side outlet temperatures of the heat exchanger versus the real experimental data.

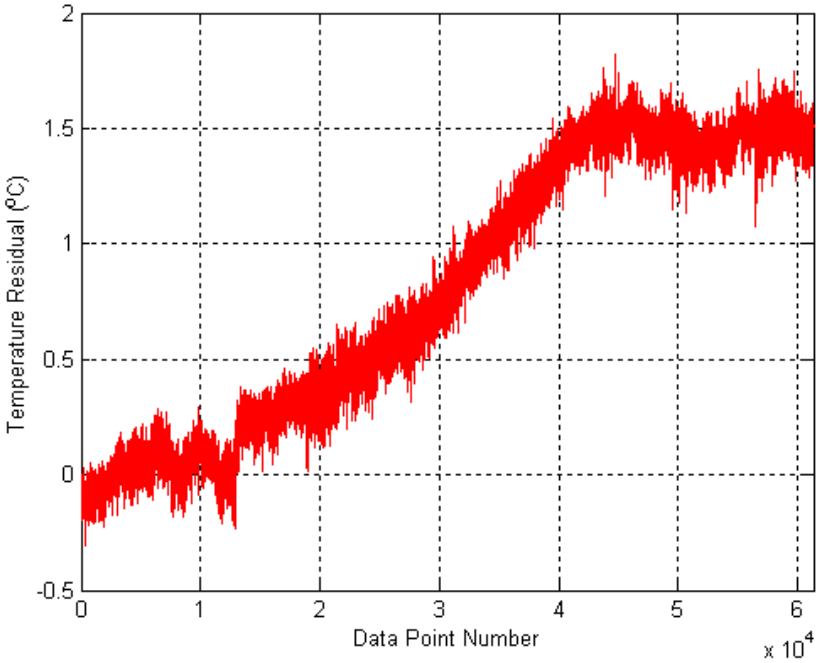

Figure 5.5. Residual between the GMDH predictions of the hot-side outlet temperatures of the heat exchanger and the real experimental data.

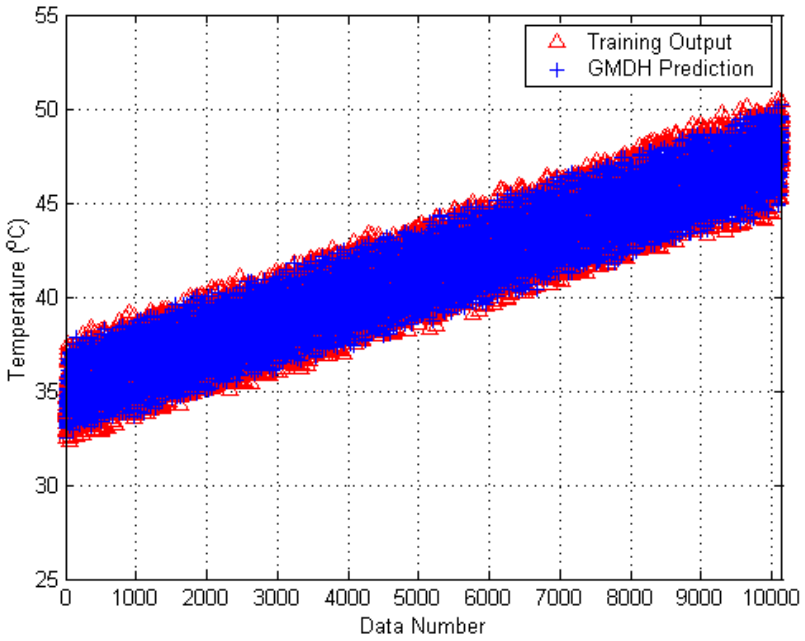

Figure 5.6. Training output and the GMDH predicted values of the shell-side/cold-side outlet temperature.

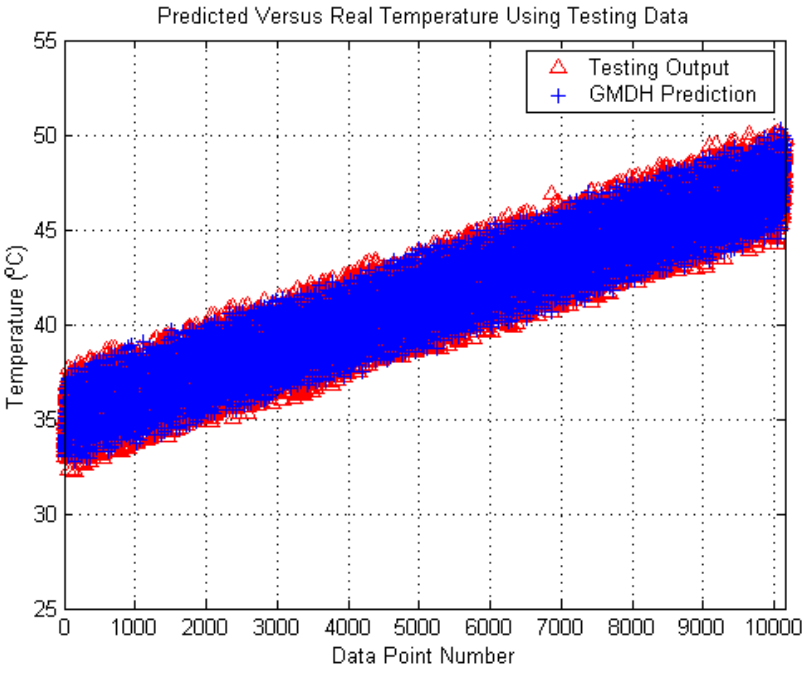

Figure 5.7. Training output and the GMDH predicted values of the shell-side/cold-side outlet temperature.

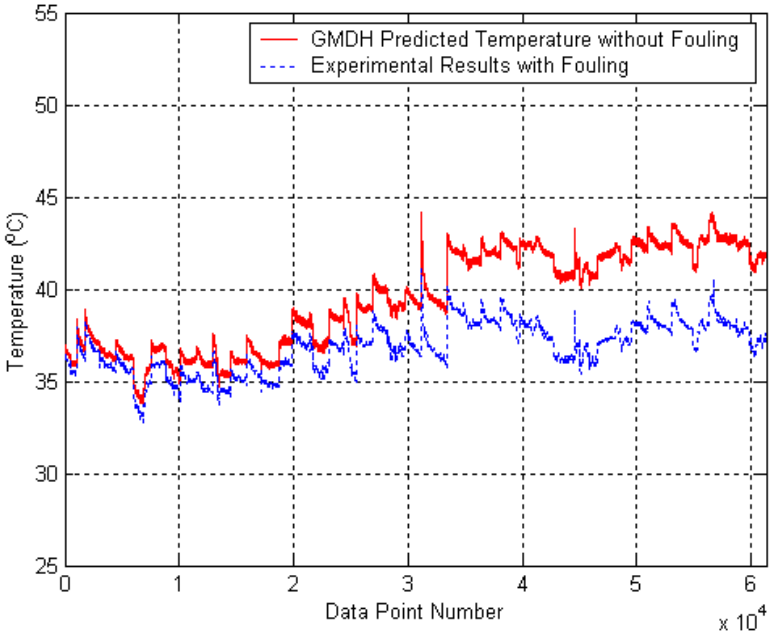

Figure 5.8. GMDH Predictions of the cold-side Outlet temperatures of the heat exchanger versus the real experimental data.

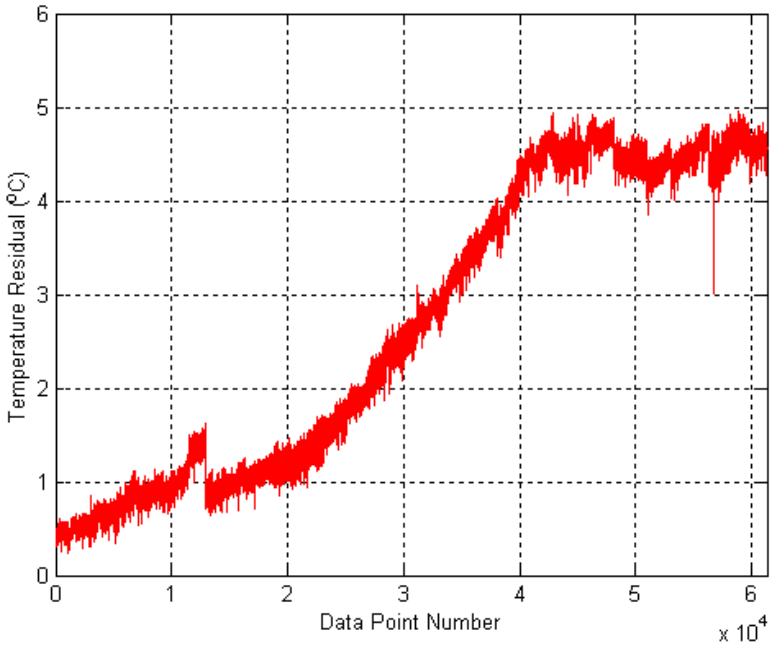

Figure 5.9. The residual between the MDH predictions of the cold-side outlet temperatures of the heat exchanger and the real experimental data.

5.5. Monitoring of Fouling in the Steam Generator

With both the normal data and data with fouling generated using the developed UTSG SIMULINK model, we first use the GMDH method to develop a data-driven model and then use the model to monitor and diagnose the fouling progress. The MATLAB code for monitoring and diagnosis of fouling in the heat exchanger is given in the Appendix.

The procedure is the same as that used above for the heat exchanger. That is, first we establish a data-driven model using the normal data. Then we use this model and the faulty data, that is, with the fouling progression, to make predictions and estimate residuals of the steam pressure. In our study, the hot-leg temperature and the number of tubes are used as the inputs for predicting steam pressure.

Figure 5.10 gives the data for UTSG steam pressure used for training and the GMDH predicted values; Figure 5.11 presents the steam pressure data used for testing and the GMDH predicted values. We see from these two figures that they both agree with each other very well.

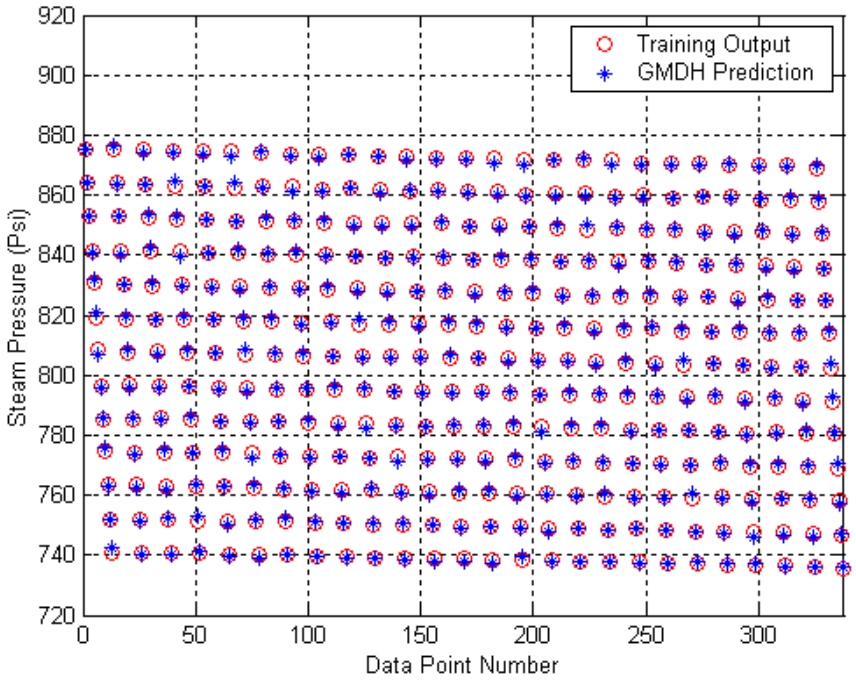

Figure 5.10. Training steam pressure and the GMDH predicted values.

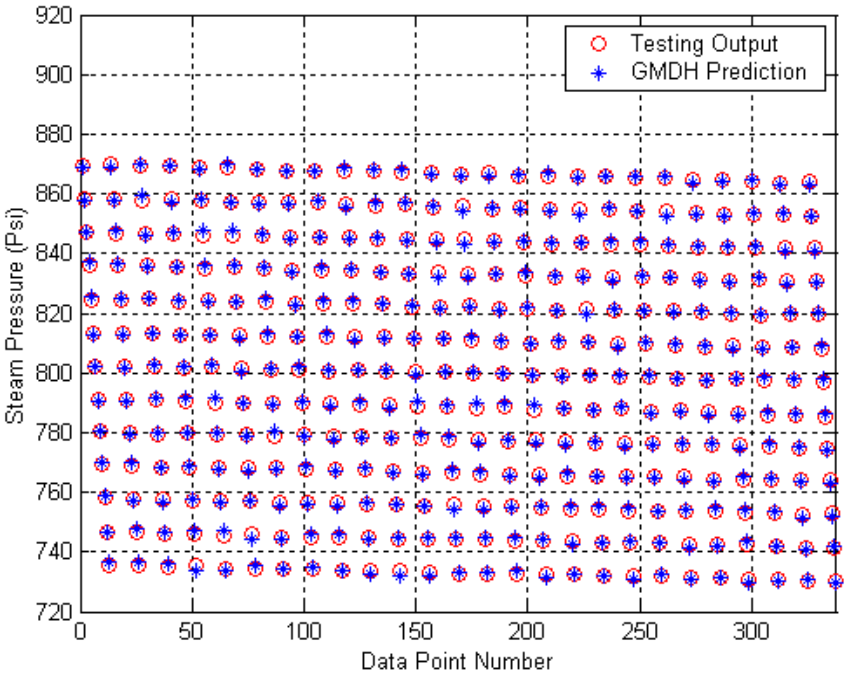

Figure 5.11. Testing steam pressure and the GMDH predicted values.

After the development of the GMDH model, we used the experimental data and the model to make new predictions. Figure 5.12 gives the GMDH predictions of the UTSG steam pressure versus the simulation results from the UTSG SIMULINK model. Figure 5.13 shows the residuals. It should be noted that the steam pressure is evaluated with different UTSG hot-side inlet temperatures. Therefore we see that there are different curve blocks in Figure 5.12. The predictions of the steam pressure with a single fixed hot-side inlet temperature are shown in Figures 5.14 and 5.15. From Figures 5.12 - 4.15, we can see that for both cases, at the initial stage of the simulated fouling progress, the estimated residual is comparatively small since there is not much fouling. Then as the fouling progresses and gradually increases, the residual also becomes larger. While finally the fouling reaches the asymptotic value and keeps constant, the residual also follows the same trend and becomes asymptotically constant.

Again, these results suggest that we can effectively use the residual trend as given in Figures 5.12 - 5.15 to monitor and diagnose the fouling problem that is occurring in a steam generator.

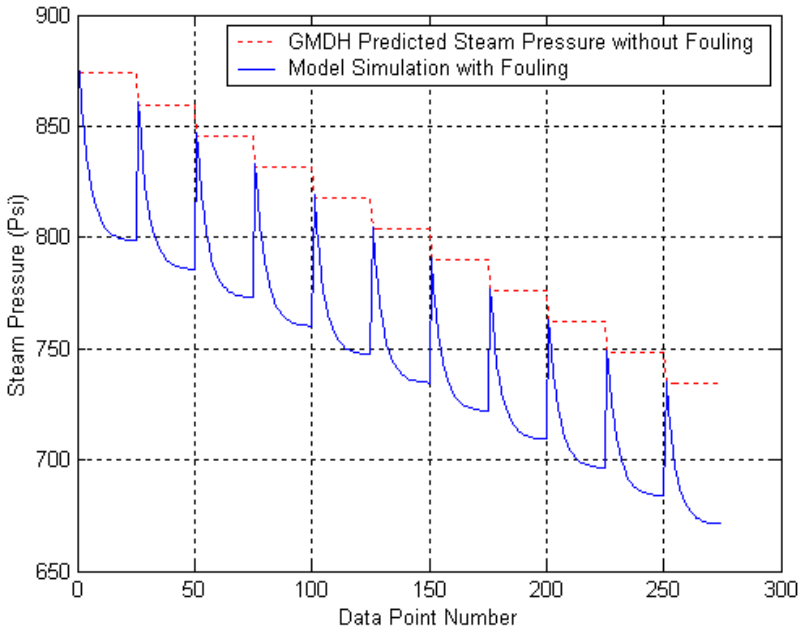

Figure 5.12. GMDH predictions of the UTSG steam pressure versus the simulations of the UTSG SIMULINK model (with different hot-side inlet temperature).

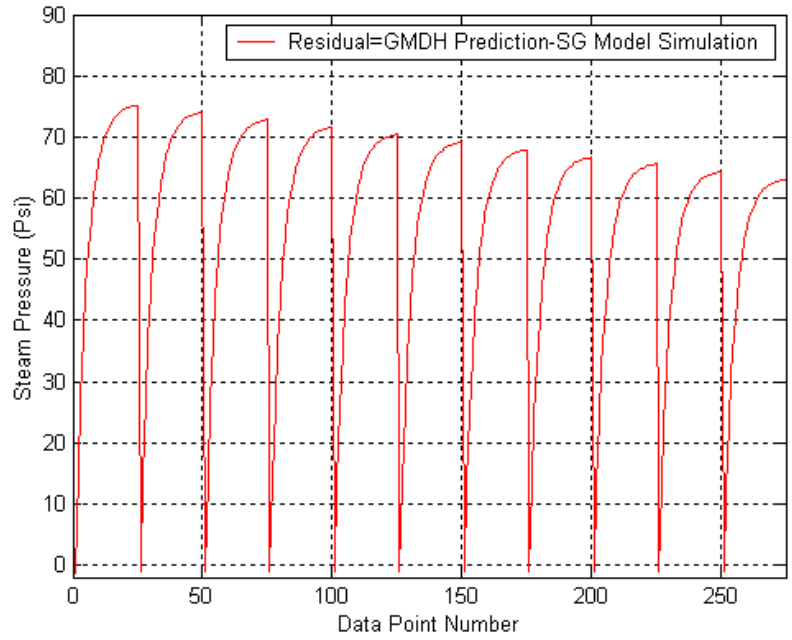

Figure 5.13. Residual between the GMDH predictions of the UTSG steam pressure and the simulations of the UTSG SIMULINK model (with different hot-side inlet temperature).

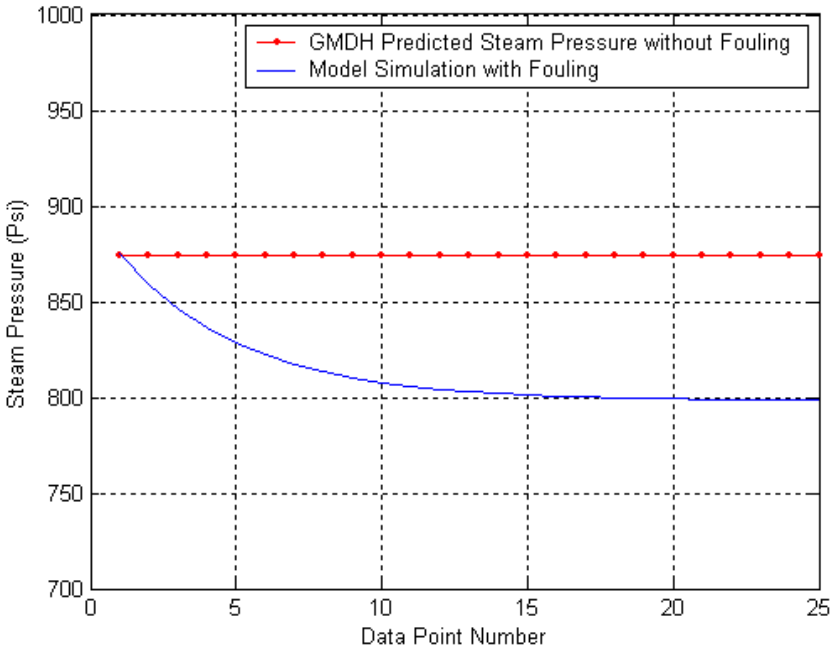

Figure 5.14. GMDH predictions of the UTSG steam pressure versus the simulations of the UTSG SIMULINK model (with a single hot-side inlet temperature).

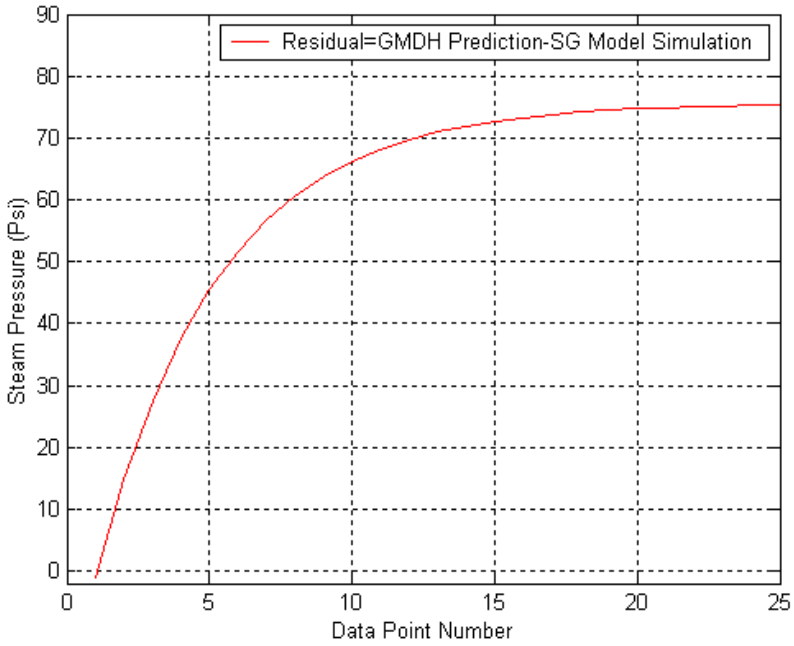

Figure 5.15. Residual between the GMDH predictions of the UTSG steam pressure and the simulations of the UTSG SIMULINK model (with a single hot-side inlet temperature).

5.6. Remarks

In this section, we used the first-principle models to generate data for development of the corresponding GMDH models for the heat exchanger and the UTSG.. These models were used to make predictions and the corresponding estimates of the residuals. It should be emphasized that for the heat exchanger we used the data collected from the experimental setup. All of the above results demonstrate that GMDH method can be successfully applied for monitoring and diagnosis of the fouling progression or other degradations that may occur in both heat exchangers and steam generators, as long as adequate data are available and the GMDH models are properly developed.

6. HYBRID MODEL DESIGN FOR STEAM GENERATOR/HEAT EXCHANGER MONITORING AND DIAGNOSIS

6.1. System Modeling for Diagnosis

A general architecture of combining first-principle and data-based models is shown in Figure 6.1. Several different modeling techniques were applied and compared. These included artificial neural networks, group method of data handling, and others.

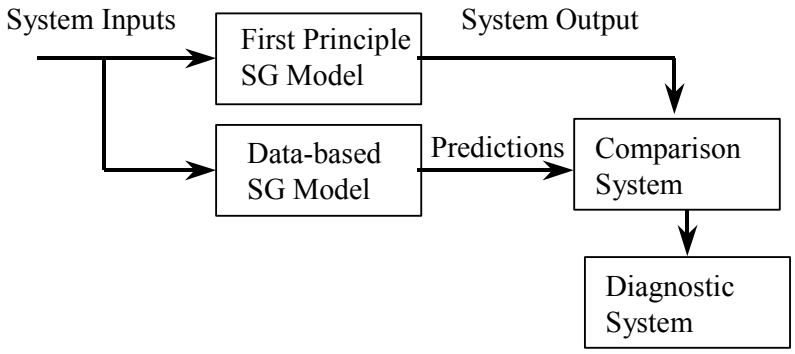

Figure 6.1. General fault detection and isolation architecture.

The two most common groups of models used in Fault Detection and Isolation (FDI) systems are first-principles models and data-based models. First-principle models do not provide the sensitivity necessary to detect slight changes in sensor calibration or plant degradation; however, data-based models have been used to accurately perform this sensitive FDI task [Gribok 2001]. Although these methods have not been applied to Steam Generator systems, the basic strategies have been applied to both nuclear systems and the balance of plant. The main thrust of this research is to develop a reliable system that may be either data-based or a hybrid system that embodies both types of models.

Data-based systems are applicable to operating plants and systems where plant data have been recorded over the entire operating range. The data based systems are only accurate when applied to the same operating conditions under which data were collected. When plant conditions or operations change, the model must extrapolate outside the training space and the results should not be trusted. Unlike linear models, which extrapolate in a known linear fashion,

non-linear models extrapolate in an unknown manner. These empirical (data-based) models must be trained on past plant data. Since automated data acquisition systems may not have been implemented on the SG systems, especially for new generation designs that have not been constructed, data may not be available and first principle models must be used and then appended with data-based models as data become available. The combination of data-based and first principle models are termed ***hybrid models***.

This hybrid framework, although more complicated, has a very important advantage. Purely data-based systems are not reliable when the system moves into new operating conditions which may result from configuration changes, new operating practices, or external factors such as unusual cold cooling water temperatures in condensers. By using the proposed hybrid system, the plant monitoring system will tend towards the first-principle model when new operating conditions are encountered and will use the data based models when in familiar operating conditions.

6.2. Hybrid Design

The first step in integrating first principles models with data-based models is an in-depth survey of the current literature. This task was begun with over 88 journal or conference papers identified. Several useful overview papers include Thompson and Kramer (1994), Wilson and Zorsetto (1997), te Braake and van Can (1998). The hybrid approach has commonly been termed a *gray-box* modeling approach, as contrasted to "black box" modeling of neural networks or other data based approaches. The term gray-box comes from the idea that a portion of the internal model, the first principle model, is explainable. In other technical papers these approaches are termed semi-mechanistic models.

There are two major approaches to hybrid, gray-box, or semi-mechanistic modeling: the *serial approach* and the *parallel approach*. The serial approach uses a data based model to construct missing inputs or parameter estimates to the first principles model, while the parallel approach uses a neural network to model non-linearities, disturbances, or other processes not accounted for in the first principles model.

6.2.1. Serial Approach

In the serial hybrid modeling approach (see Figure 6.2), neural networks are used to model parameters in the first principle models, and the first principle model is used to model the

system. These parameters may be unknown, immeasurable, changing with time, or otherwise uncertain. Psichogios and Ungar (1992) first proposed this idea in 1992 and applied it to a simulated fed-batch bioreactor. Later, Alessandri and Parisini (1997) applied the concept to a 320 MW power plant. Many other applications of the Serial Approach are available in the literature and will be investigated in more detail. Other data-driven modeling techniques, such as the *Group Method of Data Handling (GMDH)* (Ferreira and Upadhyaya, 1999) that provides a nonlinear characterization of process variables, will also be investigated.

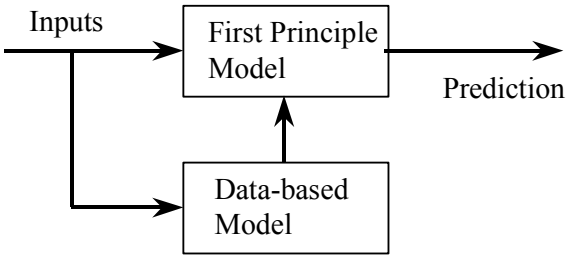

Figure 6.2. Serial Hybrid Modeling Approach.

6.2.2. Parallel Approach

In the parallel hybrid modeling approach (see Figure 4.3), a neural network is trained to predict the residuals not explained by the first principles model. When in operation, the predicted residuals are added to the first principles model output, resulting in a total prediction that is much closer to the actual system. The parallel approach was first proposed by Kramer, Thompson, and Bhagat (1992). They applied radial basis function neural networks to correct the output of a first principle model of a Continuous Stirred Tank Reactor (CSTR). In 1994 they published another paper applying the technique to a batch penicillin fermentation process (Thompson 1994). Both papers showed promising results.

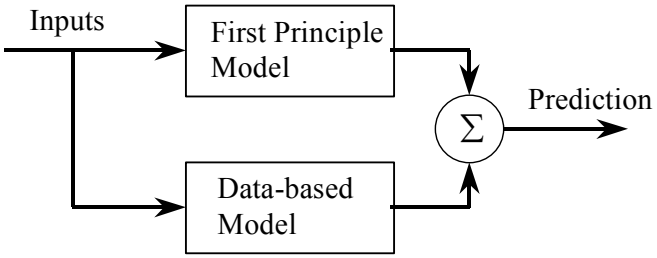

Figure 6.3. Parallel Hybrid Modeling Approach.

6.3. Development of the Heat Exchanger Model

This research investigates the application of hybrid modeling to heat exchanger monitoring and diagnostics. To understand this application we first present the methods of modeling a heat exchanger from first principles and then explain methods to integrate empirical models through series and parallel hybrid modeling.

6.3.1. Heat Exchanger Modeling

A heat exchanger is a device used to transfer heat between two fluids that are at different temperatures and are separated by a solid wall. Heat exchangers are generally classified according to the type of construction and the flow arrangement. The simplest configuration, termed double pipe, consists of two concentric tubes containing the hot and cold fluids. The flow direction of the hot and cold fluids determines whether we have a double pipe parallel flow or a double pipe counter flow heat exchanger. Another type of construction is the tube and shell arrangement that houses several internal tubes. This arrangement consists of one or more passes of the shell side fluid. The tube and shell HX provides a greater heat transfer area compared to the single tube version. Other heat exchanger arrangements are described by Incropera [1996]. For simplicity, the double pipe parallel flow concept, shown in Figure 4.4, is used in this work.

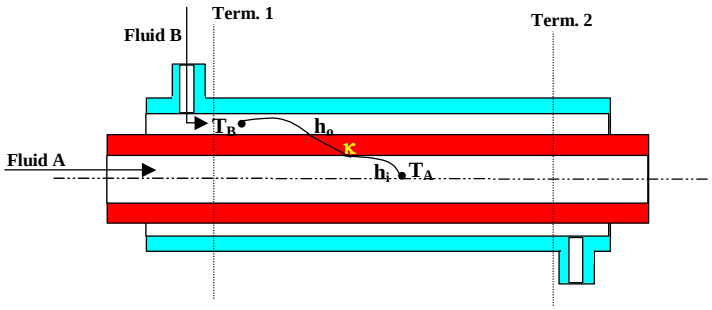

Figure 6.4. Double-pipe parallel flow heat exchanger.

Two approaches to represent the heat exchanger by first principles model are considered: the Log Mean Temperature Method and the Effectiveness-NTU Method. Both methods are based on balance energy equations applied to the heat exchanger with the amount of heat transferred by the hot fluid equal to the amount of heat received by the cold fluid:

$$Q = \dot{m} c_p^h \Delta T^h = -\dot{m} c_p^c \Delta T^c \tag{6.1}$$

where Q = heat transfer
$\dot{m}$ = mass flow rate
c_p = specific heat
ΔT = temperature difference
Superscripts h and c designate hot and cold.

6.3.2. Log Mean Temperature Difference (LMTD) Method

The overall heat transfer, Q, of a heat exchanger can be calculated by using the following expression:

$$Q = U \cdot A \cdot \Delta T_m \tag{6.2}$$

where: U = overall heat-transfer coefficient
A = total surface area for heat transfer consistent with definition of U
ΔT_m = suitable mean temperature difference across the heat exchanger.

The overall heat-transfer coefficient, ***U***, is defined as the total thermal resistance between the two fluids. It accounts for the convection thermal resistances of both hot and cold fluids and the conduction thermal resistance of the wall that separates the fluids.

The mean temperature difference across the heat exchanger ΔT_m is derived by applying the energy balance through the heat exchanger (see Equation (6.1)) in combination with Equation

(6.2), in its derivative/integral form. The complete development of ΔT_m equation is given in Holman [1981]. The log-mean temperature difference (LMTD) is given by

$$LMTD = \Delta T_m = \frac{\Delta T_1 - \Delta T_2}{\ln\left(\Delta T_1 / \Delta T_2\right)} \tag{6.3}$$

where: ΔT_m = Log Mean Temperature Difference (LMTD)
$\Delta T_1 = T_{h,1} - T_{c,1}$
$\Delta T_2 = T_{h,2} - T_{c,2}$
Indices 1 and 2 designate the two opposite ends of the heat exchanger.

To take advantage of the LMTD approach, one must know in advance the output temperatures for the cold and hot fluids. Usually the output temperatures are unknown, and then an iterative process must be employed. The LMTD method is used in this work as a simple model that is used as part of the hybrid model. In this application, an additional simplification is made in which $\mathbf{\Delta T_m}$ is calculated from the hot and cold inlet temperatures; thus, an iterative solution is not necessary. The simplified model is:

$$Q = UA(T_h - T_c) \tag{6.4}$$

6.3.3. The Effectiveness-NTU Method

The effectiveness-NTU method is an alternative approach that is used when fluid output temperatures are unknown. The effectiveness-NTU method is based on the effectiveness of the heat exchanger in transferring a given amount of heat, with effectiveness defined as the rate between the actual heat transfer and the maximum possible heat transfer

$$e \equiv \frac{Q}{Q_{\max}} \tag{6.5}$$

The maximum heat transfer is given by

$$Q_{\max} = \left(\dot{m} \times c_p\right)_{\min} \left(T_{h_{inlet}} - T_{c_{inlet}}\right) = C_{\min}\left(T_{h_{inlet}} - T_{c_{inlet}}\right) \tag{6.6}$$

where C is the fluid capacity defined as $\dot{m}c_p$; $C_{\min}$ is the hot or the cold fluid that has the minimum fluid capacity. From Equations (6.3), (6.5) and (6.6) it follows that the effectiveness is

$$e = \frac{C_h\left(T_{h_{inlet}} - T_{h_{outlet}}\right)}{C_{\min}\left(T_{h_{inlet}} - T_{c_{inlet}}\right)} \quad \text{or} \quad e = \frac{C_c\left(T_{c_{inlet}} - T_{c_{outlet}}\right)}{C_{\min}\left(T_{h_{inlet}} - T_{c_{inlet}}\right)} \tag{6.7}$$

The Number of Thermal Units (NTU) is defined as

$$NTU \equiv \frac{UA}{C_{\min}} \tag{6.8}$$

The effectiveness can be written as a function of NTU, C_{min} and C_{max}. Holman (1981) develops the effectiveness relation for the double pipe parallel flow heat exchanger as

$$\boldsymbol{e = \frac{1 - \exp[-NTU(1 + C_{\min}/C_{\max})}{1 + C_{\min}/C_{\max}}} \tag{6.9}$$

This first principle model is used in the simulations as the actual heat exchanger. It is much more accurate than the simplified model of Equation (6.4).

6.3.4. Data-Driven Modeling and Artificial Neural Networks

Neural networks are modeling techniques that learn system behavior through data acquired from that system. They are able to learn the relationship for operating regions that are presented to them during the training. If the operating region moves outside the training region, the neural network model cannot be expected to give accurate predictions.

In this work neural networks are used in the hybrid models. In the hybrid serial model, the neural network predicts the heat flow that is used in the physical model, while in the hybrid parallel model, the neural network is trained to predict the error between the simplified model (Equation (6.4)) and the actual system modeled by the NTU method.

6.4. Model Testing

The literature contains reports that compare the series and parallel hybrid approaches. van Can et al. (1996) reports that the serial approach is superior to the parallel approach and others have made similar conclusions. In this research, we compare the performance of the both method to track system changes and detect deviations from normality.

To perform these tests, a hybrid approach was used to model a heat exchanger as part of a monitoring and diagnosis system. As a first step to this goal, we simulated the actual heat

exchanger with a high fidelity model (NTU). The simulation methods reported were useful in developing the methodology for hybrid model design and implementation.

To perform the simulations, the NTU model was used to simulate normal, and faulted conditions and a hybrid model were used to monitor the heat exchanger. Departures from normality are in the form of residuals, which are the differences between the predicted outputs (hybrid model) from the actual outputs (simulated heat exchanger). The residuals were processed by a fault diagnostics system to determine the faulted conditions. This general FDI architecture is shown in Figure 6.1.

6.5. Summary of Results

The Effectiveness-NTU Model (NTU) was implemented to simulate the heat exchanger behavior. The NTU model used as inputs hot and cold inlet temperatures and hot and cold mass flow rates; the outputs are the overall heat transfer rate, and the hot and cold outlet temperatures. The fluids were the hot and cold water, and the transfer area of the heat exchanger was a known parameter (3.5 ft^2). A mean value for the heat transfer coefficient for water and this heat exchanger was assumed to be, U = 275. The input data to the NTU model was chosen to cover the range of values that would occur in the actual laboratory experiments. These values were about: Thot = 125 °F; Tcold = 65 °F; $\dot{m}_{hot} = 1000 lb/h$; $\dot{m}_{cold} = 3500 lb/h$. Additionally, small fluctuations were imposed to model normal process disturbances.

6.5.1. Hybrid Serial Model

In the hybrid serial approach, the simplified HX model was implemented to predict the hot and cold outlet temperatures using as input the hot and cold inlet temperatures and the hot and cold mass flow rates. This simplified model followed the general behavior of the heat exchanger but, intentionally, did not perform as well as the high fidelity NTU model.

The simplified HX model was implemented using a two-node approach. Each node was developed combining the relationships: $Q = (\dot{m}_h \times c_p)(T_{h_1} - T_{h_2})$ and $Q = U \cdot A \cdot LMTD$. The LMTD Equation (6.3) was simplified and approximated as $(T_{h_1} - T_{c_1})$. The two nodes were arranged in a series configuration. This way, the hot and cold outlet temperatures derived from the first node would be the inputs for the second node, in addition to the hot and cold mass flow

rates. The hot and cold outlet temperatures derived from the second node constituted the final output for the simplified HX model.

A neural network was trained through the data collected from the NTU model to predict the heat transfer value (Q) to be used in the physical model. Then, the Q that previously was calculated inside the physical model ($Q = UA(T_h - T_c)$) would now be supplied by the neural network. The serial hybrid model inputs were: the hot and cold inlet temperatures and the hot and cold mass flow rates; and the predicted variables are the hot and cold outlet temperatures, as shown in Figure 6.5.

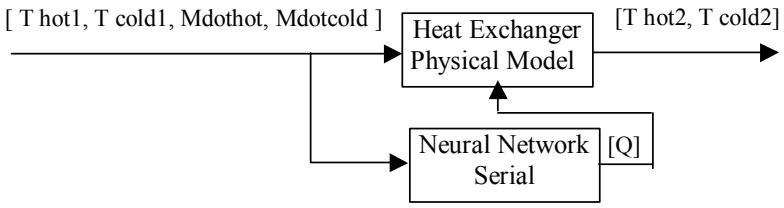

Figure 6.5. Serial hybrid model for the heat exchanger.

A test case was performed to compare the hybrid model to the actual system (NTU model). This case contained a dynamic input, which resulted in dynamic outputs. Fluctuations were imposed on the inlet hot temperature, within the training range. The fluctuations that could be seen in the output (see Figure 6.6) followed the same pattern as those imposed on the input.

The results (see Figure 6.6) show that the temperatures predicted by the series hybrid model were very close to the those from the NTU model. The error was less than 0.14%.

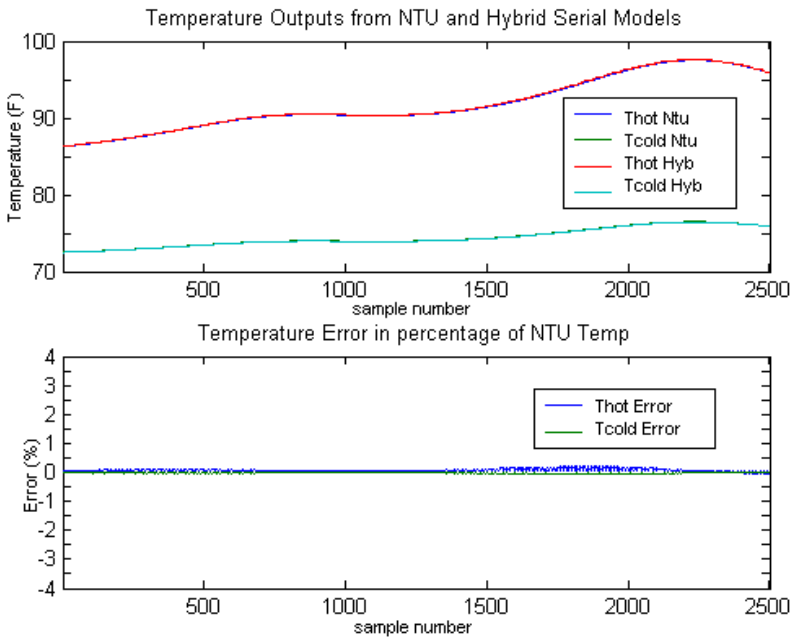

Figure 6.6. Results for serial hybrid model of the heat exchanger.

6.5.2. Hybrid Parallel Model

In the hybrid parallel approach a neural network was trained to predict the residuals in the hot and cold outlet temperatures that are not explained by the physical model. The T-Error (see Figure 6.7) is the difference between the prediction for hot and cold outlet temperatures given by the HX physical model and the values from the NTU model. The parallel hybrid model inputs are: the hot and cold inlet temperatures and the hot and cold mass flow rates; and the predicted

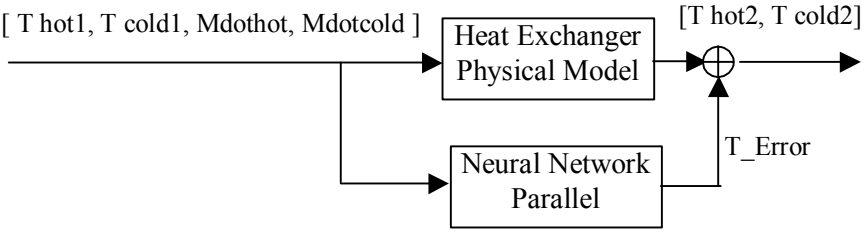

Figure 6.7. Parallel hybrid model of the heat exchanger.

variables are the hot and cold outlet temperatures (see Figure 6.7).

Fluctuations were imposed on the inlet hot temperature, within the training range, in the same manner as in the hybrid series model. The fluctuations on the output follow the same pattern as imposed on the input. The results (see Figure 6.8) showed that the temperatures

predicted by the parallel hybrid model followed those from the NTU model. The small differences in the model performances were due to a finite neural network training goal that results in finite output differences. The error in this case was less than 0.67%, which was about five times larger than that for the serial hybrid model.

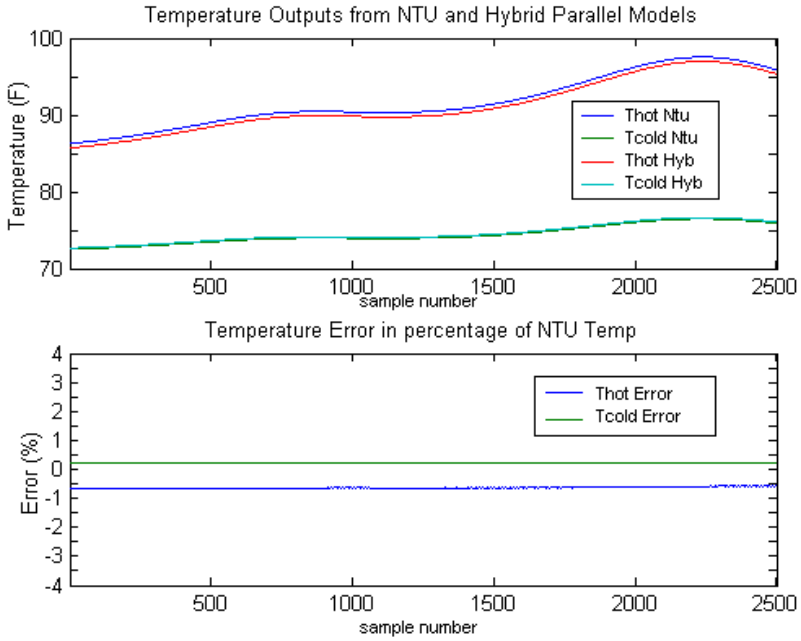

Figure 6.8. Parallel hybrid model of the heat exchanger.

6.6. Response of the Hybrid Serial Model to a Fault Condition

Fouling represents a change in the heat transfer resistance that changes the performance of heat exchangers. The usual effect is the decrease in the overall heat transfer coefficient (U). The following plot (see Figure 6.9) shows the condition in which the fouling factor was simulated by decreasing the overall heat transfer coefficient by 10%. When this operational condition was met, the neural network would produce the expected normal heat transfer coefficient for the inlet temperatures and the mass flow rates. The hybrid model generated the normal operation outputs and a comparison with the actual output showed significant differences. These differences, commonly known as residuals, will alert the user to an abnormal

condition and a fault detection and isolation (FDI) algorithm can map the residual signature to a fault hypothesis. The development of the FDI system is not discussed in this report.

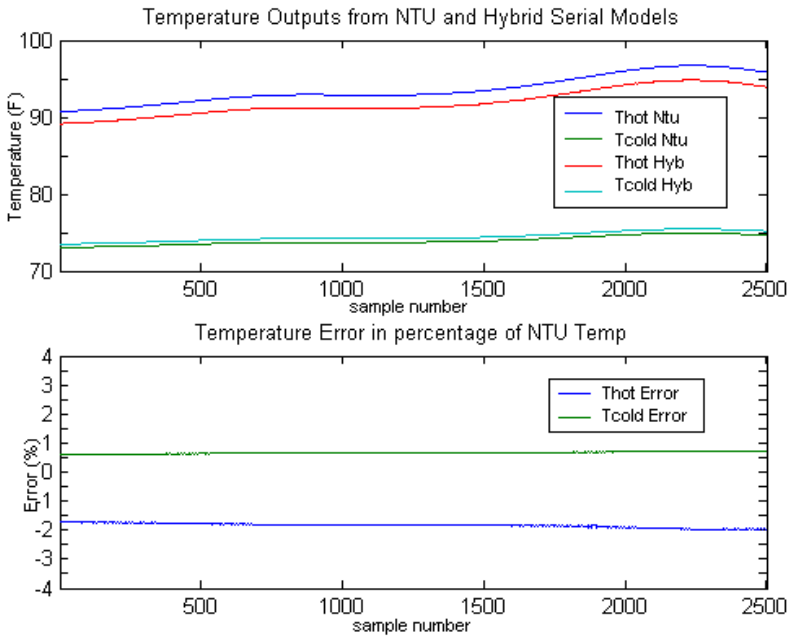

Figure 6.9. Serial hybrid model results for the fault condition.

It is interesting to note that T_{hot} has a much larger error (residual) than T_{cold}. This is because the fault causes a change in the heat transfer rate (Q). This heat transfer is related to the product of the fluid mass flow rate and the temperatures. Thus, for an equal change in Q, the temperature with a smaller mass flow rate has a higher temperature residual. In this case, the mass flow rate of the hot fluid is about a third of that of the colder fluid and the residual of the hot fluid temperature is about three times that of the cold fluid temperature.

Other fault conditions can produce different residual structures. These residual structures may include mass flow rates and pressure drops.

Remarks:

Two hybrid modeling architectures that are capable of modeling a heat exchanger are presented. Both the series and parallel hybrid approaches have small modeling errors (<1%) and the series model was shown to be able to detect a common fault condition.

6.7. Heat Exchanger Experiment

In order to accomplish this comparison of hybrid modeling techniques, a heat exchanger set up was assembled in the laboratory. The heat exchanger used in this experiment was a copper tube-and-shell structure, 24" long, with 31 internal tubes (1/4" diameter) that sit inside a 2.5" diameter shell. The HX is connected to the building hot and cold water supply in an open loop arrangement. The hot water goes through the tube side and the cold water through the shell side, in parallel flow directions. The HX is instrumented with temperature and flow rate sensors. Four type-J thermocouples allow monitoring the hot and cold water inlet and the hot and cold water outlet temperatures. Turbine type flow meters were installed in the hot and cold-water inlet piping. The temperature and flow rate signals are conditioned, and then sent to a digital data acquisition system that is based on National Instruments' hardware and LabVIEW Virtual Instrument program. See Figure 6.10 for a schematic of the HX system. The data were acquired and stored for future use. Figures 6.11 – 6.13 show the laboratory heat exchanger setup.

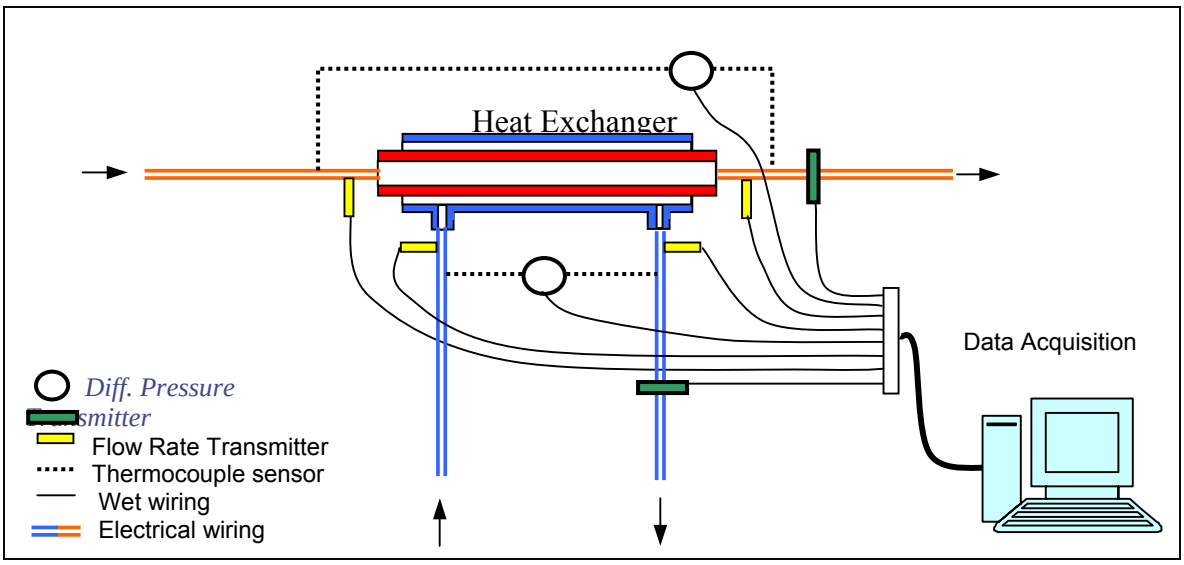

Figure 6.10. Laboratory heat exchanger system.

Figure 6.11. Photograph of the laboratory heat exchanger system.

Figure 6.12. Close-up view of the laboratory heat exchanger.

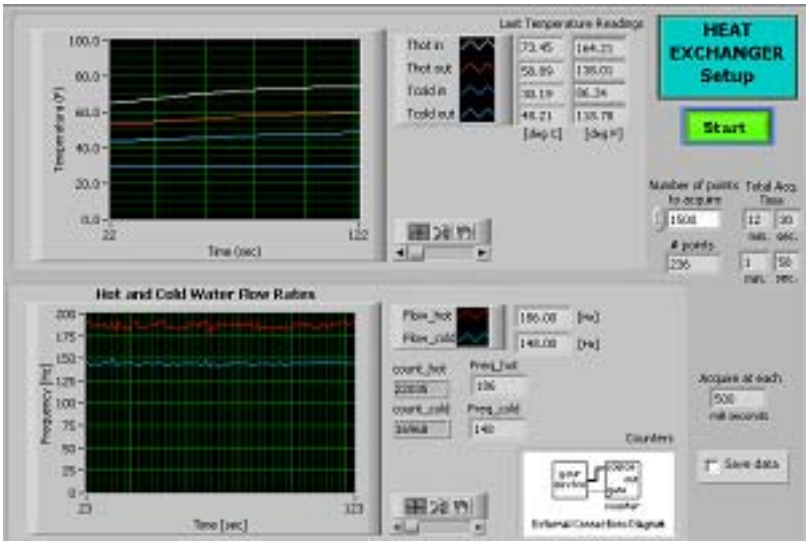

Figure 6.13. LabView based user interface.

6.7.1. Hybrid Parallel Modeling

A hybrid parallel model was developed using NTU method to implement the heat exchanger physical model and the multi-layer perceptron (MLP) neural network architecture to implement the data based model. To achieve good results, when calculating the overall heat transfer coefficient (U), the physical model takes into consideration the different Nusselt and Prandtl numbers, related to each different steady state thermodynamic condition under which the data were acquired.

The MLP neural network architecture gave better results when implemented with one neural network to predict the error in the hot water temperature and another to predict the error in the cold water temperature, instead of using just one neural network model to predict both.

In the hybrid parallel approach, a neural network was trained to predict the residuals in the hot and cold temperatures on the output of heat exchanger that are not explained by the physical model. The inputs of the model were the hot and cold temperatures of the inlet water and the hot and cold mass flow rates. Figure 6.14 shows the hybrid parallel model schematic.

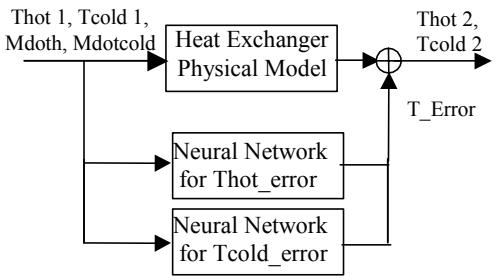

Figure 6.14. Heat exchanger parallel hybrid model.

6.7.2. Input Data

The heat exchanger was supplied with building water in an open loop arrangement. The different steady state conditions were established by varying the hot and cold water flow rates. Changing the water flow rates caused all the temperature measurements to change. The data were acquired and stored for each steady state condition. Figures 6.15-6.17 show fourteen steady state levels, each one could be characterized roughly by a medium value for the hot and cold mass flow rate and the corresponding values for the inlet cold and hot temperatures.

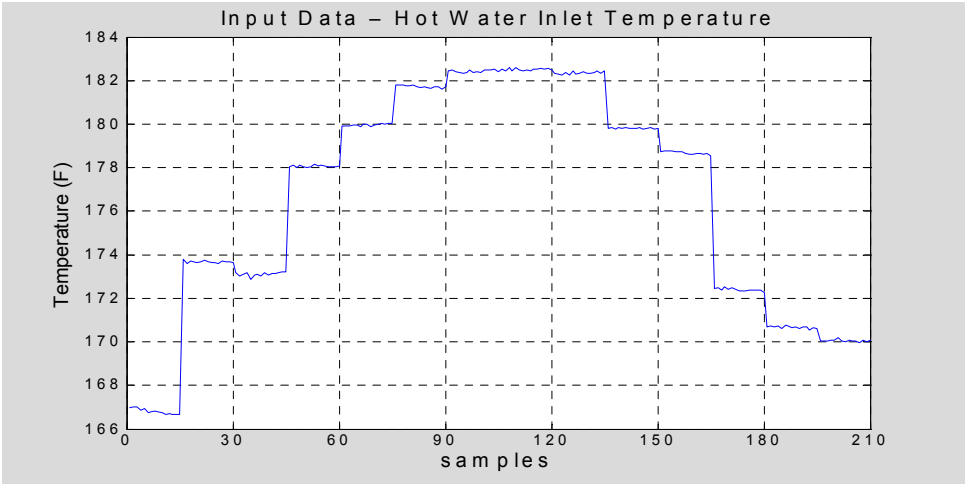

Figure 6.15. Input data: hot water inlet temperature.

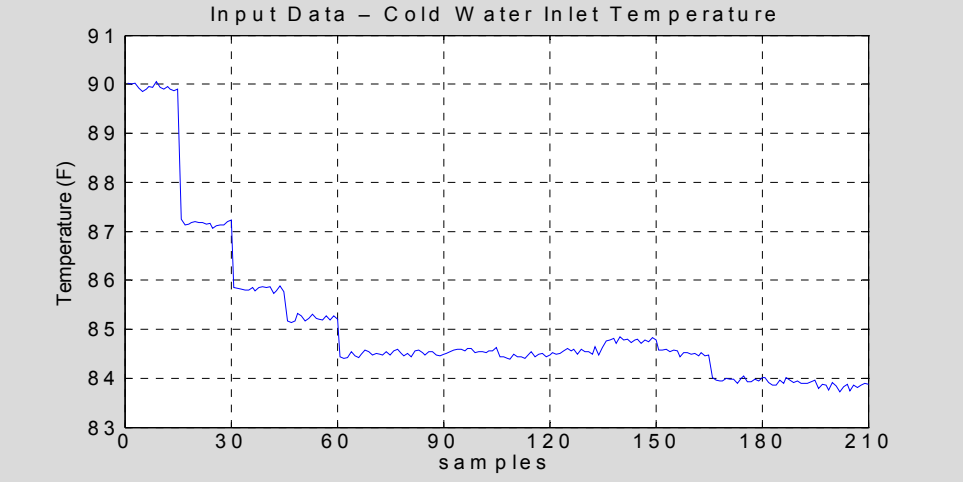

Figure 6.16. Input data: cold water inlet temperature.

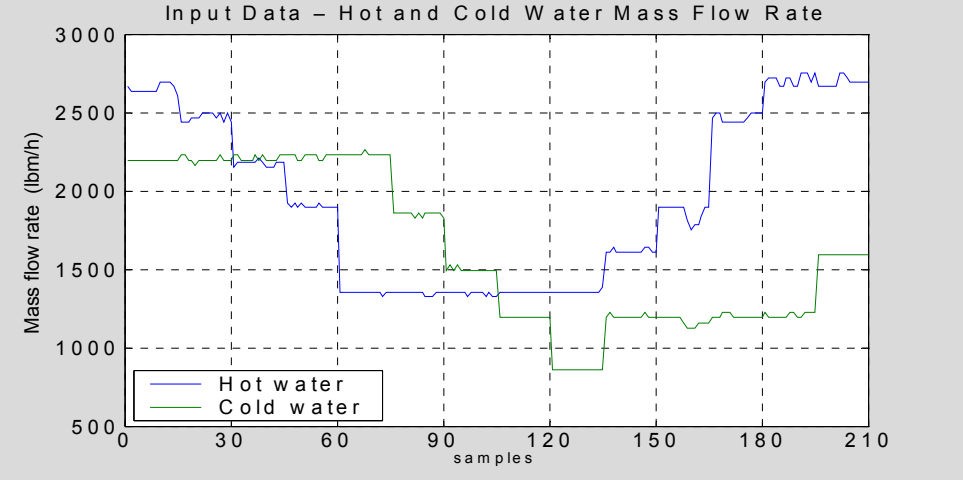

Figure 6.17. Input data: hot and cold water mass flow rate.

6.7.3. Results

Figure 6.18 shows the prediction of the physical and the parallel hybrid models for the hot water temperature prediction and its actual measurement.

The results (see Figure 6.18) show that the physical model (blue line) is not able to exactly model the temperature at each steady state condition. This is due to the use of physical models that do not consider all inputs and disturbances such as heat loss to the room. On the other hand, the parallel hybrid model (red line) follows the actual data (green line) much better.

The mean percent error, is 0.10% for the hybrid model hot temperature predictions versus 0.53% for the physical model: a performance increase of five times. The neural networks in the hybrid model attempt to explain or compensate for the residuals not taken in account by the physical model.

Figure 6.19 shows the predictions for the cold water temperature output, and similar performance can be observed. The hybrid model outperforms the physical model by a factor of about 5. The mean error, in percentage of the actual values, is 0.26% for the hybrid model predictions versus 1.37% for the physical model. The remaining error is dud to stochastic noise, unknown inputs, and other disturbances that were not modeled.

6.8. Remarks

The results show that the physical model and a parallel hybrid model architecture are capable of modeling a heat exchanger. The parallel hybrid approach has a small modeling error. The physical modeling did not perform well at all steady state conditions. The heat exchanger laboratory data have been very useful in demonstrating the effectiveness of the hybrid modeling techniques.

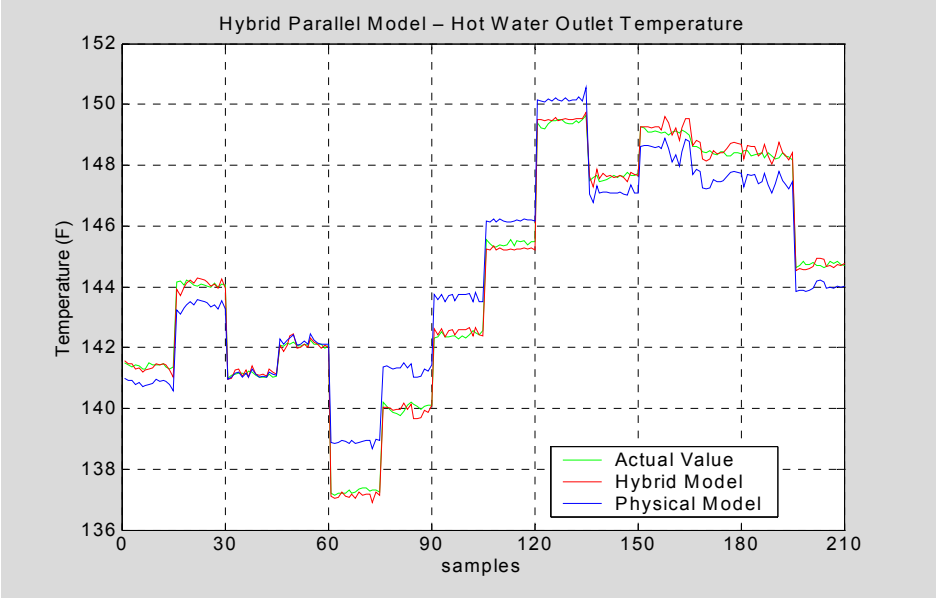

Figure 6.18. Hot temperature: hybrid and physical model predictions and measurements.

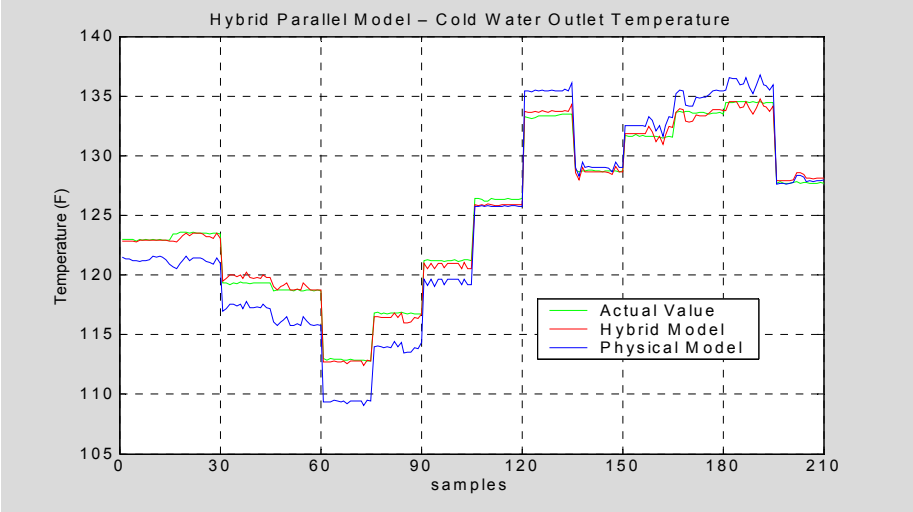

Figure 6.19. Cold temperature: hybrid and physical model predictions and measurements.

7. FAULT DIAGNOSIS DURING TRANSIENT CONDITIONS USING SUBSPACE DATA-DRIVEN MODELS

7.1. Introduction

Dynamic model based fault diagnosis is expected to have better robustness to process disturbance than steady state model based fault diagnosis. For nuclear power plants with load following capability, it becomes mandatory to utilize dynamic models for fault diagnosis. In addition, besides condition-based maintenance, reconfigurable control and transient fault diagnosis are also important to improve operation performance and safety. In these cases, automatic fault recovery can only be achieved with the help of a dynamic model based fault diagnosis system. As explained later, dynamic model based fault diagnosis requires fewer sensors for fault isolation than steady state fault diagnosis because additional temporal redundancy is utilized.

A dynamic fault diagnosis algorithm is developed for nuclear power systems in this research. In this approach, a low order state-space model is developed for fault diagnosis from currently widely used simulation tools in nuclear system design, using subspace identification techniques. The subspace identification technique is parsimonious in model parameterization because of the minimal realization of linear state space models and good numerical stability because none of nonlinear optimization algorithms is involved. In addition, linear state space model is the most well studied model for control design and fault diagnosis. After a linear state model is obtained from data generated from simulation models, model uncertainties are identified from plant measured data and explicitly formulated in fault diagnosis algorithm.

Robust parity space approach is applied to generate dynamic residuals for fault diagnosis in this research. Robust residuals are designed such that they are statistically significant if and only if there are faults involved in the system and are robust to model uncertainty and measurement noise. Fault isolation is achieved by designing structured residual set in which the residuals are sensitive to all faults but one. In this manner, the insignificant component of the generated residual vectors can be immediately used for fault isolation. Because a perfect solution can hardly be obtained to design a residual

sequence that is sensitive to a subset of faults while insensitive to the other faults, model uncertainties, and measurement noises, only a sub-optimal solution can be obtained. The optimization has been solved via a generalized eigenvalue problem in this research.

In this section, the theory of subspace identification is presented to identify a low order linear state space model from simulation models. A robust dynamic residual generator design algorithm is then developed without directly identifying model uncertainty. Finally, the developed algorithm is demonstrated through the application to IRIS HCSG system for transient fault diagnosis.

7.2. Theory of Subspace Identification

Subspace identification is the most important contribution in the field of system identification in the 1990s. The initial concepts and ideas of subspace identification were originated by De Moor in 1988 and the theory and implementation became mature in 1995 (Van Overschee and De Moor, 1995).

Subspace identification combines the theory in linear system, statistics, optimization, and numeric linear algebra for dynamic system identification. Subspace identification extracts model information from the column space of certain matrices obtained from input-output data and Kalman state information from the row space of these matrices without knowing the system matrices. The major advantage of subspace identification is that no explicit model parameterization is needed and only numeric linear algebra such as singular value decomposition and QR decomposition is needed for implementation. Therefore, subspace identification provides a robust and efficient solution to the development of dynamic models from input-output data.

A linear state space model structure is assumed in subspace identification. Although many industrial processes have nonlinearity, this nonlinearity can be handled either by recursive updating of a linear model or by using model uncertainty decoupling techniques for robust control and fault diagnosis design. Most importantly, linear state space model is the only class of systems tractable with rigorous theory. The mathematical representation of a linear state space model is as follows:

$$x_{k+1} = Ax_k + Bu_k + w_k$$
$$y_k = Cx_k + Du_k + v_k \tag{7.1}$$

where u_k is the input vector, y_k is the output vector, x_k is the state vector, and w_k and v_k are zero mean white Gaussian noise vectors with the following constant covariance structure:

$$E[\begin{bmatrix} w_i \\ v_j \end{bmatrix}(w_i^T, v_j^T)) = \begin{pmatrix} \Sigma^w & \Sigma^{wv} \\ \Sigma^{vw} & \Sigma^v \end{pmatrix}\delta_{ij} \tag{7.2}$$

On the condition that the input and output data are available, subspace identification aims at determining:

(1) The order of the unknown system.
(2) The system matrices A, B, C, D within a similarity transformation.
(3) The noise characteristic matrices Σ^w, Σ^v, and Σ^{vw}.

7.2.1. Block Data Equations

In subspace identification, block Hankel data matrices are used to extract the model information and the Kalman state information from data using geometric projection. A block Hankel matrix of a signal has its column vector stacked in rows and the stacked column vectors in time sequences arranged in columns. For instance, the block Hankel matrix of the input signal is constructed as follows:

$$U_k^s = \begin{pmatrix} u_k & u_{k+1} & \cdots & u_{k+N-1} \\ u_{k+1} & u_{k+2} & \cdots & u_{k+N} \\ \cdots & \cdots & \cdots & \cdots \\ u_{k+s-1} & u_{k+s} & \cdots & u_{k+s+N-1} \end{pmatrix} \tag{7.3}$$

where k denotes the discretized time instant of the first row and first column element, s denotes the number of row blocks and N denotes the number of columns used to construct the block Hankel matrix. The block Hankel matrix Y_k^s, W_k^s, V_k^s can be constructed similarly for the signal y, w, and v, respectively.

The extended observability matrix Γ_s relating the state vector to the stacked output vector is defined as follows:

$$\Gamma_s = \begin{bmatrix} C \\ CA \\ \dots \\ CA^s \end{bmatrix} \tag{7.4}$$

The Toeplitz block matrices H_s and G_s are further defined as follows:

$$H_s = \begin{bmatrix} D & 0 & \dots & 0 \\ CB & D & \dots & 0 \\ \dots & \dots & \dots & \dots \\ CA^{s-1}B & CA^{s-2}B & \dots & D \end{bmatrix} \tag{7.5}$$

$$G_s = \begin{bmatrix} 0 & 0 & \dots & 0 \\ C & 0 & \dots & 0 \\ \dots & \dots & \dots & \dots \\ CA^{s-1} & CA^{s-2} & \dots & 0 \end{bmatrix} \tag{7.6}$$

The concept of Kalman state sequences in system dynamics is emphasized in subspace identification. The key of subspace identification is to identify Kalman state sequences directly from the input-output data without knowing the system matrices. A Kalman state sequence involved in block data equation is defined as follows:

$$X_k = \begin{bmatrix} x_k & x_{k+1} & \cdots & x_{k+N-1} \end{bmatrix} \tag{7.7}$$

Based on the above matrices, the block data equation can be obtained as follows:

$$Y_k^s = \Gamma_s X_0 + H_s U_k^s + G_s W_k^s + V_k^s \tag{7.8}$$

In order to identify the Kalman state sequences from the input-output data using geometric projection, it is also necessary to build block Hankel matrix of the input and output signals for the past block data and the future block data separately.

Given that the past block matrix and the future block matrix have the same number of row blocks $s+1$, the past block matrix and the future block matrix of the input signal are defined as follows:

$$U_p = U_k^s \tag{7.9a}$$

$$U_f = U_{k+s+1}^s \tag{7.9b}$$

The past block matrix and the future block matrix of the output signal can be defined in the same manner.

7.2.2. Recovery of System Matrices from State Sequence

Subspace identification technique is deeply rooted in the fact that the Kalman state sequence can be identified from input-output data. If the state sequence has been determined from the input-output data without knowing the system matrices, the identification problem can be transformed to a least squares estimation problem with respect to the system matrices and the process and measurement noise covariance matrices.

Given that two adjacent state sequences $\hat{X}_{k+1}$ and $\hat{X}_k$ have been determined, they are related to the system matrices A, B, C, and D in the following manner:

$$\begin{pmatrix} \hat{X}_{k+1} \\ Y_k^s \end{pmatrix} = \begin{pmatrix} A & B \\ C & D \end{pmatrix} \begin{pmatrix} \hat{X}_k \\ U_k^s \end{pmatrix} + \begin{pmatrix} W_k \\ V_k \end{pmatrix} \tag{7.10}$$

The system matrices can then be recovered by solving a least-squares problem such that the Frobenius norm of the difference of two sides of Equation (7.10) is minimized.

Three major subspace identification algorithms N4SID (Numerical algorithms for Subspace State Space System Identification), MOESP (Multiple Output-Error State Space), and CVA (Canonical Variate Analysis) exist. These algorithms differ only in how the Kalman state sequences are extracted from input-output data and how the system matrices are recovered. Because N4SID has been implemented in the MATLAB System Identification Toolbox, the following discussion is based on N4SID algorithm.

7.2.3. Extractability of Kalman State Sequence from Input-Output Data

It will be proved that Kalman state sequence can indeed be extracted from input-output data in this section. In the next two sections, two techniques will be shown on how to obtain Kalman state sequence from input-output data.

7.2.3.1. System Decomposition

For a real system, the state variables and the system output variables are excited both by deterministic inputs and by stochastic noises. In another word, the state vector and the measurement vector can be decomposed into two components as follows:

$$\begin{aligned} x_{k+1} &= x_k^d + x_k^s \\ y_k &= y_k^d + y_k^s \end{aligned} \tag{7.11}$$

where the superscripts d and s correspond to the deterministic component and the stochastic component, respectively.

Because the involved system is linear, the system defined in Eqn. 6.1 is equivalent to the supposition of one deterministic system and one stochastic system. The deterministic subsystem is given by:

$$\begin{aligned} x_{k+1}^d &= Ax_k^d + Bu_k^d \\ y_k^d &= Cx_k^d + Du_k \end{aligned} \tag{7.12}$$

The stochastic subsystem is given by:

$$\begin{aligned} x_{k+1}^s &= Ax_k^s + w_k^s \\ y_k^s &= Cx_k^s + v_k \end{aligned} \tag{7.13}$$

In order to show the equivalency between the original system and the decomposed two subsystems, we can prove that for a given deterministic input $u(s)$ and stochastic input $w(s)$, the responses of the dynamic system, Equation (7.1) and the dynamic system Equation (7.11) are the same, and is given by

$$y(s) = C(s\mathrm{I} - A)^{-1}Bu(s) + Du(s) + C(s\mathrm{I} - A)^{-1}w(s) + v(s) \tag{7.14}$$

7.2.3.2. Extraction of Kalman State Vector

Kalman filter theory invented by R. Kalman in 1960 enables us to estimate the state vector sequences x_k for the dynamic system given by Equation (7.1) from input-

output data (Kalman, 1960). In subspace identification, we need to design a bank of Kalman filters to estimate a Kalman state sequence simply by working on the block Hankel matrix of past inputs and past outputs. In another word, the state estimate of Kalman state vector $\hat{x}_{k+1}$ needs to be derived from the information up to the time instant k only. Because this is the theoretical foundation of subspace identification, we are going to prove that this is indeed true in this research.

It is obvious from Equation (7.1) that the estimated mean of the state vector $\bar{x}_k$ propagates in the following manner:

$$\begin{aligned} \bar{x}_{k+1} &= A\bar{x}_k + Bu_k \\ \bar{x}_0 &= x_0 \end{aligned} \tag{7.15}$$

$\bar{x}_0$ = the initial state estimate of the process.

Apparently, the estimated mean of the state vector $\bar{x}_k$ follows exactly the deterministic part of the dynamics defined in Equation (7.1). However, $\bar{x}_k$ is different from x_k^d since the initial state estimate is still a random variable.

The covariance matrix P_x of the estimation error of state vector propagates as follows:

$$\begin{aligned} P_{x,k+1} &= E[(x_{k+1} - \bar{x}_{k+1})(x_{k+1} - \bar{x}_{k+1})^T] \\ &= AP_{x,k}A^T + \Sigma^w \end{aligned} \tag{7.16}$$

The estimated mean value of the output vector $\bar{y}_k$ is as follows:

$$\bar{y}_k = C\bar{x}_k + Du_k \tag{7.17}$$

The covariance matrix P_y of the estimation error of output vector propagates as follows:

$$P_{y,k} = E[(y_k - \bar{y}_k)(y_k - \bar{y}_k)^T] = CP_{x,k}C^T + \Sigma^v \tag{7.18}$$

The covariance matrix between the state estimate and the output is given by

$$P_{xy,k} = E[(x_k - \bar{x}_k)(y_k - \bar{y}_k)^T] = P_{x,k}C^T \tag{7.19}$$

In subspace identification, the state estimate of Kalman state vector $\hat{x}_{k+1}$ is determined using only the information up to the time instant k. This is quite different from the classical Kalman filtering setting where the full input-output information including the current information is used. In classical Kalman filtering, the information up to the time instant $k+1$ is used to estimate the state $\hat{x}_{k+1}$.

For this reason, it is assumed that the estimate of the state vector $\hat{x}_{k+1}$ is a linear function of the available system output y_k, which is given by:

$$\hat{x}_{k+1} = Ky_k + g \tag{7.20}$$

K is a matrix and g is a vector to be determined.

The optimal state estimate can be obtained by minimizing the objective function given by

$$J = E[(x_{k+1} - \hat{x}_{k+1})^T (x_{k+1} - \hat{x}_{k+1})] \tag{7.21}$$

The above minimization problem is equivalent to minimizing the following objective function:

$$\begin{aligned} J &= tr\{E[(x_{k+1} - (Ky_k + g))(x_{k+1} - (Ky_k + g))^T]\} \\ &= tr\{E[(x_{k+1} - \hat{x}(k+1|k) - (Ky_k + g - \hat{x}(k+1|k))) \\ &\qquad (x_{k+1} - \hat{x}(k+1|k) - (Ky_k + g - \hat{x}(k+1|k)))^T]\} \end{aligned} \tag{7.22}$$

Substituting $y_k = y_k - \bar{y}_k + \bar{y}_k$ into Equation (7.22) and noticing Equation (7.18), the minimal value is reached when the following conditions are satisfied:

$$\frac{\partial J}{\partial g} = 2(g - \hat{x}(k+1|k)) + 2K\bar{y}(k) = 0 \tag{7.23a}$$

$$\begin{aligned} \frac{\partial J}{\partial K} = 2K(P_{y,k} + \bar{y}_k \bar{y}_k^T) - 2E[(x_{k+1} - \hat{x}(k+1|k))(y_k - \bar{y}_k))^T] \\ + 2(g - \hat{x}(k+1|k))\bar{y}_k^T = 0 \end{aligned} \tag{7.23b}$$

The solution is then given by:

$$g = \hat{x}(k+1|k) - K\bar{y}_k \tag{7.24a}$$
$$K = E[(x_{k+1} - \hat{x}(k+1|k))(y_k - \bar{y}_k)^T]P_{y,k}^{-1} \tag{7.24b}$$

After cumbersome algebra, the non-steady state Kalman state estimate $\hat{x}_{k+1}$ can be obtained by the following recursive formula.

$$\hat{x}_{k+1} = A\hat{x}_k + Bu_k + K_k[y_k - C\hat{x}_k - Du_k] \tag{7.25a}$$
$$K_k = E[(x_{k+1} - \hat{x}(k+1|k))(y_k - \bar{y}_k)^T]P_{y,k}^{-1} = AP_{x,k}C^T + \Sigma^w \tag{7.25b}$$
$$P_{y,k} = E[(y_k - \bar{y}_k)(y_k - \bar{y}_k)^T] = CP_{x,k}C^T + \Sigma^v \tag{7.25c}$$

The covariance of the state estimation error is given by:

$$\begin{aligned} P_{x,k+1} &= E[(x_{k+1} - \hat{x}_{k+1})(x_{k+1} - \hat{x}_{k+1})^T] \\ &= E[(Ax_k + w - A\hat{x}_k - K_k(y_k - \bar{y}_k))(Ax_k + w - A\hat{x}_k - K_k(y_k - \bar{y}_k))^T] \\ &= AP_{x,k}A^T + \Sigma^w + (AP_{x,k}C^T + \Sigma^w)(CP_{x,k}C^T + \Sigma^v)^{-1}(AP_{x,k}C^T + \Sigma^w)^T \end{aligned} \tag{7.26}$$

If the recursive form of Kalman state estimate given in Equation (7.25) is written explicitly, the non-steady state Kalman state estimate is as follows:

$$\hat{x}_k = \begin{pmatrix} L_1 & L_2 & L_3 \end{pmatrix} \begin{pmatrix} \hat{x}_0 \\ u_0 \\ \cdots \\ u_{k-1} \\ y_0 \\ \cdots \\ y_{k-1} \end{pmatrix} \tag{7.27}$$

L_1, L_2, and L_3 are three linear operators acting on the initial state, the past input vectors, and the past output vectors, respectively.

Although the derivation of Kalman state estimate is a natural extension of the classical Kalman filter, the theoretic foundation of subspace identification has been established,

which ensures that the Kalman state estimate $\hat{x}_k$ can be obtained by expressing itself as a linear function of the past $k-1$ inputs and outputs as well as the initial state estimate.

7.2.3.3. Extraction of Kalman State Sequence

Based on Equation (7.27), the k-th block row of the process state, which is X_k based on the notation of Equation (7.7), is written in the matrix form as follows:

$$\begin{aligned}\hat{X}_k &= \begin{pmatrix}\hat{x}_k & \hat{x}_{k+1} & \cdots & \hat{x}_{k+N-1}\end{pmatrix} \\ &= \begin{pmatrix}L_0 & L_P\end{pmatrix}\begin{pmatrix}\hat{X}_0 \\ -- \\ W_p\end{pmatrix}\end{aligned} \tag{7.28}$$

$\hat{X}_0$ = the estimate of the initial state sequence.

$$W_p = \begin{pmatrix}U_p \\ Y_p\end{pmatrix}$$

Equation (7.28) indicates that the Kalman state sequence can be generated by a bank of non-steady state Kalman filters working in parallel on each of the columns of the block Hankel data matrix of past inputs and past outputs. If the estimate of the initial state vector $\hat{x}_0$ and the covariance matrix of the initial state estimate error $P_{x,0}$ are known, the estimate of the state vector $\hat{x}_k$ can be obtained by an iteration of a Kalman filter over k time steps. The Kalman state sequence $\hat{X}_k$ can be obtained by running N paralleled non-steady state Kalman filters simultaneously in the same manner if the estimate of the initial state sequence $\hat{X}_0$ is known.

The last but not the least point of subspace identification is that the estimated Kalman state sequence is not unique, which depends on the choice of the initial state sequence and the covariance matrix of initial state estimation error. In another word, the recovered system matrices based on subspace identification may not be able to reproduce the true system states. However, through appropriate choice of the initial state sequence, the input-output responses of the identified system will be the same as the real system.

7.2.4. Orthogonal Projection Methods

The objective of subspace identification is to recover Kalman states from input-output data without the knowledge of system matrices. Subspace identification technique achieves Kalman state estimate by exploring the relationship among the spaces of the input, output, and state sequences through geometric projection. In orthogonal projection methods, we constrain the row space of the identified Kalman state sequence to be in the combined row space of W_P and U_f.

Starting from Equation (7.28), it can be proved that an estimate of the future output block matrix Y_f, denoted by Z_f, is a linear combination of the past information block matrix W_p and the future input block matrix U_f, which is given by:

$$Z_f = (L_p, L_u)\begin{pmatrix} W_p \\ U_f \end{pmatrix} \tag{7.29}$$

L_p = a linear operator acting on W_p.
L_u = a linear operator acting on U_f.

The prediction error of future output can be represented by the Frobenius norm given by:

$$\| Y_f - (L_p, L_u)\begin{pmatrix} W_p \\ U_f \end{pmatrix} \|_F \tag{7.30}$$

To make the prediction error minimized with the constraint that the rows of Z_f lives in the joint row space of W_P and U_f, it can be proved that the optimal solution to the minimization problem with the specified constraint is to perform an orthogonal projection of the row space of the matrix Y_f onto the joint row space of matrix W_p and U_f (Favoreel, De Moor, and Van Overschee, 1998).

The orthogonal projection of the row space of matrix A onto the row space of matrix B is computed in the following manner:

$$C = A/B = AB^T (BB^T)^{-1} B$$

Theorem 7.1: If the deterministic input u_k is uncorrelated with the process noise w_k and the measurement noise v_k; the input u_k is persistently excited of order 2k; the number of measurements goes to infinity $N \to \infty$; and the process noise w_k and the measurement noise v_k are not identically zero, then we have (Van Overschee and De Moor, 1996):

$$Z_k = Y_f / \begin{pmatrix} W_p \\ U_f \end{pmatrix} = \Gamma_s \hat{X}_k + H_s U_f \tag{7.31}$$

Theorem 7.1 shows one way to predict the future output based on the past inputs and outputs as well as the current inputs without the information of the system matrices. More importantly, Theorem 6.1 gives the relationship between the Kalman state estimate and the input-output data in a direct manner assuming that the row space of $\hat{X}_k$ lives in the joint row space of matrix W_p and U_f.

7.2.5. Oblique Projection Methods

Although Theorem 7.1 gives the relationship between the Kalman state estimate and the optimal prediction of the future output through an orthogonal projection, it is not convenient in implementation to recover the Kalman state directly because the future input term U_f is involved. To overcome this difficulty arising from the term U_f, an oblique projection method can be used to relate the Kalman state estimate to the oblique projection matrix with the constraint that the row space of Kalman state sequence lies in the row space of matrix W_p such that the future block Hankel matrix U_f will have no effects on the obtained projection matrix.

Starting from the orthogonal projection theory, it is quite intuitive to obtain the oblique projection, which is as follows:

$$Y_f /_{U_f} W_p = \Gamma_s \widetilde{X}_k$$

$\widetilde{X}_k$ is the initial Kalman filter state estimate involved in the oblique projection.

The oblique projection of the row space of matrix A along the row space of matrix B onto the row space of matrix C is computed in the following manner:

$$A/_B C = [A/B^{\perp}][C/B^{\perp})^{+} C$$

$A/B^{\perp}$ represents the orthogonal projection of the row space of A onto the orthogonal complement of the row space of B. Obviously, $B/_B C = 0$.

Theorem 7.2: If the deterministic input u_k is uncorrelated with the process noise w_k and the measurement noise v_k; the input u_k is persistently excited of order 2k; the number of measurements goes to infinity $N \to \infty$; and the process noise w_k and the measurement noise v_k are not identically zero.

Let O_k be defined as the oblique projection as follows:

$$O_k = Y_f /_{U_f} W_p \tag{7.32}$$

If singular value decomposition is performed on the oblique projection matrix, then we have

$$O_k = \begin{pmatrix} U_1 & U_2 \end{pmatrix} \begin{pmatrix} S_1 & 0 \\ 0 & 0 \end{pmatrix} \begin{pmatrix} V_1^T \\ V_2^T \end{pmatrix} = U_1 S_1 V_1^T \tag{7.33}$$

The following claims can be stated (Van Overschee and De Moor, 1996):

(1) The matrix O_k is equal to the product of the extended observability matrix Γ_S and the estimated Kalman filter state sequence $\hat{X}_k$, that is:

$$O_k = \Gamma_S \hat{X}_k \tag{7.34}$$

(2) The order of the system is equal to the number of singular values of O_k that are not zero.

(3) The extended observability matrix Γ_S can be obtained as follows:

$$\Gamma_S = U_1 S_1^{1/2} T \tag{7.35}$$

T is a similarity transformation matrix.

(4) The part of the state sequences $\hat{X}_k$ can be computed as follows:

$$\hat{X}_k = T^{-1} S_1^{1/2} V_1^T$$

(5) The state sequences $\hat{X}_k$ is related to the matrix O_k as follows:

$$\hat{X}_k = \Gamma_S^+ O_k \tag{7.36}$$

Theorem 7.2 provides an optimal solution to the linear combination of past inputs and outputs, that is, $O_k = L_p W_p$ so that the prediction error of the future output is minimized with respect to the Frobenius norm. The row space of this optimal solution O_k is the projection of the row space of Y_f along the row space of U_f onto the row space of W_p.

For a system with l outputs and n true states, the oblique projection matrix O_k has $k \cdot l$ rows and N columns, whose rows span a subspace of $k \cdot l$ dimensional row space in the N dimensional ambient space. However, only n states are sufficient to predict the future output from the past information. Therefore, it is necessary for subspace identification to determine the true number of states from the oblique projection matrix. In mathematics, this problem can be formulated as follows:

$$\min_{R \in R^{li \times q}} \| O_k - R \|_F^2 \tag{7.37}$$

with the constraint that the rank of R is n.

The best solution to the minimization problem given in Equation 7.37) is as follows:

$$R \approx O_k = \Gamma_k \hat{X}_k = U_1 S_1 V_1^T \tag{7.38}$$

The columns of Γ_k spans n-dimensional space because the original system is observable and the rows of $\hat{X}_k$ are n-dimensional since the system has n states. Because the oblique projection matrix O_k is a product of $\hat{X}_k$ and Γ_k, the rank of O_k is indeed equal to n.

Moreover, the column space of O_k is the same as the column space of Γ_k since each column of O_k is nothing but a linear combination of the columns of Γ_k as is shown in Equation (7.38). For the same reason, the row space of O_k is the same as the row space of $\hat{X}_k$ since each row of O_k is nothing but a linear combination of the rows of $\hat{X}_k$ as is also shown in Equation (7.38). Therefore, after a singular decomposition of O_k, there are theoretically only n nonzero singular values. However, for a real world problem where N is not infinite and there may be nonlinearity, the singular value decomposition of O_k does not always produce zero singular values. In this situation, the predominant singular values are used to determine the order of system dynamics.

Because the column space of O_k is the same as the column space of Γ_k and the row space of O_k is the same as the row space of $\hat{X}_k$, Equation (6.38) can then be split into two parts as follows:

$$\begin{aligned} \Gamma_k &= U_1 S_1^{1/2} T \\ \hat{X}_k &= T^{-1} S_1^{1/2} V_1^T \end{aligned} \tag{7.39}$$

Therefore, Equations (7.35) and (7.36), can be used to estimate the extended observability matrix Γ_k and the Kalman state sequence $\hat{X}_k$ directly from the input and output data without the knowledge of system matrices.

At this point, Kalman state sequence has been identified from the input-output data without the knowledge of system matrices, the dynamic system identification is then transformed to a least squares estimation problem, which is described in Section 7.2.2.

Example 1: Given two matrices A and B and a matrix $C = AB$ as follows:

$$A=\begin{bmatrix}1.0 & 1.0\\ 2.0 & 7.0\\ 1.0 & -1.0\\ 2.0 & 2.0\\ 3.0 & 0.0\end{bmatrix} \qquad B=\begin{bmatrix}1.0 & 2.0 & 3.0\\ 2.0 & 1.0 & 1.0\end{bmatrix}$$

$$C=\begin{bmatrix}3.0 & 3.0 & 2.0\\ 16.0 & 11.0 & -1.0\\ -1.0 & 1.0 & 4.0\\ 6.0 & 6.0 & 4.0\\ 3.0 & 6.0 & 9.0\end{bmatrix}$$

The matrix A has 2-dimensional column space and the matrix B has 2-dimenisonal row space. It can be verified that the rank of C is also 2. If singular value decomposition is performed on C, we have:

$$C=U_1S_1V_1^T=\begin{bmatrix}-0.1993 & -0.114\\ -0.8275 & 0.4611\\ -0.0277 & -0.3896\\ -0.3986 & -0.2280\\ -0.3405 & -0.7554\end{bmatrix}\begin{bmatrix}22.7163 & 0\\ 0 & 10.7688\end{bmatrix}\begin{bmatrix}-0.7582 & -0.6234 & -0.1448\\ 0.3521 & -0.1448 & -0.9247\end{bmatrix}$$

Obviously, the matrix C has two non-zero singular values. Because U_1 is orthonormal, it is always possible to find a transformation matrix $T=S_1^{-0.5}U_1^TA$ such that $A=U_1S_1^{0.5}T$ and $B=T^{-1}S_1^{0.5}V_1^T$. The matrix T is a full rank square matrix and thus invertible because the matrix A has full column rank as same as the rank of S_1. For the example problem, the transformation matrix T is given by:

$$T=\begin{bmatrix}-0.7764 & -1.4186\\ -0.7019 & 0.9287\end{bmatrix}$$

This simple example clearly shows the reasoning behind Equation (7.39). It should be emphasized that subspace identification is based on the major result of Equation (7.34) with three significant implications:

(1) The projection matrix can be obtained directly from input-output data;
(2) The column space of Γ_k has the same dimension as the number of states.

(3) The row space of $\hat{X}_k$ has the same dimension as the number of states.

In fact, subspace identification theory is established by revealing the equivalence between the column space of a projection matrix and the column space of the extended observability matrix and the equivalence between the row space of the projection matrix and the row space of the Kalman state sequence. It is because of the importance of subspace that this identification technique was given the name of subspace identification.

7.3. Robust Dynamic Fault Diagnosis Algorithm

After system dynamics is identified either from plant simulations or from on-line experimental data using subspace identification technique, the developed model will always have certain degrees of uncertainty either because the simulation does not truly represent the physical system or because a model reduction is implicitly performed in subspace identification.

In general, the uncertainty of a dynamic model can be represented as follows (Chen and Patton, 1999):

$$\begin{aligned} x(k+1) &= Ax(k) + Bu^*(k) + w(k) + d(k) \\ y^*(k) &= Cx(k) + Du^*(k) \end{aligned} \tag{7.40}$$

where $d(k)$ is a vector representing deterministic model uncertainty, $w(k)$ is a vector representing stochastic process noise, $u^*(k)$ is the true input vector, and $y^*(k)$ is the true output vector.

In Equation (7.40), the model uncertainty term plays the same role on the system dynamics as the process disturbance defined in Equation (7.1) except that model uncertainty is deterministic. In fact, the model uncertainty term is an extension of process disturbance from modeling point of view, which may arise from unmeasured inputs, non-linear terms in system dynamics, terms related to time-varying dynamics, linearization and model reduction, parameter variation, and simulation model uncertainty, etc.

Given that the measured inputs and outputs are corrupted with some measurement noise v_u and v_y, respectively, and some additive sensor faults, the observed input vector $u(k)$ and the observed output vector $y(k)$ are then as follows:

$$u(k) = u^*(k) + v_u(k) + E_u f_u(k) \quad (7.41a)$$

$$y(k) = y^*(k) + v_y(k) + E_y f_y(k) \quad (7.41b)$$

$f_u(k)$ and $f_y(k)$ are the fault magnitude vectors and E_u and E_y are the fault distribution matrices for the inputs and the outputs, respectively.

The objective of robust fault detection is to generate a residual that is statistically significant **if and only if** the fault magnitude vectors are not zero, i.e., the residual $r(t)$ satisfies the following property:

$$r(t) \neq 0 \quad \text{iff} \quad f_u(t) \neq 0 \text{ or } f_y(t) \neq 0 \quad (7.42)$$

If different residual patterns are predefined to signify different faults, the task of fault isolation is then to design some residual generators such that each fault must generate the predefined residual pattern regardless of its fault magnitude. Such a formulation of fault isolation problem can avoid the use of fault information for fault isolation, which may depend on fault magnitude and is difficult to obtain in nuclear power systems.

7.3.1. Robust Dynamic Fault Detection Algorithm

Considering a time window of length S, the dynamic redundancy relation in stacked vector form can be derived for the given system defined in Eqn. 6.40 as follows:

$$y_s^*(k) = \Gamma_s x(k-s) + H_s u_s^*(k) + G_s d_s(k) + G_s w_s(k) \qquad (7.43)$$

where $y_s^*(k)$, $u_s^*(k)$, $w_s(k)$, and $d_s(k)$ are stacked column vectors of s elements of $y^*(k)$, $u^*(k)$, $w(k)$, and $d(k)$, respectively. The matrices H_s and G_s are Toeplitz block matrices that relate the system inputs and the model uncertainty to the system outputs, respectively.

The stacked output error vector within the given time window can be written as follows:

$$e_s(k) = y_s(k) - H_s u_s(k) = \tilde{H}_s \tilde{z}_s(k) \qquad (7.44)$$

$$\tilde{H}_s = \begin{pmatrix} \mathrm{I} & -H_s \end{pmatrix}$$
$$\tilde{z}_s(k) = \begin{pmatrix} y_s^T(k) & u_s^T(k) \end{pmatrix}^T$$

From Equations (7.43) and (7.44), the stacked output error vector can be rewritten in its physical form as follows (Li and Shah, 2002):

$$e_s(k) = \Gamma_s x(k-s) + G_s d_s(k) + G_s w_s(k) + \tilde{H}_s \begin{pmatrix} v_{ys}(k) \\ v_{us}(k) \end{pmatrix} + \tilde{H}_s E_z f_{sz}(k) \qquad (7.45)$$

$$E_z = \begin{pmatrix} \mathrm{I}_{s+1} \otimes E_y & 0 \\ 0 & \mathrm{I}_{s+1} \otimes E_u \end{pmatrix}$$

I_{s+1} is a s dimensional identity matrix, $\otimes$ represents the Kronecker product, and $f_{sz}(k)$ is the stacked fault magnitude vector combining both the output faults and the input faults.

Equations (7.44) and (7.45) represent the computational form of the output error and its internal form from system physics, respectively. In order to construct a residual signal insensitive to the initial states and the model uncertainty, a linear transformation is performed on the original stacked output error vector. That is, a residual vector $r_s(k)$ can

be designed for robust fault detection through a linear transformation matrix V_0 with the following constraints:

$$r_s(k) = V_0(y_s(k) - H_s u_s(k)) \quad (7.46a)$$
$$V_0 \Gamma_s x(k-s) = 0 \quad (7.46b)$$
$$V_0 G_s d_s(k) = 0 \quad (7.46c)$$

Accordingly, the internal form of the residual vector takes the following simplified form:

$$r_s(k) = V_0 \tilde{H}_s \begin{pmatrix} v_{ys}(k) \\ v_{us}(k) \end{pmatrix} + V_0 G_s w_s(k) + V_0 \tilde{H}_s E_z f_{sz}(k) \quad (7.47)$$

If there is no measurement and process noise, the internal form of the residual vector defined in Equation (7.47) is only a function of the fault magnitude. Therefore, such a residual generator has the desired property for robust fault detection.

The residual vector generated from Equation (7.47) follows a multi-dimensional Gaussian distribution that is zero-mean with a covariance matrix that can be determined from the data obtained for fault free conditions. If a sensor fault occurs to the system, Equation (7.47) indicates that the fault condition residual vector will also follow a multi-dimensional Gaussian distribution with the same covariance matrix but with a non-zero mean value. Therefore, fault detection can be achieved by detecting the change of the mean value of the generated residual vectors. In order to avoid false alarms and missing detection rates due to noise, an Exponentially Weighted Moving Average (EWMA) filter (Lowry etc., 1992) can be applied to the residual vector (Qin and Li, 2001), which is given by:

$$\bar{r}_s(k) = \gamma \cdot \bar{r}_s(k-1) + (1-\gamma) r_s(k) \quad (7.48)$$

where $\bar{r}_s(k)$ is the EWMA filtered residual vector and γ is the forgetting factor for filtering.

The filtered residual vector for fault free condition also follows zero mean Gaussian distribution with the covariance matrix $\bar{R}_{s0}(k)$ given by (Del Castillo, 2002):

$$\overline{R}_{s0}(k) = \frac{1-\gamma}{1+\gamma}(R_{s0}(k) + 2\sum_{j=1}^{s}\gamma^{j} E\{r_s(k) r_s(k-j)^T\}) \tag{7.49a}$$

$R_{s0}(k)$ is the covariance matrix of the unfiltered residual vector.

To simplify the computation, asymptotic covariance matrix can be used, which is given by (Rigdon, 1995):

$$\lim_{s\to\infty} \overline{R}_{s0}(k) = \frac{\gamma}{2-\gamma} R_{s0}(k) \tag{7.49b}$$

The filtered square weighted residual can be used for fault detection with better performance than a simple weighted residual, which is given by:

$$\overline{\beta}_s(k) = \overline{r}_s^T(k)(\overline{R}_{s0})^{-1}\overline{r}_s(k) \tag{7.50}$$

During fault free condition, the filtered square weighted residual $\overline{\beta}_s(k)$ follows a central χ^2 distribution. If $\overline{\beta}_s(k)$ does not follow a central χ^2 distribution at a specified significance level α, the decision can then be made that a fault has occurred to the system at this significance level. That is, a fault is detected if the fault detection index $\omega_s(k)$ is greater than 1.0, which is defined as follows:

$$\varpi_s(k) = \frac{\overline{\beta}_s(k)}{\chi_\alpha^2} \tag{7.51}$$

7.3.2. One-Step Robust Dynamic Residual Generator Design

As described in Section 7.3.1, the key of robust fault detection is to design a linear transformation matrix such that the generated residuals are independent of the initial states and insensitive to the model uncertainties, which is written in Equation (7.46). The traditional method of dealing with model uncertainty in robust residual generator design has two steps. The first step is to determine the model uncertainty vector using Kalman

filter technique and the second step is to determine the uncertainty distribution matrix using SVD algorithm.

A new approach has been developed for robust dynamic residual generator design in this research. Inspired by subspace identification algorithm, this approach utilizes block data matrix equation to determine the relationship between the subspace spanned by the projection matrix of measured data and the subspace spanned by the projection matrix of model uncertainty. The advantage of this approach is that robust residual generator design does not need to identify the model uncertainty vector and the distribution matrix explicitly.

Let us recall the block data matrix Y_k , U_k , P_k , W_k , $V_{u,k}$, $V_{y,k}$ and Z_k defined for the output, input, model uncertainty, process disturbance, input noise, output noise, and past information, which are written as follows:

$$Y_k = \begin{bmatrix} y_s(k) & y_s(k+1) & \cdots & y_s(k+N-1) \end{bmatrix} \tag{7.52a}$$

$$U_k = \begin{bmatrix} u_s(k) & u_s(k+1) & \cdots & u_s(k+N-1) \end{bmatrix} \tag{7.52b}$$

$$P_k = \begin{bmatrix} d_s(k) & d_s(k+1) & \cdots & d_s(k+N-1) \end{bmatrix} \tag{7.52c}$$

$$W_k = \begin{bmatrix} w_s(k) & w_s(k+1) & \cdots & w_s(k+N-1) \end{bmatrix} \tag{7.52d}$$

$$V_{u,k} = \begin{bmatrix} v_{us}(k) & v_{us}(k+1) & \cdots & v_{us}(k+N-1) \end{bmatrix} \tag{7.52e}$$

$$V_{y,k} = \begin{bmatrix} v_{ys}(k) & v_{ys}(k+1) & \cdots & v_{ys}(k+N-1) \end{bmatrix} \tag{7.52f}$$

$$Z_k = \begin{pmatrix} Y_k \\ U_k \end{pmatrix} \tag{7.52g}$$

The block data matrix equation can be derived as follows:

$$Y_{k+1} = \Gamma_s X_{k+1} + H_s U_{k+1} - H_s V_{u,k+1} + G_s P_{k+1} + G_s W_{k+1} + V_{y,k+1} \tag{7.53}$$

If we post-multiply the Equation (6.53) by Z_k^T , then we have the equation

$$Y_{k+1} Z_k^T = \Gamma_s X_{k+1} Z_k^T + H_s U_{k+1} Z_k^T - H_s V_{u,k+1} Z_k^T + G_s P_{k+1} Z_k^T + G_s W_{k+1} Z_k^T + V_{y,k+1} Z_k^T \tag{7.54}$$

Considering that the model uncertainty is a deterministic variable, and the input measurement noise, the output noise, and the process noise are all uncorrelated white Gaussian, if the size of data is sufficiently big, then we have:

$$\Omega_{YZ} = \Gamma_s \Omega_{XZ} + H_s \Omega_{UZ} + G_s \Omega_{PZ} \tag{7.55}$$

Ω denotes the corresponding product term in Equation (7.54).

If Equation (7.55) is then premultiplied by the complement matrix of Γ_s, denoted by $\Gamma_s^{\perp}$, then we have:

$$\Gamma_s^{\perp}(\Omega_{YZ} - H_s \Omega_{UZ}) = \Gamma_s^{\perp} G_s \Omega_{PZ} \tag{7.56}$$

The left hand side of Equation (7.56) can be determined from the measured data and the right side of the equation is related to the space spanned by the model uncertainty vectors. Therefore, singular value decomposition can be performed on the related matrix on the left side of the equation to determine the null space spanned by the model uncertainty vectors.

Let us redefine the matrix on the left side of Equation (7.56) as Θ, that is:

$$\Theta = \Gamma_s^{\perp}(\Omega_{YZ} - H_s \Omega_{UZ}) \tag{7.57}$$

If a singular value decomposition is performed on Θ, we have:

$$\Theta = \begin{bmatrix} U_\Theta & U_\Theta^{\perp} \end{bmatrix} \begin{bmatrix} S_\Theta & 0 \\ 0 & 0 \end{bmatrix} \begin{bmatrix} V_\Theta \\ V_\Theta^{\perp} \end{bmatrix} \tag{7.58}$$

Obviously, the obtained matrix U_Θ satisfies the following equation:

$$(U_\Theta^{\perp})^T (\Gamma_s^{\perp} G_s P_{k+1}) Z_k^T = 0 \tag{7.59}$$

If there is at least one columns of Z_k^T which do not live in the null space of $(U_\Theta^{\perp})^T (\Gamma_s^{\perp} G_s P_{k+1})$, then we have:

$$(U_\Theta^{\perp})^T (\Gamma_s^{\perp} G_s P_{k+1}) = 0 \tag{7.60}$$

If it is further assumed that the model uncertainty is piecewise constant, a linear transformation matrix V_0 satisfying the desired property of robust residual generator defined in Equation (7.46), can be chosen as follows:

$$V_0 = (U_\Theta^\perp)^T (\Gamma_s^\perp) \tag{7.61}$$

Based on the above algorithm, robust residual generator can be designed without knowing the model uncertainty vector. Compared with the classical approach developed by Chen and Patton, 1999, this algorithm is much easier for implementation.

Example 2: Considering a linear dynamic system with four inputs and four outputs, the system matrices are identified as follows:

$$A = \begin{bmatrix} 0.5 & 0.5 \\ -0.5 & 0.5 \end{bmatrix} \qquad B = \begin{bmatrix} -0.4 & 0.1 & -1.1 & 1.2 \\ 1.7 & 0.3 & 1.2 & -0.1 \end{bmatrix}$$

$$C = \begin{bmatrix} 0.3 & -0.6 \\ 0.2 & 2.2 \\ 0.2 & -0.2 \\ 0.7 & 0.2 \end{bmatrix} \qquad D = \begin{bmatrix} 0 & 0 & 0 & 0 \\ 0 & 0 & 0 & 0 \\ 0 & 0 & 0 & 0 \\ 0 & 0 & 0 & 0 \end{bmatrix}$$

The fault free data is generated with measurement noise of 1% signal-noise ratio for all the four input signals and the four output signals, and process noise of 3% signal-noise ratio, and model uncertainty of constant direction. The distribution matrix and the magnitude vector of model uncertainty are given as follows:

$$E_d = \begin{bmatrix} 0.25 & 0.5 \\ 0.5 & 0.25 \end{bmatrix} \qquad d = \begin{bmatrix} 10.0 \\ 10.0 \end{bmatrix}$$

Because the number of state variables is 2 in this example, the block data matrix of Y_k, U_k, and Z_k can be constructed with s equal to 2 and N equal to 2000 according to Equation (7.52), where the system is excited with input signal $u = \sum_{i=1}^{10} \cos(i\pi t)$ and the initial state vector $x(0) = \begin{bmatrix} 0 & 0 \end{bmatrix}^T$.

After the extended observability matrix Γ_s is constructed from the system matrices, the dimension of the matrix is 12 by 2. If singular value decomposition is performed on Θ defined in Eqn 6.57, which has a dimension of 10 by 24, we have the following singular values from large to small in order, 3.2281e+006, 4.5777e+003, 121.3397, 59.2458, 1.5377, 0.9983, 0.1805, 0.0910, 0.0230, and 0.0164. Because a sharp drop occurs at the second singular value, the last nine left singular vectors can be retained to design robust residual generator for fault detection. In fact, if we remove the measurement noise and process noise, the last 9 singular values of Θ would be exactly zeros.

Figure 7.1 shows a comparison between the residual norms without the model uncertainty decoupled and with the model uncertainty decoupled. The new test data of 2000 samples are generated by exciting the system with input $u = \sum_{i=1}^{10} \sin(i\pi t)$ beginning with the initial state vector $x(0) = \begin{bmatrix} 1.0 & 1.0 \end{bmatrix}^T$ and introducing the model uncertainty since the 1000th sample.

The upper plot of Figure 7.1 shows the results when the model uncertainty is not decoupled. As can be seen, the residuals are small before the 1000th sample although the system is excited by a different input signal at a different initial state vector. However, false alarms will be produced after the 1000th sample. The lower plot shows the results when the model uncertainty is decoupled using the developed algorithm in this section. It can be seen that the generated robust residuals will not produce false alarms after the 1000th sample when model uncertainty has been introduced.

The simple example has demonstrated that the developed robust residual generation algorithm is able to decouple model uncertainty without the need to identify model uncertainty vector explicitly.

7.3.3. Robust Fault Isolation Algorithm

Structured residuals generated by multiple residual generators provide a simple and systematic approach to fault isolation. If residual generators are designed such that each one is only sensitive to a subset of the considered faults, a fault isolation scheme can then be achieved since each fault corresponds to a different residual pattern.

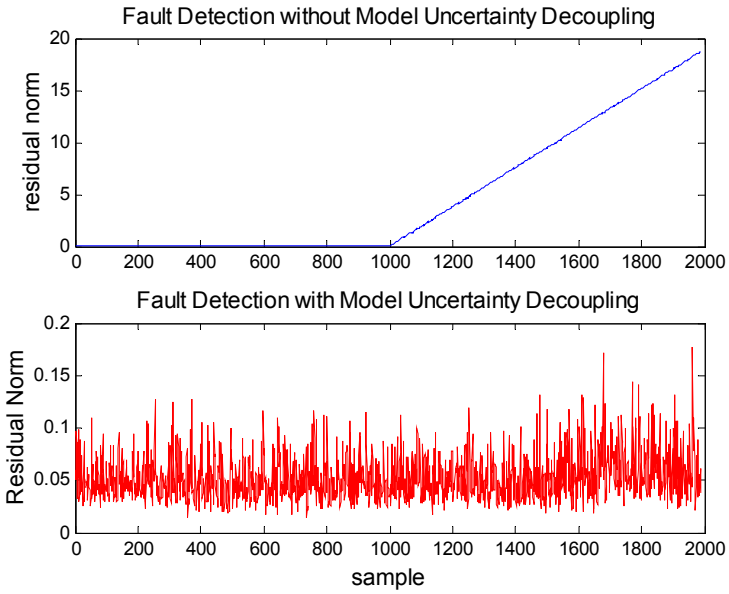

Figure 7.1. Robust fault detection for the example case during normal operation condition.

Although it is possible to design numerous residual structures for fault isolation with different isolation capability, a generalized residual set is a simple design scheme for single fault isolation (Qin and Li, 2001). In this scheme, each residual set is sensitive to all faults but one. In particular, the residual structure dedicated to the isolation of the i^{th} fault is given as follows:

$$r_i(t) = 0 \qquad \text{for the } i^{th} \text{ fault.} \tag{7.62a}$$

$$r_i(t) \neq 0 \qquad \text{for the other faults.} \tag{7.62b}$$

The fault direction matrix E_u and E_y are decomposed into the first part $E_{ui,1}$ and $E_{yi,1}$ corresponding to the faults to be desensitized, and the second part $E_{ui,2}$ and $E_{yi,2}$ corresponding to the faults to be sensitized, that is

$$E_{ui} = \begin{pmatrix} E_{ui,1} & E_{ui,2} \end{pmatrix} \tag{7.63a}$$

$$E_{yi} = \begin{pmatrix} E_{yi,1} & E_{yi,2} \end{pmatrix} \tag{7.63b}$$

The primary residual vector for robust fault detection defined in Eqn. 6.47 can then be rewritten as follows:

$$r_s(k) = V_0 \widetilde{H}_s \begin{pmatrix} v_{ys}(k) \\ v_{us}(k) \end{pmatrix} + V_0 G_s w_s(k) + V_0 \widetilde{H}_s E_{z1} f_{sz1}(k) + V_0 \widetilde{H}_s E_{z2} f_{sz2}(k) \qquad (7.64)$$

where E_{z1} and E_{z2} are constructed from $E_{ui,1}$, $E_{yi,1}$ and $E_{ui,2}$, $E_{yi,2}$, respectively, in the same manner as E_z is constructed from E_u and E_y.

The residual generator V_i dedicated to the isolation of the i^{th} fault is designed as follows:

$$V_i \cdot V_0 \widetilde{H}_s E_{z1} = 0 \qquad (7.65)$$

In order to make the residual generator given in Equation (7.65) still sensitive to the other considered faults, the transformation matrix V_i can be obtained by solving an optimization problem such that its row vectors v can minimize the objective function J defined as follows:

$$J = \frac{(vM_1)(vM_1)^T}{(vM_2)(vM_2)^T} \qquad (7.66)$$

$$M_1 = V_0 \widetilde{H}_s E_{z1}$$
$$M_2 = V_0 \widetilde{H}_s E_{z2}$$

A complicated algorithm based on Cholesky decomposition and standard eigen-problem is developed to solve the above optimization problem in (Li and Shah, 2002). In this research, the optimization is formulated as a generalized eigen-problem defined as follows:

$$M_1 M_1{}^T v^T = \lambda M_2 M_2{}^T v^T \qquad (7.67)$$

Similarly, in order to remove the noise effects on decision-making, an EWMA filter can also be applied to each of the generated residual vectors and an FDI index is used to check its significance of change. The FDI index is defined as follows:

$$\varpi(k) = \frac{\overline{\beta}_s(k)}{\chi_\alpha^2} \qquad (7.68)$$

7.4. Application to IRIS HCSG System

The developed algorithm was applied to the sensor fault diagnosis using the dynamic model identified from the data generated by the IRIS HCSG simulation model (Upadhyaya and Zhao, 2003). The considered sensor faults include both the input and the output faults related to the system model.

7.4.1. System Description

International Reactor Innovative and Secure (IRIS) is one of the Generation IV nuclear reactor designs for near term deployment (Carelli et al., 2003). The IRIS reactor is an integral light-water reactor (LWR). The reactor coolant systems including steam generators, pumps, and pressurizer are all integrated inside the reactor vessel. This integral design eliminates the possibility of large loss of coolant accidents. The reactor has eight Helical Coil Steam Generators (HCSG) connected to four steam lines and four feed water lines. The long lifetime core is achieved by means of 5 percent enriched uranium for the first reactor core and 9 percent enriched uranium for successive reactor cores. The reactor refueling is needed only at the end of the first five years, and afterwards once every eight years. Because of the deep burnup, fewer amount of nuclear waste per unit of reactor power is produced than current operating reactors.

The HCSG systems are major contributors to the safety and economy of the IRIS reactor design. The size of steam generators can be reduced through the helical coil design. The heat transfer of the coiled configuration is much more efficient than straight tubes because of the larger heat transfer area per unit volume and the secondary flow induced by the coil geometry. The probability of steam generator tube rupture can be reduced because secondary fluid flows inside SG tubes and thus the tube walls experience compression force from the outside, reducing the likelihood of stress corrosion cracking. In addition, these steam generators produce superheated steam, which avoids the need to install a steam-water separator in the steam generator.

In the HCSG system, a schematic of which is shown in Figure 7.2, the primary fluid flows downward from the top to the bottom on the shell side. The primary side heat transfer is sub-cooled forced convection along the entire steam generator height and the secondary fluid flows upward inside the coiled tubes from the bottom to the top of the

steam generator. The feed water flows into the sub-cooled region of the steam generator. In the sub-cooled region, the heat transfer is mainly due to single-phase turbulent and molecular momentum transfer and the pressure loss is mainly due to wall friction. The saturated region begins when the bulk temperature becomes saturated. The heat transfer in the saturated boiling region is dominated by nucleate boiling, which is much more efficient than single-phase liquid or steam heat transfer. In the saturated boiling region, the generated bubbles do not disappear in the liquid core and the pressure loss is not only due to the wall friction but also due to the interfacial drag between the bubbles and the liquid. In the HCSG system, the length of liquid film heat transfer is short since the flow velocity is relatively high (about 1.5 m/s). Saturated boiling ends when the critical heat flux is reached and the liquid film disappears. Because of the relatively large mass flow rate (62.85 kg/s), the critical heat flux occurs at relatively high steam quality. When the steam quality becomes 1.0, the liquid evaporation ceases and the steam becomes superheated.

In the HCSG system, the steam pressure is controlled and the steam pressure sensor fault will propagate within the control loop. The feed water flow rate is regulated when reactor power changes, so it is important to have a correct indication of the feed water flow rate for this power transient. The detailed results are therefore presented for these two sensor faults. To demonstrate the systematic solution to sensor FDI of the developed approach, the FDI results of all the other sensor faults are also summarized.

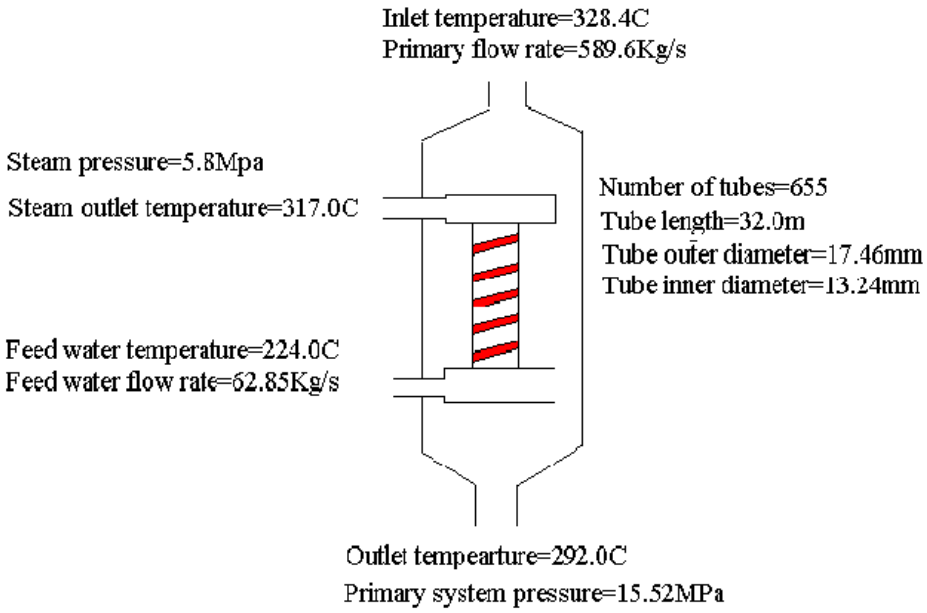

Figure 7.2. Schematic of IRIS HCSG system.

7.4.2. Data Generation and Subspace Identification

A linear state space model is identified for the HCSG system at full power operation condition using subspace identification technique. The data characterizing the system dynamics is generated by exciting the simulation model with white Gaussian noise inputs of 1% power. The perturbed inputs include the hot leg temperature, the primary flow rate, the feed water flow rate, the feed water temperature, and the steam flow rate. The appropriate choice of the excitation inputs plays a significant role in the quality of the identified model. If too much power is included in the input signals, some nonlinear modes will be excited. On the contrary, if the included power is too small, the identified model cannot capture enough system dynamics.

Figure 7.3 shows the singular values of the oblique projection matrix for different number of state variables ranging from 1 to 50. The number of states is chosen as five since a significant breakpoint can be observed at this point. If too many state variables are chosen, the resulting model will lose the capability of generalization because some of the degrees of freedom will be used to model the system noise. If too few state variables are used, the resulting model may not be able to explain some significant dynamics of the system. In general, the number of state variables should be chosen such that no

significant information can be included if it is further increased. As can be seen from the figure, a reduced order model can indeed be developed through a systematic approach of subspace identification. The original nineteen order physical model has been reduced to a five order empirical model that can still capture the dominant dynamics of the system.

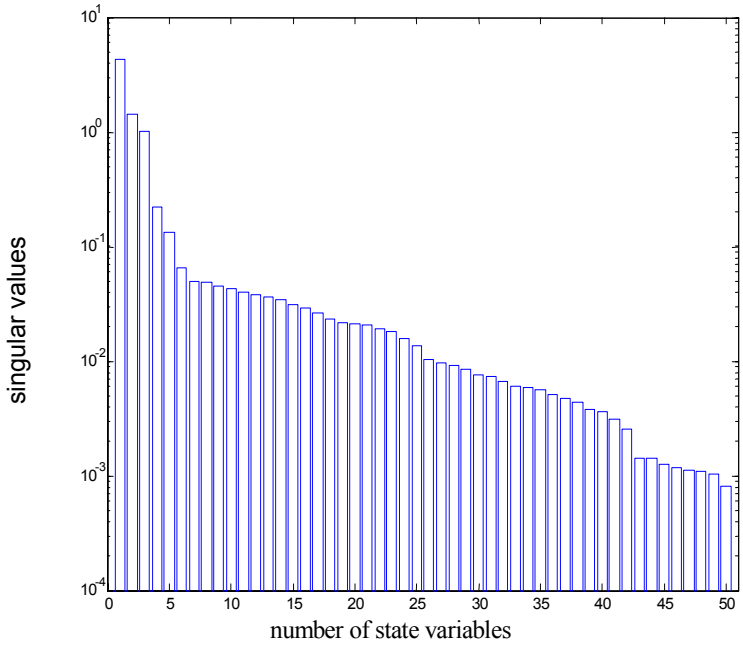

Figure 7.3. The singular values of the projection matrix.

In order to test the generalization capability of the identified model, a test data set is generated with the reactor power at 90% full power and the input excitation power of 0.5%. Figure 7.4 shows the comparison of results between the cold leg temperature obtained from the simulation model and the corresponding predicted values based on the identified model. The prediction errors are indeed very small.

The prediction error index γ can be used to quantify the prediction performance of the identified model, which is given by (Favoreel, De Moor, and Van Overschee, 1998):

$$\gamma = \sqrt{\sum_{k=1}^{N}(y_k - \hat{y}_k)^2 / \sum_{k=1}^{N} y_k^2} \tag{7.69}$$

where N is the number of test data points, y_k is the actual value of the kth data point, and $\hat{y}_k$ is the predicted value of the kth data point.

The prediction error indices are 11.2%, 8.3%, 8.8%, 10.6%, 10.2% and 8.3% for the cold leg temperature, the steam pressure, the steam outlet temperature, the sub-cooled length and the saturated boiling length, respectively. These small indices show that the identified model is able to give a good prediction for all the outputs even if the reactor is operating at a different power level with different magnitude of perturbations.

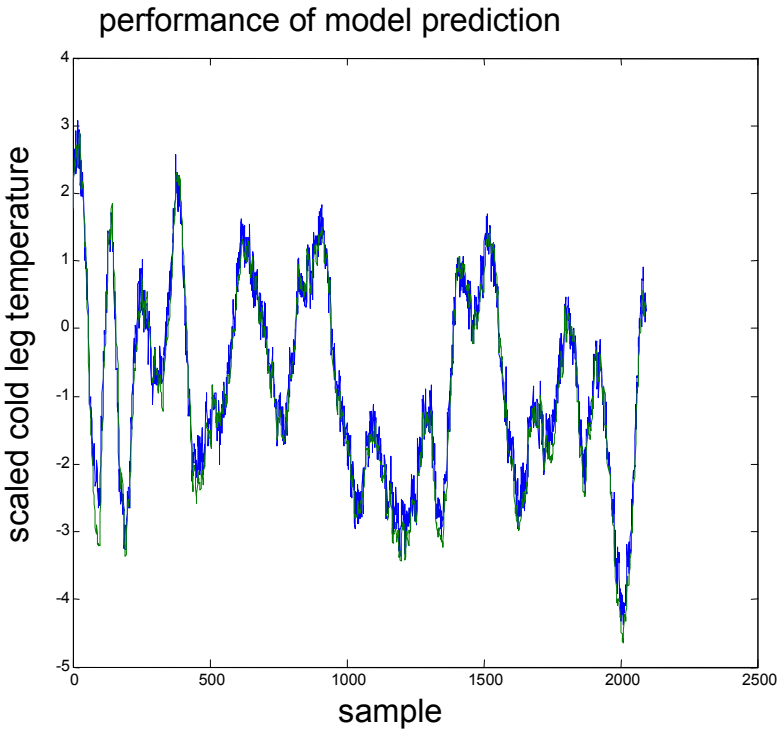

Figure 7.4. Model prediction of subspace identification for HCSG cold leg temperature.

7.4.3. Robust Fault Detection Design

To show the performance of the developed robust fault detection algorithm, the identified linear state space model is used to generate data with model uncertainty. The model uncertainty is introduced by adding an additive term to the state vector after the 300th sample. The model uncertainty term has a fixed direction but the magnitude of the model uncertainty varies linearly with time.

Figure 7.5 shows the performance of the developed robust fault detection algorithm to sensor faults. Model uncertainty is introduced after the 300th sample and a cold leg temperature sensor fault with a bias of 1 ^{o}C is injected after the 500th sample. The upper plot shows that if model uncertainty is not decoupled the fault detection index will not be able to distinguish a sensor fault and model uncertainty. However, the lower plot shows that the developed robust fault detection algorithm results in a fault detection index greater than 1.0 only after a fault has occurred to the system. Therefore, it can be concluded that the developed robust fault diagnosis algorithm is able to decouple model uncertainty without loss of the capability of fault detection.

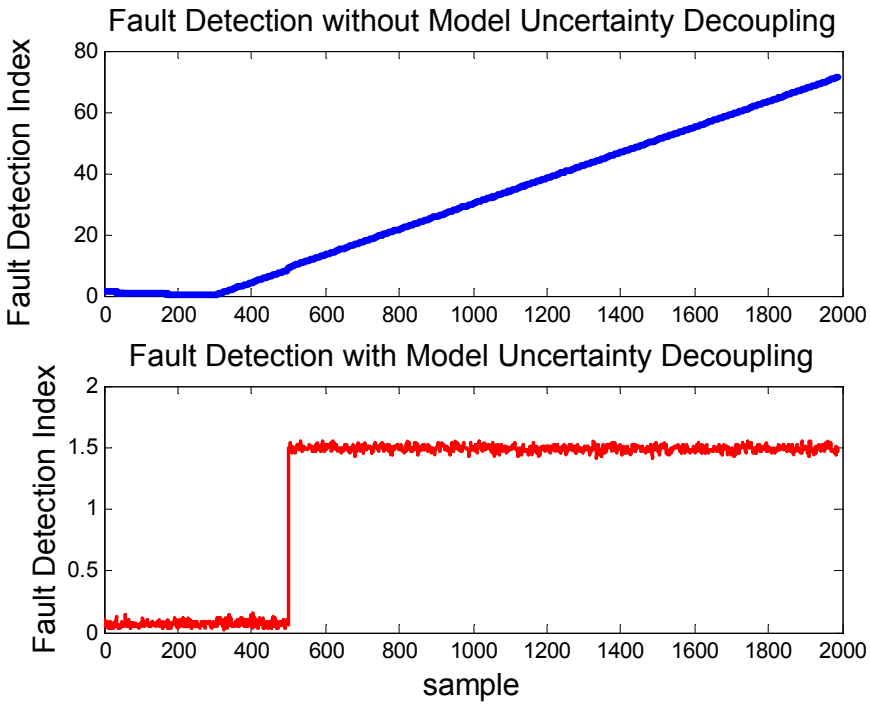

Figure 7.5. Robust fault detection for cold leg temperature sensor fault.

Figure 7.6 shows the performance of the fault detection index for a feed water flow meter bias fault with a magnitude of 2% at 1500 second during the transient when the reactor power is reduced from 100% to 95% at a rate of 0.0012 Full Power/min. The fault detection residual generator responds to the fault with no time delay and generates a significant fault signal as significant as 10.0 compared with the fault detection index of less than 1.0 for fault free condition. It can also be seen that the generated fault detection

index has the desirable property that it returns to an insignificant level when the fault is recovered during the transient at 2500 seconds.

After the reactor reaches 95% power level, the fault detection index remains less than 1.0, which can demonstrate that the identified model has learned the system dynamics appropriately because the model still retains its good prediction capability at 95% power level, an unknown operation condition, although the model is built from the data collected at 100% power level. From the viewpoint of FDI robustness, it can be concluded that a dynamic model is superior to a static model in which case model prediction is simply an interpolation among the data used to train it without revealing the causal relationship among the measured variables and thus without the capability of generalization outside the training space.

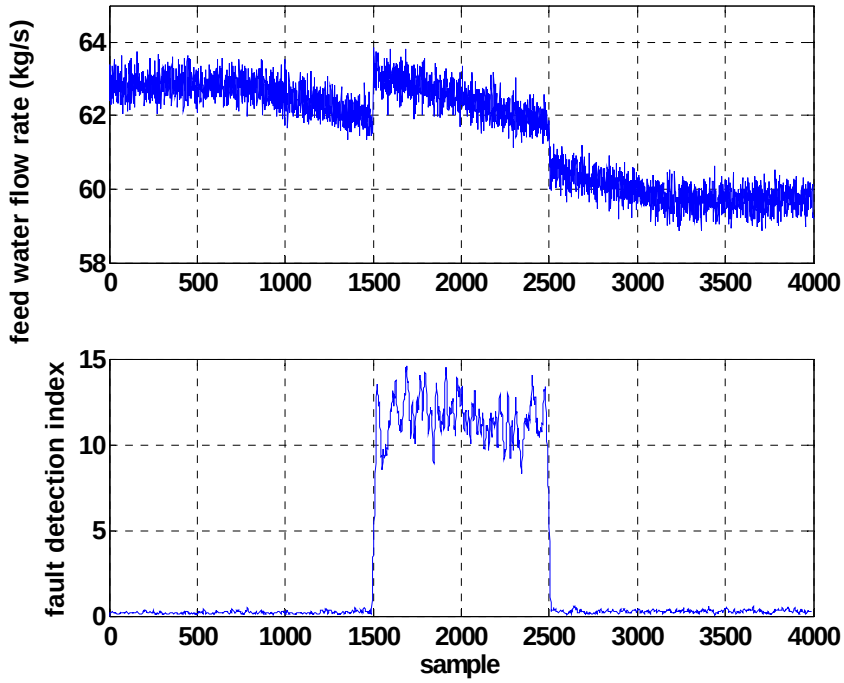

Figure 7.6. Fault detection of feed water flow meter sensor fault during a reactor power transient.

Figure 7.7 shows the performance of fault detection for a steam pressure sensor bias fault of 2% magnitude at the 800th sample when the reactor is initially operating at 90% full power. Because the steam pressure is controlled in the HCSG system, the steam pressure will experience a fault-induced transient. The fault detection index responds immediately when the sensor fault occurs at the 800th sample. It is interesting to notice that the fault

detection index is almost constant after the fault occurs. On the one hand, this indicates that the identified model is able to represent the system dynamics initiated by the fault. On the other hand, the fault detection index does not return to an insignificant level even though the measured steam pressure has been brought back to the original level. This is because some other process variables such as the saturated boiling length and the sub-cooled length cannot be brought back to their original values due to the sensor fault.

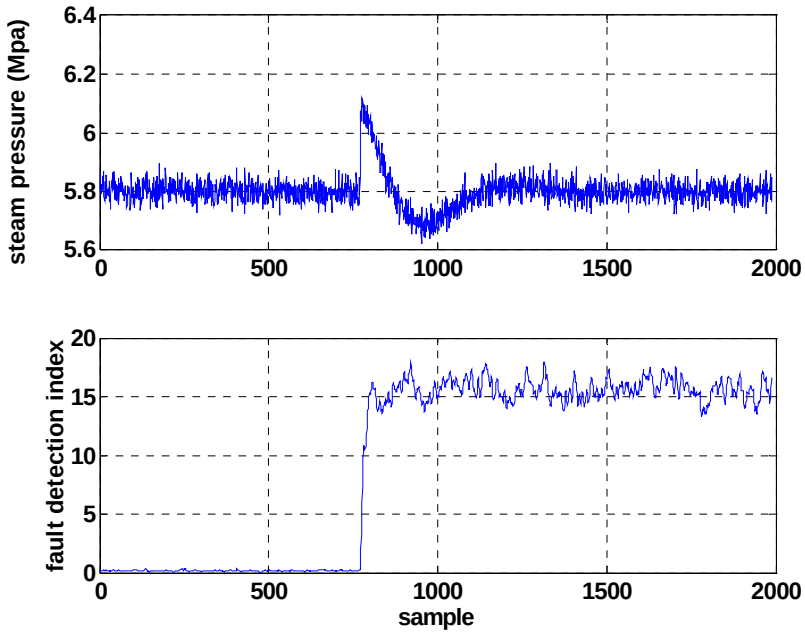

Figure 7.7. Fault detection of steam pressure sensor fault.

7.4.4. Robust Fault Isolation Design

Ten residual generators are designed for fault isolation. Each of the ten residual generators corresponds to ten linear transformations on the original estimation error vector such that it is sensitive to all faults but the one to which the residual generator is dedicated for fault isolation. The ten residual generators are dedicated to the isolation of the following sensor faults:

Variable 1: the cold leg temperature.
Variable 2: the steam pressure.
Variable 3: the steam temperature.
Variable 4: the saturated boiling length.

Variable 5: the sub-cooled length.
Variable 6: the hot leg temperature.
Variable 7: the steam flow rate.
Variable 8: the feed water temperature.
Variable 9: the feed water flow rate.
Variable 10: the primary flow rate.

Figure 7.8 shows the FDI indices of the ten residual generators responding to the feed water flow meter bias fault with a magnitude of 2% at 1500 second during the transient when the reactor power is reduced from 100% to 95% at a rate of 0.0012 Full Power/min. As can be seen, the residual generator dedicated to the isolation of the ninth variable produces an insignificant FDI index of less than 1.0 while all the other residual generators do not. Therefore, the feed water flow meter sensor fault can be correctly isolated when the fault is detected between 1500 second and 2500 second during the reactor power transient.

The FDI indices for the fifth variable and the seventh variable are approximately 1.2 and 2.0, respectively, while the FDI indices for the other variables are much significantly greater than 1.0. It can be seen from this that the fault isolation of feed water flow meter fault has less confidence level when it is to be isolated from a sub-cooled length measurement fault or a steam flow meter fault than the other faults. An insight we can obtain here is that FDI performance testing at design phase with a reliable simulation model should still be emphasized.

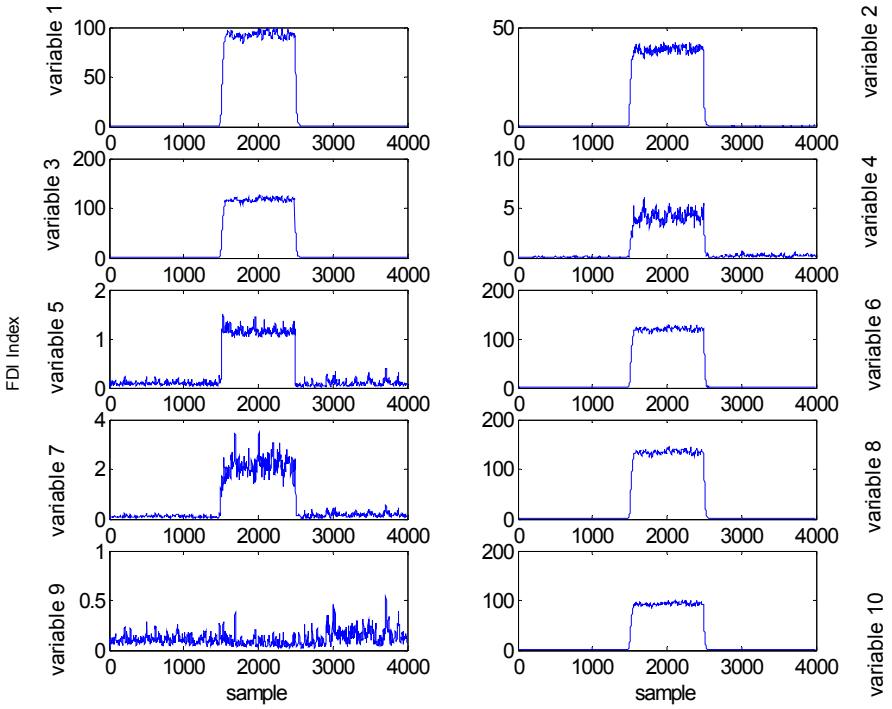

Figure 7.8. Fault isolation of feed water flow meter sensor fault during a reactor power transient.

Figure 7.8 has also demonstrated the success of the developed FDI method in that a predetermined logic of fault isolation is achieved through studying the identified model. This is a significant difference from many recently published literatures where FDI is inappropriately paraphrased as a pattern recognition problem. Pattern recognition needs to determine the fault features through the collection of faulty data, which is unrealistic in process engineering application.

The fault isolation residual generators have shown the robustness of the developed method to measurement noises. Although all the measured variables are added with 0.2% white Gaussian noise, the residual generators can successfully eliminate their effects on the residuals after EWMA filters are applied to the residuals.

Figure 7.9 shows the FDI indices of the designed ten residual generators for the fault isolation of a steam pressure sensor fault. In the figure, the FDI indices of all the variables except the second variables are greater than 1.0, therefore, the steam pressure sensor fault can be isolated correctly throughout the fault induced transient. As compared with static model based FDI approaches, the proposed approach is able to isolate a

controlled variable related sensor fault at the initial stage when it occurs. In the meantime, fault misdiagnosis can be avoided during the fault-induced transient. Moreover, fault isolation is based on the identified model rather than fault information through appropriate design of residual generators such that the generated residuals follow the predetermined logic.

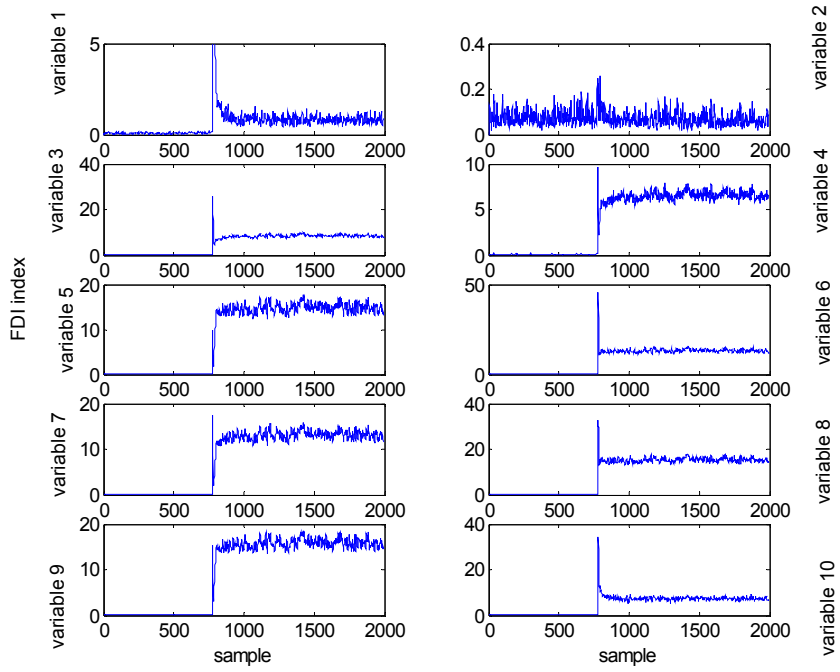

Figure 7.9. Fault isolation of steam pressure sensor fault.

Table 7.1 summarizes the FDI results for the five other sensor faults of the HCSG system that occur at 95% full power. The five faults are listed as follows:

Fault 1: cold leg temperature sensor fault with a bias of 1.0 ^{o}C,
Fault 2: steam temperature sensor fault with a bias of 1.0 ^{o}C,
Fault 3: hot leg temperature sensor fault with a bias of 1.0 ^{o}C,
Fault 4: steam flow meter fault with a bias of 1% nominal flow rate,
Fault 5: feed water temperature sensor fault with a bias of 1.0 ^{o}C.

Table 7.1. The FDI indices of bias type sensor faults

Faults / FDI index	Fault free	Fault 1	Fault 2	Fault 3	Fault 4	Fault 5
Fault detection	0.22	40.3	18.3	9.42	5.04	25.7
Cold leg temperature	0.15	**0.22**	1.7	2.25	3.45	6.3
Steam pressure	0.16	1.47	2.4	2.10	2.39	1.2
Steam temperature	0.16	2.43	**0.23**	**0.45**	4.31	22.0
Saturated boiling length	0.18	6.99	2.59	2.65	1.43	15.7
Sub-cooled length	0.18	12.7	9.2	6.30	2.06	1.3
Hot leg temperature	0.19	14.7	3.33	**0.31**	4.94	24.9
Steam flow rate	0.20	29.9	14.94	8.18	**0.22**	14.9
Feed water temperature	0.20	38.3	18.75	8.72	3.74	**0.24**
Feed water flow rate	0.19	28.8	14.64	7.31	4.55	7.43
Primary flow rate	0.16	16.1	4.51	1.65	5.76	23.7

During fault free conditions, the fault detection index is 0.22, which is less than 1.0 and will not trigger a false alarm. The FDI indices produced from all the designed residual generators for fault isolation are also less than 1.0 for fault free condition. This indirectly proves that the EWMA filtered residual vector does indeed follow a multi-dimensional Gaussian distribution with zero mean and a constant covariance matrix.

The fault detection indices are all significantly greater than 1.0 after the five faults occur. When the FDI indices of the ten residual generators designed for fault isolation are examined, they follow the predetermined logic of fault isolation for all the faults but hot leg temperature sensor fault. For the hot leg temperature sensor fault, both the residual generator dedicated to the isolation of the steam temperature sensor fault and the residual generator dedicated to the isolation of the hot leg temperature sensor fault generate an insignificant residual, which indicates an unknown fault according to the residual design scheme for isolation.

The reason is that there is a maximum sensitivity of the designed residual generator to an input fault, which is determined by the system model itself. However, because the designed residual generator can maintain the capability of being insensitive to the fault that it is designed to isolate regardless of the fault magnitude, the predetermined logic for fault isolation can always be followed if the fault magnitude is

big enough. It is found that the hot leg temperature sensor fault can be unambiguously isolated if its fault magnitude is increased to 3 ^{o}C. This example also demonstrates the importance of FDI design in reactor design phase and the necessity of testing its performance based on a realistic simulation.

7.5. Summary

A robust dynamic fault diagnosis algorithm has been presented in this Chapter for dynamic fault diagnosis of nuclear power systems. The theory of subspace identification was first described to extract low order state-space model from data generated by simulation codes. Robust parity space approach was then combined with subspace identification to design residual generators. A new one-step algorithm was derived without the need of explicitly identifying model uncertainty for uncertainty decoupling. The implementation of robust residual generator design was formulated as a generalized eigenvalue problem. Finally, the developed robust dynamic fault diagnosis algorithm was applied to the IRIS HCSG systems for transient fault detection and isolation. It has been shown that the developed algorithm is able to deal with model uncertainty for dynamic fault diagnosis without causing false alarms and can be used for reconfigurable control.

8. CONCLUDING REMARKS

8.1. Summary and Concluding Remarks

The following major tasks were completed during the project. All the originally stated milestones were accomplished during the project period. An extensive and valuable bibliography, on the various aspects of the causes and the monitoring of heat exchanger and steam generator degradation mechanisms, and on other related research topics, was assimilated as part of the deliverables of this research project.

1. Review of literature on the various tasks considered for research in this project. A complete Bibliography is given at the end of the report.
2. Development of a MATLAB-Simulink™ code to simulate the dynamic performance of a U-tube steam generator (UTSG) in a typical 1,140 MWe PWR. This multi-nodal model was used to simulate the effects of tube fouling, tube plugging, leakage and other process-related phenomenon. The UTSG model is coupled to the whole plant system in order to provide realistic simulation results. The nodal structure was expanded to account for spatial variations in the physical parameters. For example, the effect of fouling in the sub-cooled region has a higher influence on the steam pressure compared to a similar effect in the boiling region.
3. The high-fidelity nodal model of the UTSG was used to simulate the effects of fouling. Application of the group method of data handling (GMDH) method for process variable prediction. The model was used to generate a database representing normal and degraded process conditions.
4. Development of a laboratory heat exchanger system that was used to generate normal operation data and data under faulty device operation. This portable test rig was equipped with flow and pressure transmitters, flow meters, and thermocouples to measure fluid temperatures.
5. Development of a laboratory test module to simulate particulate fouling of HX tubes and its effect on overall thermal resistance. Application of the GMDH

technique to predict HX fluid temperatures, and to compare with the calculated thermal resistance.

6. Development of a hybrid first principle and data-based model that was used to update and fine-tune the model using process data. Predictive artificial neural network and nonlinear data-driven models were used for process monitoring and diagnosis. The hybrid models were classified into serial hybrid and parallel hybrid models. The serial modeling exhibited a better performance in predicting process variables compared to the parallel modeling. A simple heat exchanger model was used for this study.
7. Development of a laboratory piezo-device sensor suite for structural monitoring and a data acquisition system for measuring both input excitation signal and the response signal. This uses metal flat plates and tubing specimen. The comparison of the input excitation signal (transmitted signal) and the signal received at another location in the plate show excellent frequency response characteristics. The frequency characteristics changed when there was a flaw in the plate (or tubing) such as a crack, inclusion, deposit, etc. This task included the review of elastic wave propagation in plates under normal and fault conditions. Experiments were performed in air, and in water with and without bubbly flow. A review of wireless and Internet signal transmission was also performed as part of this experiment.
8. Development of advanced signal processing and defect classification algorithms. The transient data were analyzed using time-frequency techniques such as the wavelet transforms and the Hilbert-Huang transform (HHT). The HHT was found to be highly effective in processing non-stationary and nonlinear signals from the piezo-transducers.
9. Development of a moving-window technique in the time domain for detecting and quantifying flaw types in tubular structures. A window zooming technique was also developed for flaw location in tubes.
10. Theoretical study of elastic wave propagation (longitudinal and shear waves) in metallic flat plates and tubing with and without flaws.

11. Simulation of Lamb wave propagation using the finite-element code ABAQUS. This enables the verification of the experimental results.
12. Several publications were prepared during the project. A list of publications is given in Section 1. These were used for information dissemination.

8.2. Future Work

The following recommendations are made for future research and development as a follow-on to the work reported in these two volumes of the report.

1. Further theoretical study of the propagation of elastic waves due to defects in flat beam and tubular specimens.

2. Development of improved acoustic wave propagation experiments with focus on sensor placement for industrial applications. Refinement and integration of Hilbert Huang transform and image processing techniques in order to detect, locate, isolate, and quantify structural flaws.

3. Application of hybrid modeling approach to operating plant data.

.

BIBLIOGRAPHY related to the NEER Project

(neer01ref)

1. G. Kawiecki and A. Seagle, "Feasibility of Applying Distributed Piezotransducers to Structural Damage Detection," Proceedings of MARCON 98, Vol. 2, pp. 69.01-69.11, May 1998.

2. A.A. de Castro and D.K.S. Ting, "Sub-cooled Boiling Detection Using Spectral Analysis of Pressure Transducer Signals," Proceedings of MARCON 98, Vol. 2, pp. 68.01-68.15, May 1998.

3. M. Sakuma, S. Kanemoto, M. Ochiai, K. Higuma and M. Kobayashi, "Leakage Detection in Nuclear Power plants Using Ultrasonic Microphone Array System," Proceedings of MARCON 98, Vol. 2, pp. 67.01-67.09, May 1998.

4. F.-K. Chang, "Structural Health Monitoring: A Summary Report on the First International Workshop on Structural Health Monitoring, September 18-20, 1997," Proceedings of Structural Health Monitoring 2000, Stanford University, September 8-10, 1999.

5. A.V. Gribok, A.M. Urmanov and A.N. Volov, "Independent Component Analysis of Acoustic Signals Recorded During PFR End-of-Life Experiments," Proceedings of MARCON 97, Vol. 1, pp. 20.01-20.09, May 1997.

6. A.V. Gribok, I. Attieh, J.W. Hines and R.E. Uhrig, "Regularization of Feedwater Flow Rate Evaluation for Venturi Meter Fouling Problem in Nuclear Power Plants," Proceedings of Ninth International Topical Meeting on Nuclear Reactor Thermal Hydraulics, San Francisco, October 3-8, 1999.

7. V.I. Frankfurt and D.S. Kupperman, "Review of Electromagnetic NDT Methods for Monitoring the Degradation of Nuclear Reactor Components," Materials Evaluation, Vol. 50, No. 9, pp. 1053-1057, September 2001.

8. P.E. MacDonald, V.N. Shah, L.W. Ward and P.G. Ellison, *Steam generator Tube Failures,* NUREG/CR-6365, INEL-95/0383, April 1996.

9. D.R. Diercks, S. Bakhtiari, K.E. Kasza and D.S. Kupperman, *Steam Generator Tube Integrity Program,* NUREG/CR-6511, Vol. 7, ANL-00/4, September 2000.

10. S. Yokell, *A Working Guide to Shell-and-Tube Heat Exchangers,* McGraw-Hill, New York, 1990.

11. G. Walker, *Industrial Heat Exchangers,* McGraw-Hill, New York, 1982.

12. M. Naghedolfeizi and B.R. Upadhyaya, *Dynamic Modeling of a Pressurized Water Reactor Plant for Diagnsotics and Control,* Research Report, DOE/NE/88ER12824-02, June 1991.

13. F.-K. Chang, *A Summary Report of the 2nd Workshop on Structural Health Monitoring,* Stanford University, 2000. http://structure.stanford.edu/workshop

14. Piezo Systems, Inc., Cambridge, Massachusetts, *Introduction to Piezo Transducers,* June 2001. www.piezo.com

15. IAEA Report, *Advanced Signal Processing Techniques for Acoustic Detection of Sodium/Water Reaction,* IAEA-TECDOC-946, May 1997.

16. *Smart Structures and Materials,* Proceedings of Industrial and Commercial Applications of Smart Structures Technologies, SPIE Vol. 2721, San Diego, February 1996.

17. *Smart Structures and Materials,* Proceedings of Smart Structures and Integrated Systems, SPIE Vol. 2717, San Diego, February 1996.

18. S. Majumdar et al., *Failure Behavior of Internally Pressurized Flawed and Unflawed Steam Generator Tubing at High Temperature – Experiments and Comparison with Model Predictions,* NUREG/CR-6575, ANL-97/17, March 1998.

19. B.E. Morgan and C.L. Foster, *Acoustic Emission Monitoring of High-Energy Steam Piping,* Volume 1: Acoustic Emission Guidelines for Hot Reheat Piping, EPRI Report, TR-105265-V1, 1995.

20. B.C. Morgan and J.M. Rodgers, *Acoustic Emission Monitoring of High-Energy Headers,* Volume 1: Acoustic Emission Guidelines for Superheater Outlet Headers, EPRI Report, TR 107893-V1, 1997.

21. D.R. Diercks, J. Muscara and W.J. Shack, "Steam Generator Steam Integrity Program," Nuclear Engineering and Design, Vol. 165, pp. 143-149, 1996.

22. R. Comby, "Secondary Side Corrosion in Steam Generator Tubes: Lessons Learned in France from the In-service Inspection Results," Nuclear Engineering and Design, Vol. 168, pp. 255-259, 1997.

23. F. Cattant, "Lessons Learned from the Examination of Tubes Pulled from Electricite de France Steam Generators," Nuclear Engineering and Design, Vol. 168, pp. 241-253, 1997.

24. P. Calmon et al., "Models for the Computation of Ultrasonic Fields and Their Interaction with Defects in Realistic NDT Configurations, Nuclear Engineering and Design, Vol. 180, pp. 271-283, 1998.

25. R. Masini, E. Padovani, M.E. Ricotti and E. Zio, "Dynamic Simulation of a Steam Generator by Neural Networks," Nuclear Engineering and Design, Vol. 187, pp. 197-213, 1999.

26. D.R. Diercks, W.J. Shack and J. Muscara, "Overview of Steam Generator Tube Degradation and Integrity Issues," Nuclear Engineering Design, Vol. 194, pp. 19-30, 1999.

27. S. Majumdar, "Prediction of Structural Integrity of Steam Generator Tubes Under Severe Accident Conditions," Nuclear Engineering and Design, Vol. 194, pp. 31-55, 1999.

28. G. Srikantiah and P.R. Chappidi, "Particle Deposition and Fouling in PWR Steam Generators," Nuclear Engineering and Design, Vol. 200, pp. 285-294, 2000.

29. D.S. Kupperman, S. Bakhtiari and J. Muscara, "Steam generator Mock-up for Assessment of In-service Inspection Technology," Nuclear Engineering and Design, Vol. 207, pp. 299-305, 2001.

30. P.H. Hutton et al., *Acoustic Emission/Flaw Relationships for In-service Monitoring of LWRs,* NUREG/CR-5645, PNL-7479, October 1991.

31. K. Krishnamurthy, F. Lalande and C.A. Rogers, "Effects of Temperature on the Electrical Impedance of Piezoelectric Sensors," Proceedings of Smart Structures and Integrated Systems, SPIE Vol. 2717, pp. 302-310, February 1996.

32. G. Kawiecki, "Bending-Torsion Response of Open-Section Beams Actuated by Skewed Piezoelements," Proceedings of Smart Structures and Integrated Systems, SPIE Vol. 2717, pp. 494-508, February 1996.

33. IAEA-TECDOC-946, *Acoustic Signal Processing for the Detection of Sodium Boiling or Sodium-Water Reaction in LMFBRs*, Final Report of a Coordinated Research Program (1990-1995), IAEA, Vienna, 1997.

34. R. Whiteley and Y. Hu, "Integration of First-Principles Models with Neural Networks and Historical Data," MCEC Literature Review, August 1999.

35. B. Kohler, "Sound Fields of Ultrasonic Circumferential Arrays – Case of an Array for Steam generator Heat Exchanger Tubes," Proceedings of the 21st International Symposium on Acoustical Imaging, Laguna Beach, CA, March 2000.

36. F. Fellinger and K.J. Langenberg, “Numerical Techniques for Elastic Wave Propagation and Scattering,” in *Waves and Ultrasonic Nondestructive Evaluation,* Edited by S.K. Datta et al, pp. 81-86, North Holland, 1990.

37. A. Alessandri and T. Parisini, "Non-Linear Modeling of Complex Large-Scale Plants Using Neural Networks and Stochastic-Approximation", IEEE Transactions on Systems, Man and Cybernetics, Part A- Systems and Humans, 27(6), pp. 750-757, 1997.

38. P.B. Ferreira and B.R. Upadhyaya, “On-line Fault Monitoring and Isolation of Field Devices Using the Group Method of Data Handling,” Proceedings of MARCON 99, Vol. 2, pp. 79.01-79.15, May 1999.

39. A.V. Gribok, I. Attieh, J.W. Hines and R.E. Uhrig, "Stochastic Regularization of Feedwater Flow Rate Evaluation for the Venturi Meter Fouling Problem in Nuclear Power Plants," *Inverse Problems in Engineering*, Vol. 00, 1-26, 2001.

40. M.A. Kramer, M.L. Thompson and P.M. Bhagat, "Embedding Theoretical Models in Neural Networks," *Proc. Amer. Control Conference*, 1992.

41. D.C. Psichogios and L.H. Ungar, "A Hybrid Neural Networks First Principles Approach to Process Modeling," *AIChE Journal* 38(10), pp. 1499-1511, 1992.

42. H.A.B. te Braake, H.J.L.V. van Can and H.B. Verbruggen, "Semi-mechanistic Modeling of Chemical Processes with Neural Networks," *Engineering Applications of Artificial Intelligence*, 11(4), pp. 507-515, 1998.

43. M.L. Thompson, and M.A. Kramer, "Modeling Chemical Processes Using Prior Knowledge and Neural Networks," *AIChE Journal*, 4 (8), pp. 1328-1340, 1994.

44. H.J.L. van Can, C. Hellinga, K.C.A.M. Luyben, J.J. Heijnen and H.A.B. te Braake, "Strategy for Dynamic Process Modeling Based on Neural Networks in Macroscopic Balances," *AIChE Journal*, 42(12), pp. 3403-3418, 1996.

45. J.A. Wilson and L.F.M. Zorsetto, "A Generalized Approach to Process State Estimation Using Hybrid Artificial Neural Network Mechanistic Models," *Computer & Chemical Engineering*, 21(9), pp. 951-963, 1997.

46. K. Choi and F.-K. Chang, “Identification of Impact Force and Location Using Distributed Sensors,” AIAA Journal, Vol. 34, No. 1, pp. 136-142, January 1996.

47. G. Hearn and R.B. Testa, “Modal Analysis for Damage Detection in Structures,” Journal of Structural Engineering, Vol. 117, No. 10, pp. 3042-3063, October 1991.

48. J.-S. Lew, “Using Transfer Function Parameter Changes for Damage Detection of Structures,” AIAA Journal, Vol. 33, No. 11, pp. 2189-2193, November 1995.

49. R.Y. Liang, J. Hu and F. Choy, “Quantitative NDE Technique for Assessing Damages in Beam Structures,” Journal of Engineering Mechanics, Vol. 118, No. 7, 1468-1487, July 1992.

50. R.A. Manning, “Structural Damage Detection Using Active Members and Neural Networks,” AIAA Journal, Vol. 32, No. 6, pp. 1331-1333, 1994.

51. M.A. Moetakef, S.P. Joshi and K.L. Lawrence, “ Elastic Wave Generation by Piezoceramic Patches,” AIAA Journal, Vol. 34, No. 10, pp. 2110-2117, October 1996.

52. N. Stubbs and J.-T. Kim, “Damage Localization in Structures Without Baseline Modal Parameters,” AIAA Journal, Vol. 34, No. 8, pp. 1645-1649, August 1996.

53. G. Kawiecki and A. Seagle, "Feasibility of Applying Distributed Piezo-transducers to Structural Damage Detection", Journal of Intelligent Material Systems and Structures, Vol. 9, pp. 189-197, March 1998.

54. Sandia Laboratory Homepage: http://www.sandia.gov

55. P.A. Meyer and J.L. Rose, “Guided Wave Applications of Piezo-composite Transducers,” ASNT Fall Conference Seattle, Washington, October 1996.

56. P. Meyer, “Improved Sound Field Penetration Using Piezo-composite Transducers,” ASNT Fall Conference Seattle, Washington, October 1996.

56. M.A. Hamstad, “An Illustrated Overview of the Use and Value of a Wavelet Transformation to Acoustic Emission Technology,” AGU-Vallen Wavelet, 2002.

58. J.P. Holman, *Heat Transfer*, McGraw-Hill, Ninth Edition, New York, 2002.

59. M.A. Heckl, "Sound Propagation in Bundles of Periodically Arranged Cylindrical Tubes," Acustica, Vol. 77, pp. 143-152, 1992.

60. X.Y. Huang and M.A. Heckl, "Transmission and Dissipation of Sound Waves in Tube Bundles," Acustica, Vol. 78, pp. 191-200, 1993.

61. D. Firth, M.A. Heckl, J.A. McKnight, L.S. Mulholland, and R. Rowley, "Sound Propagation in a Steam generator: Experimental and Theoretical Results," Nuclear Energy, Vol. 32, No. 6, pp. 369-378, December 1993.

62. B.A.T. Petersson, "Structural Acoustic Power Transmission by Point Moment and Force Excitation, Part II: Plate-Like Structures," Journal of Sound and Vibration, Vol. 160, No. 1, pp. 67-91, 1993.

63. P.A. Meyer, "Piezocomposites Improve Ultrasonic Testing," Advanced Materials & Processes, pp. 37-38, 1997.

64. P. E. MacDonald, V. N. Shah, L. W. Ward, and P. G. Ellison, "Steam Generator Tube Failures," NUREG/CR-6365, 1996.

65. K. C. Wade, "Steam Generator Degradation and its Impact on Continued Operation of Pressurized Water Reactors in the United States," Energy Information Administration/ Electric Power Monthly, August 1995.

66. http://domino.pall.com/www/weblib.nsf/pub/80EC605D2451474E852567EF0053F173?opendocument

67. http://www.cpe.surrey.ac.uk/dptri/hms/fouling.htm

68. C.I. Hussain, I.H. Newson, and T.R. Bott, "Diffusion Controlled Deposition of Particulate Matter from Flowing Slurries," Proceeding of the Eighth International Heat Transfer Conference, San Francisco, 1986.

69. S.K. Beal, "Particulate Fouling of Heat Exchangers," Proceeding of the Engineering Foundation Conference, White Harie, PA, Oct.-Nov. 1982.

70. H. Muller-Stehinhagen, F. Reif, N. Epstein, and A.P. Watkinson, "Influence of Operating Conditions on Particulate Fouling," *Canadian Journal of Chemical Engineering*, Vol. 66, pp. 42-50, February 1988.

71. Y. Mussalli et al, "Effects of Fouling and Corrosion on Heat Transfer," American Society of Mechanical Engineers, 1985.

72. R.L. Watts and L.O. Levine, "Monitoring Technology Trends with Patent Data: Fouling of Heat Exchangers - A Case Study," Presented at the 22nd National Heat Transfer Conference and Exhibition, Niagara Falls, New York, August 1984.

73. J. Taborek, T. Aoku, R.B. Ritter, J.W. Paeln, and J.G. Knudsen, "Fouling: the Major Unresolved Problem in Heat Transfer," *Chemical Engineering Progress*, Vol. 68, No. 2, February 1972.

74. H. Muller-Steinhagen, and R. Bloch, "Particulate Fouling in Heat Exchangers," Transcripts of Institute of Professional Engineers, New Zealand, EMC Eng-Sec., Vol. 15, No. 3, pp. 109-118, November 1988.

75. A.K. Gupta and T.W. Jackson, "On the Mechanism of Particle Deposition through

Boundary Layers in a Heat Exchanger System," Presented at the American Institute of Aeronautic and Astronautics, 24th Aerospace Sciences Meeting, Reno, Nevada, January 1986.

76. J.G. Knudsen, "Coping with Cooling Water Fouling in Tubular Heat Exchangers," AIChE Symposium Series, Vol. 85, No. 269, pp. 1-12, 1989.

77. P.G. Papavergos and A.B. Hadley, "Particle Deposition Behavior from Turbulent Flows," *Chemical Engineering Research*, Vol. 62, September 1984.

78. F.B. Incropera and D.P. DeWitt, Fundamentals of Heat and Mass Transfer", 4th Edition, John Wiley, New York, 1996.

79. R.L. Penha and J.W. Hines, "Hybrid System Modeling for Process Diagnostics," Proceedings of MARCON 2002, Knoxville, TN, May 2002.

80. S.R. Perillo and B.R. Upadhyaya, "Applications of Piezoelectric Devices in Engineering Systems," Proceedings of MARCON 2002, Knoxville, TN, May 2002.

81. B.R. Upadhyaya, J.W. Hines, X. Huang, N.A. Johansen, A.V. Gribok, and S.R. Perillo, "Automated Monitoring and Diagnostics of the Integrity of Nuclear Plant Steam generators, Transactions of the American Nuclear Society Annual Meeting, June 2002.

82. C.W. Turner, "Modeling Magnetite Particle Deposition in Nuclear Steam Generators and Comparisons with Plant Data," AECL Report, No. 1112, pp. 1-14, December 1994.

83. A. Stutzmann, L. Viricel, M. Dijoux, and P. Lemaire, "French Experience on o.d. IGA/SCC and Fouling of SG Tubes," Nuclear Energy, Vol. 41, No. 2, pp. 137-144, 2002.

84. H. Muller-Steinhagen, "Mitigation of Process Heat Exchanger Fouling: An Integral Approach," Transactions of IchemE, Vol. 76, 1988.

85. K.I. Shin, J.H. Park, H.D. Kim, and H.S. Chung, "Simulation of Stress Corrosion Crack Growth in Steam Generator Tubes," Nuclear Engineering and Design, Vol. 214, pp. 91-101, 2002.

86. S. Kakac and H. Liu, Heat Exchangers: Selection, Rating, and Thermal Design, Second Edition, CRC Press, 2002.

87. A.D. Dimarogonas, "Vibration For Engineers," 2nd Ed., 1996 Prentice-Hall.

88. A.D. Dimarogonas, "Vibration Engineering," West Publishing, 1976.

89. S. Timoshenko, D.H. Young, and W. Weaver Jr, "Vibration Problems in Engineering," 4th Edition, John Wiley, 1974.

90. J.W.S. Rayleigh and J.W. Strut, "The Theory of Sound", Vol. 1, 2nd Edition, Dover Publications, 1945.

91. J.W.S. Rayleigh, and J.W. Strut, "The Theory of Sound", Vol. 2, 2nd Edition, Dover Publications, 1945.

92. P.W. Smith, "Validation of Torsional - Bending Piezoelectric Actuator Concept," MS Thesis, The University of Tennessee, December 1993.

93. J. Zelenka, "Piezoelectric Resonators and their Applications", Elsevier Science, October 1986. (We have a hard copy of this book taken by the UT Dept. of Mechanical and Aerospace Engineering).

94. A. Hyvarinen, J. Karhunen, and E. Oja, *Independent Component Analysis*, Wley Interscience, New York, 2001.

95. T.-W. Lee, *Independent Component Analysis: Theory and Applications*, Kluwer Academic Publishers, Boston, 1998.

96. S. Roberts and R. Everson (Ed), *Independent Component Analysis: Principles and Practice*, Camridge University Press, UK, 2001.

97. M. Girolami (Ed), *Advances in Independent Component Analysis*, Springer, New York, 2000.

98. M.G. Fontana and N.D. Greene, " Corrosion Engineering," 2nd ed., McGraw-Hill, New York, 1978.

99. A. Stutzmann, et al, "French Experience on OD-IGA/SCC and Fouling of SG Tubes," Nuclear Energy, Vol. 41, No. 2, April 2002.

100. J. R. Davis et al, "Corrosion—Understanding the Basics," ASM International, 2000.

101. P. Marcus et al, "Corrosion Mechanisms in Theory and Practice," Marcel Dekker, 1995.

102. T. Kuppan, "Heat Exchanger Design Handbook," Marcel Dekker, New York, 2000.

103. C.F. Britton et al, "Effective Corrosion Monitoring," NACE, Material Performance, April 1988.

104. C. Wood, “On Chemistry and Corrosion at Nuclear Power Plants,” Nuclear News, October 2002.

105. J. Gorman, “Survey of PWR Water Chemistry,” NUREG/CR-5116, 1989.

106. “Water Chemistry and Corrosion Problems in Nuclear Power Plants,” Proceedings of an International Symposium on Water Chemistry and Corrosion Problems of Nuclear Reactor Systems and Components Organized by IAEA, 1982.

107. NEI 97-06 (Rev 1) “Steam Generator Program Guidelines,” January 2001.

108. PWR Steam Generator Examination Guidelines, EPRI Report TR-107569**.**

109. PWR Primary-to-Secondary Leak Guidelines, EPRI Report TR-104788**.**

110. PWR Secondary Water Chemistry Guidelines, EPRI Report TR-102134**.**

111. PWR Primary Water Chemistry Guidelines, EPRI Report TR-105714**.**

112. Steam Generator Integrity Assessment Guideline, EPRI Report TR-107621.

113. PWR Steam Generator Tube Plug Assessment Document, EPRI Report TR-109495.

114. EPRI PWR Sleeving Assessment Document, EPRI Report TR-105962.

115. EPRI NP-7552 “Heat Exchanger Performance Monitoring Guidelines,” December 1991.

116. Y. Liner et al, “Simulation of Magnetite Particulate Fouling in Nuclear Steam Generators,” Chalk River Laboratories, AECL Research, Ontario, Canada, 1992.

117. C.W. Turner et al, "Modeling Magnetite Particle Deposition in Nuclear Steam Generators and Comparisons with Plant Data," Presented at the Second International Steam Generator and Heat Exchanger Conference, Toronto, Canada, 1994.

118. Cleaver J.W. et al, “The Effect of Re-entrainment on Particle Deposition,” Chemical Engineering and Science, Vol. 31, 1976.

119. G. Bontempi, M. Birattari, and H. Bersini, "Lazy Learning: a Local Method for Supervised Learning in New Learning Paradigms in Soft Computing," L.C. Jain and J. Kacprzyk (eds.) Physica-Verlag (Springer-Verlag), Heidelberg and New York, 97 - 137. (http://iridia.ulb.ac.be/~gbonte/Papers.html), 2001.

120. M. Birattari and G. Bontempi. (1999) The Lazy Learning Toolbox, for use with Matlab, Technical Report TR/IRIDIA/99-7, 1999. Iridia, Université Libre de Bruxelles, Brussels, Belgium.(http://iridia.ulb.ac.be/~mbiro/paperi.html)

121. T. Ikeda, *Fundamentals of Piezoelectricity,* Oxford University Press, 1997.

122. C.Z. Rosen et al., *Piezoelectricy,* Springer-Verlag New York, 1995.

123. G.W. Taylor et al., *Piezoelectricity,* Gordon & Breach Publishing, 1985.

124. N.N. Rogacheva, *Theory of Piezoelectric Plates and Shells,* CRC Press, 1994.

125. G. Gautschi, *Piezoelectric Sensorics: Force, Strain, Pressure, Acceleration and Acoustic Emission Sensors, Materials and Amplifiers,* Springer-Verlag New York, 2002.

126. K.-H. Hoffmann, "*1st Caesarium - Smart Materials: Proceedings of the 1st Caesarium,*" Bonn, Nov. 17-19, 1999.

127. C. Lu and A.W. Czanderna, *Applications of Piezoelectric Quartz Crystal Microbalances,* Elsevier Science, February 1984.

128. J.M.M. Herbert, *Ferroelectric Transducers and Sensors, Vol. 3,* Gordon & Breach Publishing, January 1982.

129. H.F. Tiersten, *Linear Piezoelectric Plate Vibrations: Elements of the Linear Theory of Piezoelectricity and the Vibrations of Piezoelectric Plates,* Kluwer Academic Publishers, February 1969.

130. K. Uchino, *Piezoelectric Actuators and Ultrasonic Motors,* Kluwer Academic Publishers, November 1996.

131. M.E. Regelbrugge, "*Smart Structures and Integrated Systems", Vol. 332,* SPIE-International Society for Optical Engineering, July 1998.

132. C.S. Lynch, "*Smart Structures and Materials 2000 Active Materials: Behavior and Mechanics,*" SPIE Optical Engineering Press, January 2000.

133. J. Holnicki-Szulc et al., "*Smart Structures : Requirements and Potential Applications in Mechanical and Civil Engineering,"* Kluwer Academic Publishers, May 1999.

134. "*Specifications and Tests for Piezoelectric Pressure and Sound-Pressure Transducers: ISA Standard S37.10,"* Instrument Society of America, 1982.

135. Y. Yuan and F.F. Ling, *Vibrations of Elastic Plates : Linear and Nonlinear*

Dynamical Modeling of Sandwiches, Laminated Composites, and Piezoelectric Layers, Springer-Verlag New York, January 1995.

136. K. Choi. and F.-K. Chang, "*Identification of Impact Force and Location Using Distributed Sensors*," AIAA Journal, Vol. 34, No. 1, pp. 136-142, January 1996.

137. G. Hearn.and R.B. Testa, "*Modal Analysis for Damage Detection in Structures*," J. of Structural Engineering, Vol. 117, No. 10, pp. 3042-3063, October 1991.

138. J.-S. Lew, "*Using Transfer Function Parameter Changes for Damage Detection of Structures*," AIAA Journal, Vol. 33, No. 11, , pp. 2189-2193, November 1991.

139. R.Y. Liang, J. Hu, and F. Choy, "*Quantitative NDE Technique for Assessing Damages in Beam Structures*," Journal of Engineering Mechanics, Vol. 118, No. 7, 1468-1487, July 1992.

140. R.A. Manning, "*Structural Damage Detection Using Active Members and Neural Networks*," AIAA Journal, Vol. 32, No. 6, pp 1331-1333, 1994.

141. M.A. Moetakef, S.P. Joshi, and K.L. Lawrence, "*Elastic Wave Generation by Piezoceramic Patches*," AIAA Journal, Vol. 34, No. 10, pp. 2110-2117, October 1996.

142. N. Stubbs and J.-T. Kim, "*Damage Localization in Structures Without Baseline Modal Parameters*," AIAA Journal, Vol. 34, No. 8, , pp. 1645-1649, August 1996.

143. Z. Ounaies, "*Piezoelectric Materials for Sensor and Actuator Applications at NASA LaRC,*" ICASE Research Quarterly.
http://www.icase.edu/RQ/archive/v8n2/art1.html
http://www.icase.edu/

144. American Institute of Physics Website, http://www.aip.org

145. Materials Engineering, University of Purdue's Website
http://www.ecn.purdue.edu/Engr/

146. G. Kawiecki, "*Feasibility of Applying Distributed Piezotransducers to Structural Damage Detection,*" Journal of Intelligent Material Systems and Structures, Vol. 9, pp. 189-197, March 1998.

147. P.W. Smith, "Validation of Torsional - Bending Piezoelectric Actuator Concept," MS Thesis, The University of Tennessee, December 1993.

148. J. Zelenka, "Piezoelectric Resonators and their Applications," Elsevier Science,

October 1986.

149. B.R. Upadhyaya, J.W. Hines et al., *On-Line Monitoring and Diagnostics of the Integrity of Nuclear Plant Steam Generators and Heat Exchangers*, Annual Report prepared for the U.S. Department of Energy, Report No. DE-FG07-01ID14114/UTNE-03, The University of Tennessee, June 2002.

150. L.F. Melo et al, "Particle Transport in Fouling Caused by KAOLIN-Water Suspensions on Copper Tubes," Canadian Journal of Chemical Engineering, Volume 66, February 1988.

151. J. Middis et al, "Particulate Fouling in Heat Exchangers with Enhanced Surfaces," 18th Australasian Chemical Engineering Conference, Auckland, New Zealand, 1990.

152. L. M. Chamra et al, "Effect of Particle Size and Size Distribution on Particulate Fouling in Enhanced Tubes," Enhanced Heat Transfer, Vol. 1, No. 1, 1993.

153. H. Muller-Steinhagen et al, "Particulate Fouling in Heat Exchangers," Transactions of EMCh, Vol. 15, No. 3, November 1988.

154. M. Basset et al, "The Fouling of Alloy-800 Heat Exchange Surfaces by Magnetite Particles," Canadian Journal of Chemical Engineering, Vol. 78, February 2000.

155. T. Sugioto et al, "Formation of Uniform Spherical Magnetite Particles by Crystallization from Ferrous Hydroxide Gels," Journal of Colloid and Interface Science, Vol. 74, No. 1, March 1980.

156. C.W. Turner et al, "Deposition of Magnetite Particles from Flowing Suspensions under Flow-Boiling and Single-Phase Forced-Convective Heat Transfer," Canadian Journal of Chemical Engineering, Vol. 78, December 2000.

157. H. Muller-Steinhagen et al, "Influence of Operating Conditions on Particulate Fouling," Canadian Journal of Chemical Engineering, Vol. 66, February 1988.

158. G. Bontempi, M. Birattari and H. Bersini, "Lazy Learning: A Logical Method for Supervised Learning," http://iridia.ulb.ac.be/~lazy.

159. J.L. Rose, *Ultrasonic Waves in Solid Media*, Cambridege University Press, 1999.

160. I.A. Viktorov, *Raleigh and Lamb Waves,* Plenum Press, New York, 1967.

161. B.A. Auld, *Acoustic Fields and Waves in Solids,* 2nd Edition, Robert E. Krieger Publishing Company, 1990.

162. J. Miklowitz, *The Theory of Elastic Waves and Waveguides,* North-Holland

Publishing Company, New York, 1978.

163. C.K. Chui, *An Introduction to Wavelets*, Academic Press, New York, 1992.

164. G. Strang and T. Nguyen, *Wavelets and Filter Banks*, Wellesley-Cambridge Press, 1997.

165. D.N. Alleyne, M.J.S. Lowe and P. Cawley, "The Reflection of Guided Waves From Circumferential Notches in Pipes," J. of Applied Mechanics, Vol. 65, pp. 635-641, September 1998.

166. J.J. Ditri, "Utilization of Guided Elastic Waves for the Characterization of Circumferential Cracks in Hollow Cylinders," J. Acoust. Soc. Am., Vol. 96, No. 6, pp. 3769-3775, December 1994.

167. D. Alleyne and P. Cawley, "A Two-dimensional Fourier Transform Method for the Measurement of Propagating Multimode Signals," J. Acoust. Soc. Am., Vol. 89, No. 3, pp. 1159-1167, March 1991.

168. S.K. Goumas, M.E. Zervakis, and G.S. Stavrakakis, "Classification of Washing Machines Vibration Signals Using Discrete Wavelet Analysis for Feature Extraction, IEEE Transactions on Instrumentation and Measurement, Vol. 51, No. 3, June 2002.

169. P. Maass, G. Teschke, W. Willmann, and G. Wollmann, "Detection and Classification of Material Attributes – A Practical Application of Wavelet Analysis, IEEE Transactions on Signal Processing, Vol. 48, No. 8, August 2000.

170. L.R. Dragonette, D.M. Drumheller, C.F. Gaumond, D.H. Hughes, B.T. O'Connor, N. Yen, and T.J. Yoder, "The application of Two –Dimensional Transformations to the Analysis and Synthesis of Structural Excitations Observed in Acoustical Scattering," Proceedings of the IEEE, Special Issue on Time Frequency Analysis, Vol. 84, No. 9, pp. 1249-1263, September 1996.

171. N. Yen, "Wave Packet Decomposition," J. Acoust. Soc. Am., Vol. 95, No. 2, pp. 889-896, February 1994.

172. T.W. Wu, "On Computational Aspects of the Boundary Element Method for Acoustic Radiation and Scattering in a Perfect Waveguide, J. Acoust. Soc. Am., Vol. 96, No. 6, pp. 3733-3743, December 1994.

173. G.V. Frisk, J.W. Dickey, and H. Uberall, "Surface Wave Modes on Elastic Cylinders," J. Acoust. Soc. Am., Vol.58, No. 6, pp. 996-1008, November 1975.

174. G.C. Gaunaurd, "Elastic and Acoustic Resonance Wave Scattering," Applied Mechanics Review, Vol. 42, No. 6, pp. 143-192, June 1989.

175. M. Tohyama and T. Koike, *Fundamentals of Acoustic Signal Processing*, Academic Press, 1998.

176. L.E. Kinsler and A.R. Frey, *Fundamentals of Acoustics,* 2nd Edition, John Wiley, 1962.

177. O.V. Rudenko and S.I. Soluyan (Translated by R. T. Beyer), *Theoretical Foundations of Nonlinear Acoustics,* Consultants Bureau, New York, 1977.

178. L.B. Felsen et al., *Transient Electromagnetic Fields*, Springer-Verlag, New York, 1976.

179. D.F. Parker and G.A. Maugin (Eds), *Recent Developments in Surface Acoustic Waves*, Springer-Verlag, New York, 1987.

180. C. Campbell, *Surface Acoustic Wave Devices and Their Signal Processing Applications*, Academic Press, New York, 1989.

181. F.B. Stumpf, *Analytical Acoustics*, Ann Arbor Science Publishers, Michigan, 1980.

182. A.A. Oliner et al., *Acoustic Surface Waves*, Springer-Verlag, Berlin, 1978.

183. S. Nettel, *Wave Physics,* 2nd Edition, Springer, New York, 1995.

184. D.S. Ballantine et al., *Acoustic Wave Sensors Theory, Design and Physico-Chemical Applications*, Academic Press, San Diego, 1997.

185. K.F. Graff, *Wave Motion in Elastic Solids*, Ohio State University Press, 1975.

186. C.H. Chen, *Issues in Acoustic Signal Image Processing and Recognition*, Springer-Verlag, Berlin, 1983.

187. V.P. Gilbert, *Surface Acoustic Wave Device Designed to Monitor Frequency Shifts due to Adsorption of Mass on to a Piezoelectric Crystal,* M.S. Thesis, University of Tennessee, May 1992.

188. A. Hyvarinen, J. Karhunen, and E. Oja, *Independent Component Analysis*, John Wiley, New York, 2001.

189. P.J. Oonincx, *Mathematical Signal Analysis: Wavelets, Wigner Distribution, and a seismic Application,* Stichting Mathematisch Centrum, Amsterdam, 2000.

190. J. Miklowitz, *Elastic Waves and Waveguides,* North-Holland Publishing Company, New York, 1978.

191. J.L. Davis, *Wave Propagation in Solids and Fluids,* Springer-Verlag, New York, 1988.

192. L. Cohen, *Time-Frequency Analysis,* Prentice Hall, 1995.

193. U.B. Halabe and R. Franklin, "Fatigue Crack Detection in Metallic Members Using Ultrasonic Rayleigh Waves with Time and Frequency Analysis," Materials Evaluation, Vol. 59, No. 3, pp. 424-431, March 2001.

194. R. Carmona, W. Hwang, and B. Torresani, *Practical Time-Frequency Analysis*, Academic Press, New York, 1998.

195. J. Barshinger, J.L. Rose, and M.J. Avioli, "Guided Wave Resonance Tuning for Pipe Inspection," J. of Pressure Vessel Technology, Vol. 124, pp. 303-310, August 2002.

196. J. L. Rose, "A Baseline and Vision of Ultrasonic Guided Wave Inspection Potential," Journal of Pressure Vessel Technology, Vol. 124, pp. 273-282, August 2002.

197. E.V. Malyarenko and M.K. Hinders, "Fan Beam and Double Cross-hole Lamb Wave Tomography for Mapping Flaws in Aging Aircraft Structures," J. of Acoust. Soc. Am., Vol. 108, No. 4, pp. 1631-1639, October 2000.

198. K. Motegi, "Ultrasound Radiation into Water by a Lamb Wave Device Using a Piezoelectric Ceramic Plate with Spatially Varying Thickness," Ultrasonics, Vol. 37, pp. 505-510, 1999.

199. M. Deng, "Cumulative Second-harmonic Generation of Generalized Lamb-wave Propagation in a Solid Wave-guide, J. Appl. Physics, Vol. 33, pp. 207-215, 2000.

200. B.R. Upadhyaya, J.W. Hines, X. Huang, B. Lu, S.R. Perillo, and R.L. Penha, *On-Line Monitoring and Diagnostics of the Integrity of Nuclear Plant Steam Generators and Heat Exchangers,* Annual Report: Phase-2, prepared for the DOE-NEER Program by the University of Tennessee, Knoxville, Report No. DE-FG07-01ID14114/UTNE-04, June 2003.

201. M. Junger and D. Feit, *Sound Structures, and Their Interaction,* 2nd edition, the MIT Press, 1986.

202. G. Strang and T. Nguyen, *Wavelets and Filter Banks*, Wellesley –Cambridge Press, 1997.

203. S. Kessler, "Piezoelectric-Based In-Situ Damage Detection of Composite Materials for Structural Health Monitoring Systems," Ph.D. Dissertation, MIT, 2002.

204. E. Serrano and M. Fabio, " Application of the Wavelet Transform to Acoustic Emission Signals Processing," IEEE Transactions on Signal Processing, Vol. 44, No. 5, pp. 1270-1275, May 1996.

205. Q. Huynh, L. Cooper, N. Inthan and H. Shouval, " Classification of Underwater Mammals Using Feature Extraction Based on Time-Frequency Analysis and BCM Theory," IEEE Transactions on Signal Processing, Vol. 46, No. 5, pp.1202-1207, May 1998.

206. J. Tabrikian, G. Fostick and H. Messer, "Detection of Environmental Mismatch in a Shallow Water Waveguide," IEEE Transactions on Signal Processing, Vol. 47, No. 8, pp. 2181-2190, August 1999.

207. H Watanabe, Y. Matsumoto, S. Tanaka, and S. Katagiri, "A New Approach to Acoustic Signal Monitoring Based on the Generalized Probabilistic Descent Method," IEEE Transactions on Signal Processing, Vol. 47, No. 9, pp. 2615-2618, May 1999.

208. J. Lin and L. Qu, "Feature Extraction Based on Morlet Wavelet and its Application for Mechanical Fault Diagnosis," Journal of Sound and Vibration, 234(1), pp.135-148, 2000.

209. Z. Peng, Y. He and F. Chu, "Feature Extraction of the Rub-impact Rotor System by Means of Wavelet Analysis," Journal of Sound and Vibration, 259(4), pp.1000-1010, 2003.

210. Z. Peng, F. Chu and Y. He, "Vibration Signal Analysis and Feature Extraction Based on Reassigned Wavelet Scalogram," Journal of Sound and Vibration, 253(5), pp.1087-1100, 2002.

211. J. McKeon and M. Hinders, "Lamb Wave Scattering From a Thorough Hole," Journal of Sound and Vibration, 224(5), pp.843-862, 1999.

212. M. Al-Aghbari, F. Scarpa, and W. Staszewski, "On the Orthogonal Wavelet Transform for Model Reduction/Synthesis of Structures," Journal of Sound and Vibration, 254(4), pp. 805-817, 2002.

213. D.T. Blackstock, *Fundamentals of Physical Acoustics,* Wiley-Interscience, New York, 2000.

214. M.C. Crocker (Editor), *Handbook of Acoustics,* Wiley-Interscience, New York, 1998.

215. N.E. Huang et al., "The Empirical Mode Decomposition and the Hilbert Transform for Nonlinear and Non-stationary Time Series Analysis," Proc. R. Soc. London, Series A, 454, pp. 903-995, 1998.

216. Website for *ABAQUS* software documentation, 2004. http://himalaya.tamu.edu/help/softwareDocs/abaqus63/

217. M.D. Carelli, L. Conway, L. Oriani, B. Pertovic, and N.E. Todreas, "The Design and Safety Features of the IRIS Reactor," ICONE 11, Tokyo, Japan, April 2003.

218. J. Chen and R.J. Patton, *Robust Model-based Fault Diagnosis for Dynamic Systems,* Kluwer Academic Publishers, 1999.

219. B. De Moor, *Mathematical Concepts and Techniques for Modeling Static and Dynamic Systems*, PhD Dissertation, Department of Electrical Engineering, Katholieke Universiteit Leuven, Belgium, 1988.

220. E. Del Castillo, *Statistical Process Adjustment for Quality Control,* John Wiley, 2002.

221. W. Favoreel, B. De Moor, and P. Van Overschee P, "Subspace State Space System Identification for Industrial Processes," Proc. Of the 5th IFAC Symposium on Dynamics and Control of Process Systems, pp. 322-330, 1998.

222. R.E. Kalman, "A New Approach to Linear Filtering and Prediction Problems," J. Basic Engineering, Vol. 82, pp. 35-50, 1960.

223. W. Li and S. Shah, "Structured Residual Vector-Based Approach to Sensor Fault Detection and Isolation," Journal of Process Control, Vol. 12, pp. 429-443, 2002.

224. C.A. Lowry, W.H. Woodall, C.W. Champ, and S.E. Rigdon, "A Multivariate Exponentially Weighted Moving Average Control Chart," Technometrics, Vol. 34, pp. 46–53, 1992.

225. S.J. Qin and W. Li, "Detection and Identification of Faulty Sensors in Dynamic Processes," AIChE Journal, Vol. 47, No. 7, pp. 1581-1593, 2001.

226. B.R. Upadhyaya and K. Zhao, "Robust Techniques for Monitoring and Fault Diagnosis of IRIS Helical Coil Steam Generators," GENES4/ANP2003, Kyoto, Japan, 2003.

227. P. Van Overschee and B. De Moor, "A Unifying Theorem for Three Subspace System Identification Algorithms," Automatica, Special Issue on Trends in System Identification, Vol. 31, No. 12, pp. 1853-1864, 1995.

(updated: 09/2004)